Interfacial Microstructures and Interaction Forces between Colloidal Particles in Simple and Complex Fluids

—*Molecular Dynamics Simulation*—

Hiroyuki Shinto

1999

Interfacial Microstructures and Interaction Forces between Colloidal Particles in Simple and Complex Fluids

—Molecular Dynamics Simulation—

Hiroyuki Shinto

1999

Contents

Part II Adsorption of Ions and Surfactants onto Liquid/Solid Interfaces

List of Symbols

Latin alphabets

a	atom index	[—]
A	Hamaker constant	[J]
A	parameter in Lennard-Jones (9–3) potential	[J m^9]
A_{ij}	Pauling factor of ion pair i and j	[—]
$\mathbf{A}$	rotation matrix	[—]
b	atom index	[—]
b	parameter in Born–Mayer–Huggins potential	[J]
B	parameter in Lennard-Jones (9–3) potential	[J m^3]
C_{ij}	parameter in Born–Mayer–Huggins potential	[J m^6]
d	core diameter of spherical particle	[m]
D	self-diffusion coefficient	[m^2 s^{-1}]
D_{ij}	parameter in Born–Mayer–Huggins potential	[J m^8]
e	elementary charge	[C]
E	total internal energy	[J]
$\mathbf{F}$	force on molecule	[N]
$g(r)$	pair distribution function	[—]
h	attractive headlike particle	
h	fluid layer thickness	[m]
H	repulsive headlike particle	
H′	repulsive headlike particle interacting strongly with solid surface	
H_1	thickness of bilayer formed at single surface	[m]
H_2	thickness of bilayer formed between surfaces	[m]
i	molecule index	[—]
I_{xx}, I_{yy}, I_{zz}	principal elements of inertia tensor	[kg m]
$\mathbf{I}$	molecular moment of inertia	[kg m]
j	molecule index	[—]

k	molecule index	[—]
k	spring constant in harmonic potential	[N m^{-1}]
k_B	Boltzman's constant	[J K^{-1}]
l	bond length between neighboring sites in molecule	[m]
L	box length	[m]
m	mass of particle or molecule	[kg]
n	number or aggregate size	[—]
$\mathbf{n}_z$	surface normal	[—]
N	normalizing constant	[—]
N	number of particles or molecules	[—]
$\mathbf{N}(t)$	residence vector	[—]
o	oillike particle	
P	probability distribution of molecular orientation	[(degree)$^{-1}$] or [—]
$P_{W/A}$	water/amphiphile number ratio	[—]
q	point charge	[C]
r	molecular separation	[m]
r'	distance from macroparticle surface ($r - r_M$)	[m]
r_M	core radius of macroparticle ($d_M/2$)	[m]
$\mathbf{r}$	molecular position	[m]
$\mathbf{r}_{ab}$	site–site vector ($\mathbf{r}_{ia} - \mathbf{r}_{jb}$)	[m]
$\mathbf{r}_{ib}$	ion–site vector ($\mathbf{r}_i - \mathbf{r}_{jb}$)	[m]
$\mathbf{r}_{ij}$	position of molecule i relative to j ($\mathbf{r}_i - \mathbf{r}_j$)	[m]
R	center-to-center distance between macroparticles	[m]
R'	nearest separation between macroparticles ($R - d_M$)	[m]
$R(t)$	residence autocorrelation function	[—]
R^{cut}	cutoff separation	[m]
s	scaled distance	[—]
t	taillike particle	
t	time	[s]
T	absolute temperature	[K]
$\mathbf{T}$	torque on molecule	[N m]

$u(r)$	pair potential for molecule–molecule interaction	[J]
$u(z)$	pair potential for molecule–wall interaction	[J]
$\mathbf{u}$	unit vector	[—]
U	total potential energy	[J]
V	volume of system	[m^3]
w	waterlike particle	
w_{alc}	alcohol weight fraction	[—]
W	potential of mean force (PMF)	[J]
x	Cartesian coordinate	[m]
X	volume fraction of surfactants or amphiphiles	[—] or [vol %]
y	Cartesian coordinate	[m]
z	Cartesian coordinate	[m]
z'	perpendicular distance from planar wall	[m]
Z	perpendicular distance from planar wall	[m]

Greek alphabets

α	fluid layer index	[—]
Δ	separation between lattice plane	[m]
ΔG^{bar}	energy barrier for direct adsorption	[J]
Δr	separation between concentric spheres	[m]
Δt	time step	[s]
Δx	molecular displacement ($x(t) - x(0)$)	[m]
Δy	molecular displacement ($y(t) - y(0)$)	[m]
ε	energy parameter in pair potential	[J]
ε_0	permittivity of free space	[$C^2\ J^{-1}\ m^{-1}$]
ε_{HB}	hydrogen bond energy	[J]
ϕ	angle	[degree] or [rad]
$\phi(r)$	potential for particle–particle interaction	[J]
μ	molecular dipole moment	[C m]
θ	angle	[degree] or [rad]
ρ	number density	[m^{-3}] or [m^{-2}]

ρ	parameter in Born–Mayer–Huggins potential	[m]
σ	size parameter in pair potential	[m]
$\sigma(...)$	root mean square fluctuation	[...]
τ	scaled time or discrete time	[—]
τ_0	time unit for Lennard-Jones system $(\sigma(m/\varepsilon)^{1/2})$	[s]
τ_F	force correlation time step	[—]
τ_T	time constant for heat bath	[s]
ω	molecular angular velocity	[rad s^{-1}]
Ω	molecular orientation	[rad]
ξ	Cartesian component (x, y, z)	[m]
ξ	constraint condition	[m^2]
$\psi(r)$	potential for particle–macroparticle interaction	[J]
$\psi(z)$	potential for particle–wall interaction	[J]

Subscript and superscript

F_ξ	denotes ξ component (= x, y, z) of force vector
$\mathbf{F}_{ia}$	denotes force on atom a in molecule i
$\mathbf{r}_{ia}$	denotes position of atom a in molecule i
*	denotes reduced variables
A	denotes amphiphile
ad	denotes adhesion
br	denotes bridge
cut	denotes cutoff
dir	denotes direct interaction
ext	denotes external field
FSH	denotes force shifting
h	denotes hydration
HB	denotes hydrogen bond
I	denotes ion
in	denotes inner region
m	denotes modified form

M	denotes macroparticle
min	denotes minimum
NN	denotes nearest neighbor
S	denotes solvent or solution
solv	denotes solvent
surf	denotes surface or surfactant
tot	denotes total
tr	denotes truncation
vol	denotes volume
W	denotes water or wall

1
General Introduction

1.1 Introductory remarks

Colloidal particles are utilized in the production processes of various advanced functional materials, such as electric and magnetic materials, catalyses, ceramics, paints, medicines, and cosmetics. In these processes, the interfacial features influence the behavior of the colloids in a medium and the function of the final products. For the accurate control of the material property, therefore, it is indispensable to estimate precisely the behavior of molecules near the surface of colloidal particles and to evaluate quantitatively the interparticle force and the behavior of the particles.

Colloidal particles are dispersed in various liquid media, which is named the suspension. The characteristics of the suspension mainly depend on the interaction force between particles, that is, the "mean force" which is determined not only by the direct interparticle force but also by the solvent–particle and solvent–solvent interactions. In order to control the property of the suspension, the third substances (e.g., electrolytes, surfactants, and polymers) are added to a solution as either the dispersant or the floccurant if necessary. These additives usually adsorb onto the surface of colloidal particles to change their interaction force substantially. Thus, the microscopic structure and dynamics of a solid/liquid interface govern the surface force and consequently affect the macroscopic behavior of the colloidal particles.

In actual processes, the contribution of a non-equilibrium field becomes important in addition to the equilibrium behavior. For example, it was observed experimentally that the shear flow largely influences the phase separation phenomena such as the nucleation and the spinodal decomposition. In the author's opinion, one can not explain satisfactorily how a non-equilibrium field influences on a suspension, until one understand exactly the basic characteristics of the suspension. In this dissertation, therefore, the main attention is focused on the equilibrium microscopic features of the solid/liquid interfaces and the interaction forces between colloidal particles. But the non-equilibrium features are also examined when they are needed.

1.2 Experimental methods

Detailed understanding of interaction forces between colloidal particles in fluids has been the central subject of colloid science. Historically, the van der Waals theory and the Derjaguin–Landau–Verwey–Overbeek (DLVO) theory have been frequently used to describe the interaction between colloidal particles in electrolyte solutions. Most experimental results were explained by these theories, although some observations were not.

Recently, the surface force apparatus (SFA) and the atomic force microscopy (AFM) were developed to measure *in situ* the surface force in fluids. As described below, these instruments have contributed to the progress of colloid science as greatly as the van der Waals and DLVO theories.

1.2.1 Surface force apparatus (SFA)

The SFA was developed in late 1970s [Israelachvili and Adams, 1978;

TABLE 1.1: Force measurements by SFA

Liquid medium	Reference
Inert nonpolar liquid	Horn and Israelachvili [1981], Christenson [1983, 1985, 1986]
Polar liquid	Christenson and Horn [1983], Christenson [1984]
Hydrogen-bonding liquid	Christenson [1984], Christenson and Horn [1985]
Aqueous electrolyte solution	Pashley [1981], Pashley and Israelachvili [1984a, 1984b]
Liquid alkane	Christenson *et al.* [1987], Herder *et al.* [1989], Gee and Israelachvili [1990]
Polymer melt	Horn and Israelachvili [1988], Horn *et al.* [1989], Israelachvili and Kott [1988]

Israelachvili, 1991, Section 10.7] and has been used to measure the interaction forces between cleaved or chemically modified mica surfaces in various media (see Table 1.1). The attractive van der Waals and repulsive electric double-layer forces were measured *in situ* and the results were found to agree quantitatively with the prediction given by the above theories. However, the forces which the DLVO theory fails to predict (i.e., non-DLVO forces) were also discovered; for example, the oscillatory structural force, the repulsive hydration force, the attractive hydrophobic force, the steric interaction in polymeric systems, and the capillary and adhesion forces [Israelachvili, 1987, 1991; Israelachvili and Wennerström, 1996; Christenson, 1988]. In particular, the long-range attraction which occurs between hydrophobic surfaces in water is important, because this attractive force has been utilized in various industries without knowing the origin of the force [Israelachvili, 1991, Section 13.6; Christenson and Claesson, 1988; Tsao *et al.*, 1991; Kurihara and Kunitake, 1992].

The SFA is a very powerful tool to investigate the interaction forces between large surfaces and provides a useful information about the adsorbed layers of molecules near the surface. However, the SFA can not probe the behavior of the

TABLE 1.2: Surfactant aggregates on solid surfaces visualized by AFM

Surfactant	Solid surface [a]	Reference
Cationic [b]	Graphite, MoS_2	Manne *et al.* [1994], Manne and Gaub [1995]
	Mica, Silica	Manne and Gaub [1995]
	Gold	Jaschke *et al.* [1995]
Anionic [c]	Graphite	Wanless and Ducker [1996]
	Gold	Jaschke *et al.* [1995]
Zwitterionic [d]	Graphite	Ducker and Grant [1996]
	Mica, Silicon nitride	Ducker and Grant [1996]
Nonionic [e]	Graphite	Patrick *et al.* [1997]

[a] Classified into hydrophobic, non-metal hydrophilic, and metal surfaces.

[b] Alkyltrimethylammonium halides.

[c] Sodium dodecyl sulfate (SDS).

[d] Dodecyldimethylammoniopropanesulfonate (DDAPS).

[e] Poly(oxyethylene) *n*-dodecyl ethers.

individual molecules, which is important to understand the detailed structures and dynamics of the adsorbed layers.

1.2.2 Atomic force microscopy (AFM)

In late 1980s, the AFM was developed to visualize the atomic scale roughness of a substrate surface and the adsorbate on the surface [Binning *et al.*, 1986; Hansma *et al.*, 1988]. However, Ducker *et al.* [1991, 1992] used the AFM to measure the interaction force between a colloidal probe and a substrate.

Using the AFM, the surfactants, polymers, and biomolecules on the surface have been investigated extensively. As for surfactants, recent *in situ* measurements listed in Table 1.2 show that surfactants form aggregates at the solid/liquid interface as well as in the bulk solution and the interfacial aggregates exhibit various morphology of spheres, cylinders, half-cylinders, and bilayers, depending

on the surface property and the surfactant structure [Manne, 1997]. All the experiments in Table 1.2 were carried out in aqueous solutions of nearly the critical micelle concentration (CMC). It was also found that even in sufficiently dilute solutions ($\simeq$ CMC/10^5) where micelles are not formed stably in the bulk, islandlike aggregates of cationic surfactants are formed on the mica surface [Fukuda, 1996]. But, why and how the aggregates are formed at solid/liquid interfaces are poorly understood at present.

1.3 Integral equation theory (IET)

1.3.1 Basics

In late 1970s, the theoretical works started to elucidate the characteristics of solid/liquid interfaces and the interactions between the solid surfaces from a molecular point of view, using the integral equation theory (IET). The IET is based on the Ornstein–Zernike relation connected with various equations of closure approximation [Hansen and McDonald, 1986]. The IET has the following advantages:

(i) The effects by a very small amount of elements on the whole system can be estimated appropriately.

(ii) Much computation time is not necessary, because the IET treats molecules *implicitly* through molecule–molecule pair correlation functions and there is no need to calculate interactions between all pairs of molecules.

On the contrary, there are the following disadvantages:

(i) It is not impossible but difficult to apply the IET to the system of complicated molecules.

(ii) The IET is applicable only to a stable (or metastable) single phase system in an

TABLE 1.3: Surface forces in various fluids analyzed by IET

Fluid		Reference
Pure	Lennard-Jones particle	Kjellander and Sarman [1990, 1991], Sarman [1990], Kinoshita *et al.* [1996b]
	Neutral hard-sphere	Henderson [1988], Attard *et al.* [1991], Kinoshita *et al.* [1996a], Götzelamann and Dietrich [1997]
	Dipolar hard-sphere	Attard *et al.* [1991], Kinoshita *et al.* [1996a]
	Waterlike hard-sphere	Kinoshita *et al.* [1996a]
	SPC/E water molecule	Kinoshita and Hirata [1996]
Mixed	Aqueous electrolyte	Kinoshita *et al.* [1996a]
	Hard-sphere mixture	Kinoshita *et al.* [1996b, 1996c], Kinoshita [1998]

equilibrium state and provides no dynamical information.

(iii) The reliability of the analyzed results depends largely on the closure equations used [Attard and Patey, 1990].

The disadvantages (i) and (ii) imply that the IET is not accessible to the interesting and important phenomena such as the nucleation, the micelle formation, and the effects of the shear flow. The defect (iii) indicates that the comparison of the results with those by the molecular simulations is required to confirm the accuracy of the analyzed results.

1.3.2 Surface forces in fluids

In order to elucidate theoretically the origin of non-DLVO forces on the molecular level, the IET has been applied to the pure fluid systems given in Table 1.3, where a pair of either uncharged or charged large spheres (or planar walls) are immersed in a pure fluid. Following these one-component fluids, the IET was recently applied to an aqueous electrolyte solution [Kinoshita *et al.*, 1996a] and a multi-component fluid of hard-sphere mixtures which represents a cyclohexane–

octamethylcyclotetrasiloxane (OMCTS) system [Kinoshita *et al.*, 1996b] and a nonpolar liquid containing a small amount of water [Kinoshita *et al.*, 1996c; Kinoshita, 1998].

1.4 Computer simulation

1.4.1 Basics

The molecular dynamics (MD) and Monte Carlo (MC) methods have been used to simulate the molecular behavior in three states of vapor, liquid, and solid and even in the coexistance of these phases [Allen and Tildesley, 1987; Rapaport, 1995; Frenkel and Smit, 1996]. In both the methods, a large number of molecules (or particles) in a cell are considered and their interactions are calculated using the potential functions prepared. In the MC method, the molecules move one by one stochastically, by which only the static properties of an equilibrium system are obtained. In the MD method, the molecules are allowed to move according to their equations of motion. Hence, the MD simulation provides both static and dynamic properties of a system, whether the system is either in equilibrium or in non-equilibrium [Evans and Morriss, 1990]. This is the most advantageous feature in the MD method. However, the MD and MC simulations consume a large amount of computation time, because the interactions between all the pairs of molecules must be calculated.

The evaluation of intermolecular potentials is crucial in the simulation. This is not only because the potentials influence the simulation results, but also because they determine the computation time required. As the molecular model becomes more detailed and precise, the simulation becomes more realistic but more time-consuming. As far as water and organic molecules are concerned, following two

models are frequently used, depending on the systems and phenomena to be examined.

Atomistic model. In an atomistic (or realistic) description, molecules are modeled as realistically as possible by use of stretching, bending, and torsional potentials between bonding atoms, and Lennard-Jones and Coulomb potentials between non-bonding atoms. Several groups have proposed the different atomistic models such as MM3 [Allinger *et al.*, 1989], AMBER [Weiner *et al.*, 1986], CHARMm [Brooks *et al.*, 1983], Dreiding [Mayo *et al.*, 1990], TRIPOS [Clark *et al.*, 1989], and OPLS [Jorgensen and Tirado-Rives, 1988].

Simple model. Molecules in the simple model are described on the basis of the following idea: molecular details are ignored except the most characteristic features such that the universal properties of systems are produced at least qualitatively. Then, an oil/water/amphiphile system is mimicked by using "waterlike" particles, "oillike" particles, and "amphiphilelike" molecules composed of the waterlike and oillike particles [Telo da Gama and Gubbins, 1986; Smit, 1988; Smit *et al.*, 1990].

1.4.2 Water at solid surfaces

In late 1970s, molecular simulations were applied to a solid/liquid interface. Many simulations have been performed to elucidate the features of water mainly near the hydrophobic surfaces and the metal electrodes as shown in Table 1.4. On the other hand, very few studies have been reported on non-metallic hydrophilic surfaces because of the various properties of the material surfaces and the difficulty in modeling. Recently, hydrophilic interfaces have been simulated extensively as given in Table 1.4.

It was found that the density profile of water molecules oscillates in the three layers next to the metallic or hydrophilic surface, accompanying the significant structural change, and that the diffusion of water molecules near the surface is very

TABLE 1.4: Simulations of water at solid surfaces

Surface property	Material	Reference
Hydrophobic	Hydrocarbon	Lee *et al.* [1984], Lee and Rossky [1994]
	Carbon	Zhu and Robinson [1991]
Hydrophilic	NaCl	Anastasiou *et al.* [1983]
	MgO	McCarthy *et al.* [1996]
	SiO_2, Lecithin	Kjellander and Marcelja [1985a, 1985b]
	Hydroxylated silica	Lee and Rossky [1994]
	Urea	Boek *et al.* [1992]
Metallic	Pt	Spohr [1989, 1990], Raghavan *et al.* [1991a, 1991b]
	Ag, Cu, Ni	Siepmann and Sprik [1995]

sensitive to the nature of the surface. The density oscillation was confirmed experimentally by X-ray scattering measurements of water at charged Ag(111) surfaces [Toney *et al.*, 1994]. In the case of the hydrophobic surface, the "icelike" structure of water was simulated in the interfacial region, which was verified experimentally also [Iiyama *et al.*, 1995; Bellissent-Funel *et al.*, 1996].

1.4.3 Ion adsorption on solid surfaces in water

In addition to the characteristics of a solid/liquid interface, the ionic behavior near the interface play an important role in many industrial processes, such as the dispersion of colloidal particles, the membrane separation, the electrode reactions, and the crystal growth.

To understand the behavior of hydrated ions near a solid surface in water, molecular simulations were carried out mainly for the smooth wall and the atomistic surface of Pt(100), as summarized in Table 1.5. In most simulations, the ionic behavior was investigated only near the surface, but the following

TABLE 1.5: Simulations of ion adsorption on solid surfaces in water

Surface model	Ion	Reference
Smooth wall	Li^+, I^-	Spohr and Heinzinger [1986]
	Na^+	Matsui and Jorgensen [1992]
	Li^+, F^-, Cl^-, Br^-, I^-	Glosli and Philpott [1992, 1993a, 1993b]
Pt(100)	Na^+, Cl^-	Rose and Benjamin [1991, 1993];
	I^-	Spohr [1993]
	Li^+, I^-	Perera and Berkowitz [1993]
	Li^+, I^-	Heinzinger [1996]

simulations were performed to know the potential of the ion positioned in the region from the interface to the bulk. The free energy profiles for ionic adsorption onto the water/Pt(100) interface were calculated to examine how stably the ion adsorbs on the surface [Rose and Benjamin, 1991; Spohr, 1993; Perera and Berkowitz, 1993]. The profiles in tetrahydrofuran as well as in water were determined to investigate how the profiles are influenced by the characteristics of solvent molecules [Matsui and Jorgensen, 1992]. However, it is still unclear how the ionic behavior at the interface is influenced by the properties and structures of the solid surface.

1.4.4 Complex fluids

Surfactant (or amphiphilic) molecules play an important role in the vast region of material industry: for example, (i) surfactants assemble spontaneously in solutions to form micelles, bilayers, and vesicles; (ii) surfactants adsorb at oil/water interfaces to reduce the interfacial tension; and (iii) surfactants adsorb onto solid surfaces to change the nature of the surfaces. These characteristics of surfactants have been investigated mainly by experimental methods, but the underlying physics is still poorly understood on the molecular level. Recently because

TABLE 1.6: Atomistic simulations of various amphiphilic systems

System	Reference
Micelle	Watanabe *et al.* [1988],Watanabe and Klein [1991], Wendoloski *et al.* [1989], Shelley *et al.* [1993], Laaksonen and Rosenholm [1993], Böcker *et al.* [1994], MacKerell [1995], Griffiths and Heyes [1996]
Monolayer at air/water interface	Bareman and Klein [1992], Böcker *et al.* [1992], Siepmann *et al.* [1994], Tarek *et al.* [1995], Schweighofer *et al.* [1997]
Monolayer at liquid/liquid interface	Schweighofer *et al.* [1997], Urbina-Villalba *et al.* [1997]
Monolayer at solid/liquid interface	Bandyopadhyay *et al.* [1998b]
Self-assembled monolayer	Siepmann and McDonald [1993], Mar and Klein [1994]
Bilayer	Marrink and Berendsen [1994], Heller *et al.* [1993], Shinoda *et al.* [1997]

computational power has advanced, molecular simulations can be applied even to the amphiphilic behavior in various environments, as described below.

As for the atomistic model, a number of simulations have been implemented on such systems as summarized in Table 1.6 and quantitative and detailed molecular information about the real systems is estimated. But unfortunately these atomistic simulations are limited within a few nanoseconds and this time scale is too short to examine the important behavior of micellar solutions, such as the surfactant exchange, or the micellar formation and breakdown that may occur on the time scale of milliseconds.

As for the simple model, Larson performed the lattice MC simulations for oil/water/amphiphile systems and observed that the amphiphiles form spontaneously spheres, cylinders, lamellas, and more complex phases [Larson, 1994, 1996]. Smit and co-workers performed a series of MD simulations and reported as follows:

(i) Surfactants adsorb at the oil/water interface and consequently reduce the interfacial tension, where this reduction becomes larger as the surfactant concentration is higher or the surfactant has a longer tail chain [Smit, 1988; Smit *et al.*, 1990, 1991].

(ii) The molecular structure of surfactants influences the shape of self-assembled micelles [Smit *et al.*, 1993b; Esselink *et al.*, 1994; Karaborni *et al.*, 1994].

(iii) An oil droplet is solubilized in a micellar solution [Karaborni *et al.*, 1993].

The point to note is that the size distribution of surfactant aggregates and the critical micelle concentration (CMC) have been also evaluated by these simulations, which are not obtained by the atomistic simulations because of the lack of the computational power [Larson, 1992; Smit *et al.*, 1993a; Rector *et al.*, 1994; Brindle and Care, 1992; Desplat and Care, 1996; Wang *et al.*, 1993; Haliloglu and Mattice, 1994]. All these results support that the simple description of amphiphilic systems can capture, at least qualitatively, most of the underlying physics in the systems.

Further details of complex fluid simulations are well reviewed elsewhere [Klein, 1992; Smit, 1993; Pastor, 1994; Karaborni and Smit, 1996; Tobias *et al.*, 1997; Larson, 1997; Bandyopadhyay *et al.*, 1998a].

1.4.5 Surface forces in fluids

Since 1980, the interaction forces between neutral planar walls in a fluid have been calculated, as summarized in Table 1.7. In these simulations, the molecular film confined between the walls must be in equilibrium with the bulk fluid. Hence, the grand canonical ensemble and the test particle insertion method were employed in most of the studies. A new statistical ensemble [Bordarier *et al.*, 1997] and a new MD cell [Wang *et al.*, 1994; Gao *et al.*, 1997] were also developed for this purpose. However, in the author's opinion it seems rather difficult to apply these

TABLE 1.7: Surface forces in various fluids evaluated by simulations

Fluid	Reference
Lennard-Jones particle	Snook and van Megen [1980], Magda *et al.* [1985], Bérard *et al.* [1993], Bordarier *et al.* [1997], Gao *et al.* [1997], Schoen and Diestler [1997]
Mixture of Lennard-Jones particles	Somers *et al.* [1993]
Ellipsoidal Gay–Berne particle	Gruhn and Schoen [1997, 1998a, 1998b]
Dipolar Lennard-Jones particle	Han *et al.* [1993]
Waterlike hard-sphere	Luzar *et al.* [1987]
Alkane	Wang *et al.* [1994], Gao *et al.* [1997], Dijkstra [1997]

methods to a mixture and a complex fluid.

1.5 Objective of this work

For the accurate material processing, it is important to understand systematically the interaction between solid surfaces in a fluid and the interfacial microstructure, as described in Section 1.1. Although these problems have been investigated experimentally, the behavior of individual molecules near the interface is still poorly understood. The theoretical method and the molecular simulation also have been applied to the problems, but unfortunately the studies were not systematic because the applications were limited to a simple system.

The objective of this dissertation is to elucidate systematically the behavior of water molecules, ions, and surfactants near a solid surface and the interaction forces between the surfaces using MD simulations. The author expects that this work can give the fundamental and important insight into the precise control of production processes of particulate materials.

This dissertation is composed of three Parts (I–III) and eight Chapters (1–8) as follows:

In **Part I (Chapters 2 and 3)**, the behavior of water molecules near a solid surface is examined using the atomistic model. **Chapters 2** and **3** deal with water near the hydrocarbon and NaCl-crystal surfaces, respectively, which are typical hydrophobic and hydrophilic surfaces. The characteristics of water molecules at these surfaces are investigated and compared in detail in terms of the interfacial structure and diffusion of water molecules and the hydrogen-bonding network. How the difference in the nature of hydrophobic and hydrophilic surfaces influences the properties of water molecules is also discussed.

In **Part II (Chapters 4 and 5)**, the adsorption of ions and surfactants onto liquid/solid interfaces is investigated. In **Chapter 4**, the simulation developed in Chapter 3 is extended to investigate the ionic behavior near the interface. The adsorption of Na^+ and Cl^- ions onto the NaCl-crystal surfaces in water is examined in terms of the free energy profiles for adsorption. It is clarified how stably the ions are adsorbed on the surfaces and how the adsorption behavior is influenced by the size of the ions and the detailed structure of the surfaces.

In **Chapter 5**, the adsorption of surfactants on a solid surface in water is examined. At the begining, the simple description of water, oil, and surfactant molecules and solid surfaces is developed to make the simulation possible within the limits of the present computational power. This simple model is verified by comparing the results with those by the atomistic model. Then, the surfactant adsorption onto the hydrophobic and hydrophilic walls in water is simulated. The mechanism of the adsorption and aggregation of surfactants on the surface is proposed, and how the mechanism is influenced by the concentration and molecular structure of surfactants is discussed in detail. These results are critically compared with the recent AFM measurements.

In **Part III (Chapters 6 and 7)**, the interaction force between macroscopic colloidal particles in a fluid is investigated systematically. The new computational technique to evaluate surface forces in a fluid is proposed in **Chapter 6**. Using this evaluation method as well as the simple model given in Chapter 5, the interaction forces between colloidal particles in simple fluids and alcohol–water mixtures are calculated in **Chapters 6** and **7**, respectively. These results are compared in detail with the corresponding SFA and AFM measurements.

Finally, **Chapter 8** discusses all the results in this thesis to give conclusions. The perspectives in the MD method to investigate the effects of a non-equilibrium field are also given.

Part I

Water at Solid Surfaces

2
Water at Hydrophobic Surfaces
—Smooth Hydrocarbon Surfaces—

2.1 Introduction

In the first two chapters, the basic characteristics of water at hydrocarbon and NaCl-crystal surfaces are investigated and compared in detail, which are typical hydrophobic and hydrophilic surfaces, respectively. Although simulations of the same systems were already reported as shown in Table 1.4, the results seem to be insufficient and nonsystematic. Hence, the purpose of Chapters 2 and 3 is not only to give the detailed and systematic information, but also to answer the question, "what is the essential nature of water at the hydrophobic and hydrophilic surfaces?" Note that the wisdom obtained helps the author to construct the *coarse* model of water, oil, and surfactant molecules and solid surfaces, as is described in Chapter 5.

2.2 Basics of molecular dynamics method

2.2.1 Intermolecular potentials

1) Atoms

Consider first the simple case of a system containing N atoms. The potential energy is formally written as

$$U_N = \sum_i u_1(\mathbf{r}_i) + \sum\sum_{i<j} u_2(\mathbf{r}_i, \mathbf{r}_j) + \sum\sum\sum_{i<j<k} u_3(\mathbf{r}_i, \mathbf{r}_j, \mathbf{r}_k) + \cdots , \tag{2.1}$$

where the first term represents the effect of an external field on the system and the remaining terms represent interparticle interactions. The second term denotes the pair potentials, which depend only on the magnitude of the pair separation $r_{ij} = |\mathbf{r}_i - \mathbf{r}_j|$. It is believed that the pair term contributes to more than 80 % of the total interparticle energy, compared with the three-body and higher-order terms. In practice, the calculation of the three-body term is very time-consuming on a computer.

The interparticle potential generally used in computer simulations is the *effective* pair potential $u_2^{\text{eff}}(r_{ij})$. Accordingly, Equation (2.1) is rewritten by

$$U_N \approx \sum_i u_1(\mathbf{r}_i) + \sum\sum_{i<j} u_2^{\text{eff}}(r_{ij}) . \tag{2.2}$$

The effective pair potential is carefully determined so as to reproduce experimental data of the system employed. This indicates that the effective pair potential includes the many-body effects approximately and is different from the true two-body potential $u_2(r_{ij})$. For simplicity, the notation $u(r_{ij})$ or $u(r)$ is used in this dissertation.

2) Small molecules

Secondly, consider polyatomic molecules that can be treated as a rigid body satisfactorily (e.g., N_2, CO_2, H_2O, and CH_4). A model molecule is composed of interaction sites, which are usually centered on the positions of the nuclei in the real molecule. The interaction between rigid molecules i and j is a complicated function of their relative positions $\mathbf{r}_i$, $\mathbf{r}_j$ and orientations Ω_i, Ω_j. In practice, the intermolecular potential is a sum of pairwise interactions between site a in molecule i, at position $\mathbf{r}_{ia}$, and site b in molecule j, at position $\mathbf{r}_{jb}$:

$$u(\mathbf{r}_i, \mathbf{r}_j, \Omega_i, \Omega_j) = u(\mathbf{r}_{ij}, \Omega_i, \Omega_j) = \sum_{a \in i} \sum_{b \in j} u_{ab}(r_{ab}) , \tag{2.3}$$

where u_{ab} is the pair potential between sites a and b, and r_{ab} represents the site–site separation $|\mathbf{r}_{ia} - \mathbf{r}_{jb}|$.

3) Large molecules

For larger molecules it is necessary to consider the internal motions of stretching, bending, and torsion. The torsional potential is the most important, because it largely influences the molecular conformations; for example, *trans* and *gauche* conformers of *n*-butane. Further details of the intermolecular potentials are well documented in the recent books [Allen and Tildesley, 1987; Sprik, 1993; Rapaport, 1995; Heyes, 1998].

2.2.2 Periodic boundary conditions

The size of the system employed is limited by the computational power. The largest number of atoms simulated is 10^6–10^7 up to date, while a real material is composed of about 10^{23} atoms or molecules. This indicates that the system simulated is affected by the effects of the finite size and the surface. To eliminate these effects, the periodic boundary conditions are usually used. The conditions are not necessarily imposed in all the dimensions and frequently applied in one or two dimensions, depending on phenomena to be simulated.

As shown in Figure 2.1, molecules in a part of a real material are considered, whose number is about 10^2–10^5. The molecules are positioned in a box (i.e., the basic cell), which is surrounded by the image cells. When the force acting on a molecule in the basic cell is calculated, the contribution from molecules in all the image cells is added to that in the basic cell.

For a short-range potential, the "minimum image convention" with the "spherical cutoff" is practiced approximately. In this procedure, a molecule interacts only with the nearest molecules irrespective of whether they reside in the basic cell or one of the neighboring cells, only when the separations are less than

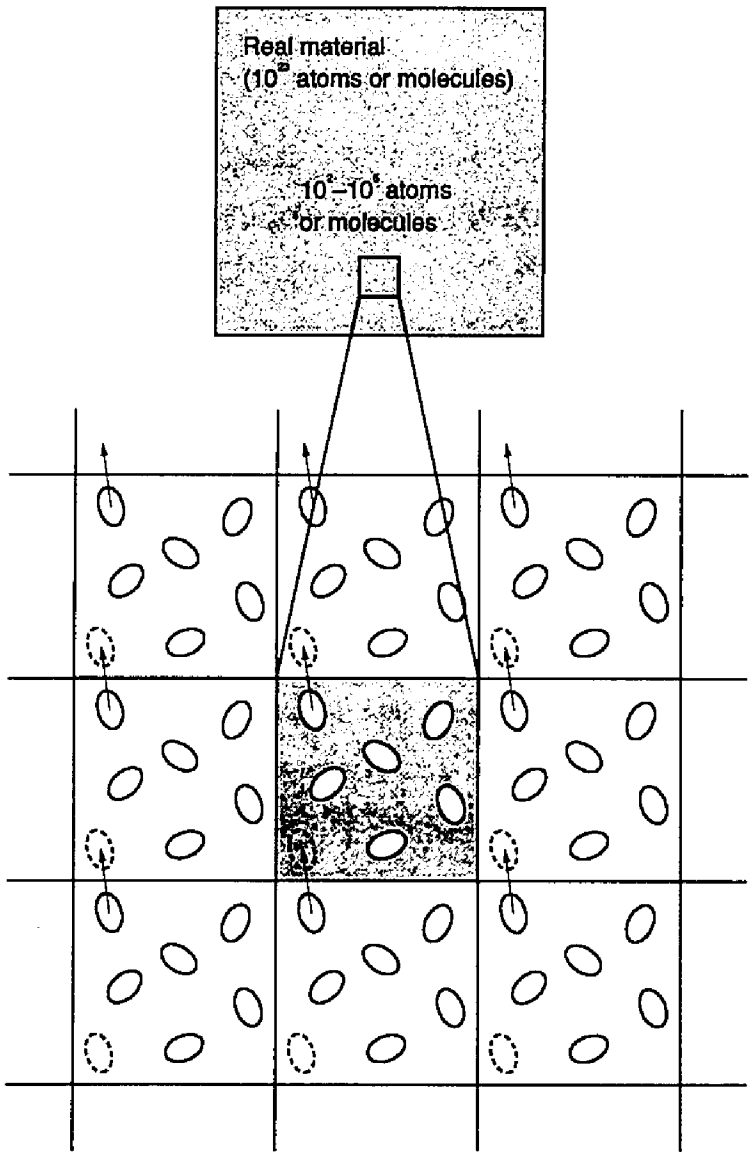

Figure 2.1. Periodic boundary system, in which the basic cell is surrounded by the image cells. A two-dimensional system is illustrated for clarity.

cutoff distance R^{cut}. When a rectangular cell with dimensions $L_x \times L_y \times L_z$ is given, R^{cut} must satisfy the following relation for consistency with the minimum image convention:

$$R^{cut} < \frac{1}{2} \min(L_x, L_y, L_z). \tag{2.4}$$

When a long-range potential is employed with three-dimensional periodicity, the Ewald method is usually applied other than the above cutoff procedure as described in Section 2.3.3.

2.2.3 Equations of motion

The equations of motion depend on the molecular model and statistical ensemble employed [Allen and Tildesley, 1987; Rapaport, 1995; Frenkel and Smit, 1996]. The author here describes only a simulation method of non-linear rigid molecules in a microcanonical (NVE) ensemble, where the number of molecules N, the volume V, and the total energy E are constant. The differential equations to be solved are a Newton–Euler equation of motion:

$$m \frac{\mathrm{d}^2 \mathbf{r}_i}{\mathrm{d}t^2} = \mathbf{F}_i, \tag{2.5}$$

$$\mathbf{I} \cdot \frac{\mathrm{d}\omega_i}{\mathrm{d}t} = \mathbf{A}_i \cdot \mathbf{T}_i + \omega_i \times (\mathbf{I} \cdot \omega_i). \tag{2.6}$$

Here m is the mass of a molecule. $\mathbf{I}$ is the inertia moment along the principal axes, which consists of only diagonal elements (i.e., I_{xx}, I_{yy}, and I_{zz}), and ω_i is and the corresponding angular velocity. $\mathbf{A}_i$ represents the rotation matrix given by the Euler angles to convert the space-fixed coordinate into the body-fixed coordinate. $\mathbf{F}_i$ and $\mathbf{T}_i$ represent the force and torque acting on the center-of-mass of molecule i, respectively, and are given by

$$\mathbf{F}_i = \sum_{a \in i} \mathbf{F}_{ia} = \sum_{a \in i} \left(- \frac{\partial U_N}{\partial \mathbf{r}_{ia}} \right), \tag{2.7}$$

$$\mathbf{T}_i = \sum_{a \in i} (\mathbf{r}_{ia} - \mathbf{r}_i) \times \mathbf{F}_{ia} = \sum_{a \in i} (\mathbf{r}_{ia} - \mathbf{r}_i) \times \left(- \frac{\partial U_N}{\partial \mathbf{r}_{ia}} \right). \tag{2.8}$$

Equations (2.5) and (2.6) are solved numerically, where the quaternions are used as orientational parameters instead of the Euler angles. More details of this numerical procedure are given elsewhere [Allen and Tildesley, 1987; Rapaport, 1995].

2.3 Methods

2.3.1 Molecular models

1) Water–water interaction

Various models for water–water interaction have been proposed because water is a unique fluid and plays an important role in our surroundings. Water models widely used in computer simulations are ST2 [Stillinger and Rahman, 1974], MCY [Matsuoka *et al.*, 1976], SPC [Berendsen *et al.*, 1981], SPC/E [Berendsen *et al.*, 1987], and TIP4P [Jorgensen *et al.*, 1983].

In this dissertation, the SPC/E model is selected not only because it faithfully reproduces the bulk property of water, but also because it is efficient in calculation. As illustrated in Figure 2.2, the SPC/E water is composed of three sites, whose internal geometry is rigid with 0.1 nm distance between O and H atoms and 109.74° angle (i.e., a tetrahedral angle) between two OH bonds [Berendsen *et al.*, 1987]. The water–water potential is a sum of these site–site interactions:

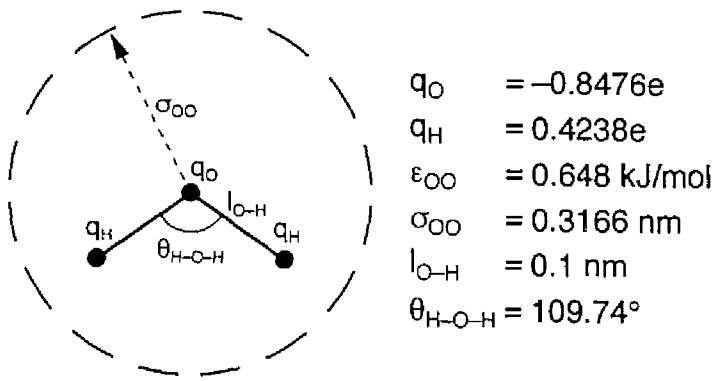

Figure 2.2. SPC/E water model, which is rigid with three sites.

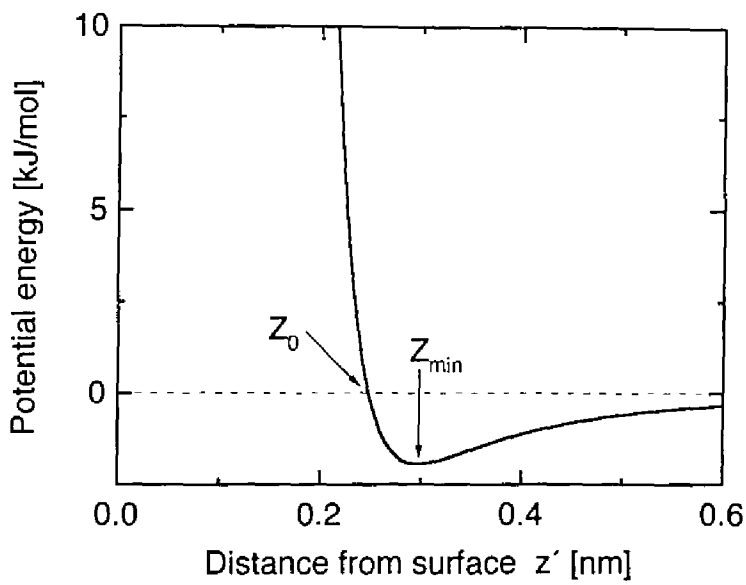

Figure 2.3. Interaction energy between a water molecule and the hydrocarbon wall, as a function of the distance from the surface z'. The outermost plane of atoms in the wall is positioned at $z' = 0$. The hydrocarbon wall is treated as a flat structureless plate. The water–surface interaction does not depend on the molecular orientation (see the text).

$$u_{ij}^{WW}(\mathbf{r}_{ij}, \Omega_i, \Omega_j) = \sum_{a\in i}\sum_{b\in j}\frac{q_a q_b}{r_{ab}} + 4\varepsilon_{OO}\left[\left(\frac{\sigma_{OO}}{r_{OO}}\right)^{12} - \left(\frac{\sigma_{OO}}{r_{OO}}\right)^{6}\right], \qquad (2.9)$$

where the subscript OO represents oxygen–oxygen interactions, q_a is the point charge on site a in molecule i, and ε and σ are the energy and size parameters for the Lennard-Jones (12–6) potential, respectively. On the right-hand side of Equation (2.9), the first term represents the Coulomb interactions and the second term describes the repulsion by the electron cloud overlapping.

The values of parameters for the point charges and the overlap repulsion are determined such that the thermodynamic quantities of the model water are consistent with the experimental data; that is, $q_O = -2q_H = -0.8476e$, $\varepsilon_{OO} = 0.648$ kJ/mol, and $\sigma_{OO} = 0.3166$ nm. The anisotropy of hydrogen bonds is represented implicitly via the site–site interactions. The hydrogen-bonding energy between two SPC/E water molecules in their most favorable configuration is found to be –30.0 kJ/mol. More details are given in the original papers [Berendsen *et al.*, 1981, 1987].

2) Water–surface interaction

The interaction between a water molecule and a hydrocarbon surface is represented by the (9–3) potential [Lee *et al.*, 1984]:

$$u^{wall}(z) = \frac{A}{z^9} - \frac{B}{z^3}, \qquad (2.10a)$$

$$A = 17.477 \times 10^{-6} \text{ kJ nm}^9/\text{mol},$$
$$B = 76.144 \times 10^{-3} \text{ kJ nm}^3/\text{mol}. \qquad (2.10b)$$

where z is the perpendicular distance between the outermost plane of the solid wall and the center of an O atom in an SPC/E molecule. The hydrocarbon wall is treated as a flat structureless plate, because the atoms in the solid are *smeared out* in all the directions. There is no hydrogen–wall interaction, indicating that the interaction

between a single water molecule and the wall does not depend on the molecular orientation. This is because the diameter of the H atom and the interaction with the wall are, in practice, negligible compared with those of the O atom.

The values of parameters A and B given in Equation (2.10b) are appropriate for a material like paraffine [Lee *et al.*, 1984]. The potential has a minimum of –1.93 kJ/mol at z = 0.297 nm (= Z_{min}) and exhibits the zero value at z = 0.247 nm (= Z_0), as shown in Figure 2.3. It is worth noting that the binding energy of –1.93 kJ/mol is much smaller in absolute value than the hydrogen-bonding energy of –30.0 kJ/mol, which makes the nature of the surface hydrophobic.

2.3.2 Basic cell

Figure 2.4 illustrates the unit cell with the dimensions of $L_x \times L_y \times L_z$ = 1.862 nm × 1.862 nm × 2.362 nm, where the origin of coordinates is taken at the center of the cell. The outermost layers of two solid walls are parallel to the xy plane and located at $z = -L_z/2$ and $+L_z/2$, between which 216 water molecules are confined. The periodic boundary conditions are applied in the directions x and y. A water molecule whose O atom is positioned at z experiences the external potential, $u^{ext}(z)$, given by the superposition of u^{wall} from the walls:

$$u^{ext}(z) = u^{wall}(z + L_z/2) + u^{wall}(L_z/2 - z)\,. \tag{2.11}$$

The profile of $u^{ext}(z)$ is given in Figure 2.5. The effective width of the cell in the z direction is defined as the separation between points at $z = -L_z/2 + Z_0$ and $L_z/2 - Z_0$, where each u^{wall} on the right-hand side of Equation (2.11) is zero.

2.3.3 How to handle long-range forces

1) Basics

The Ewald lattice summation technique has been commonly used to calculate the

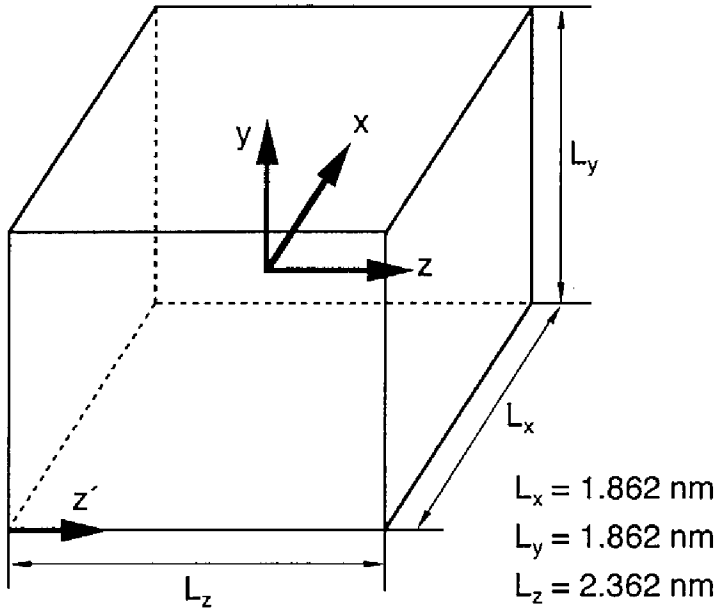

Figure 2.4. Basic cell for MD simulation. Shaded plates represent the outermost plane of atoms in the hydrocarbon wall.

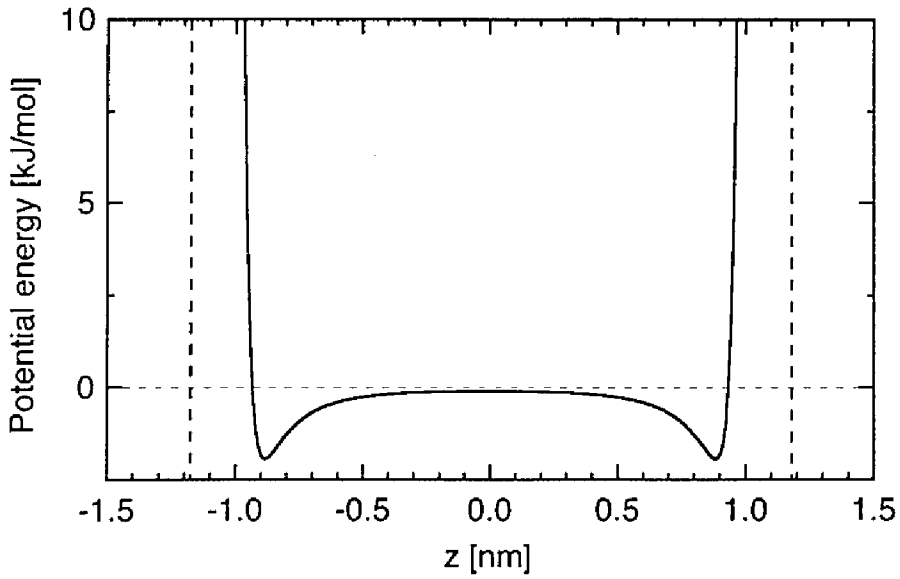

Figure 2.5. External potential from the two planar walls of the basic cell when the O atom of a water molecule is located at z (see Figures 2.3 and 2.4). Vertical dashed lines denote the outermost plane of atoms in the wall.

long-range Coulomb interactions in a system, which is periodic in all three dimensions [Allen and Tildesley, 1987]. However, the Ewald method can not be applied straightforward to an *inhomogeneous* system whose periodicity exists only in two dimensions, as shown in Figure 2.4.

To calculate the Coulomb interactions in the system with two-dimensional periodicity, several groups developed the 2D-Ewald methods [Heyes and van Swol, 1981; Heyes, 1994; Rhee *et al.*, 1989; Hautman and Klein, 1992]. Recently, Lekner [1989, 1991] suggested a different technique. Unfortunately, these methods seem to have the following defects:

(i) Programming is not easy since the algorithm is much complicated.

(ii) Enormous computation time is needed.

(iii) It is still unclear whether the methods can reproduce faithfully the behavior of the anisotropic systems or not.

Alternatively, the Coulomb interactions are truncated at a finite spherical radius of R^{cut}, which typically ranges 0.8–2.0 nm. There are three main spherical truncation methods:

(i) Potential shifting method, where the electrostatic potential between each pair is scaled by $[1 - (r/R^{cut})^2]^2$.

(ii) Force switching method, where the force is smoothly truncated to zero at $r = R^{cut}$ over a given range (typically 0.1–0.2 nm).

(iii) Force shifting method, where a constant is added to the force such that both the force and potential are zero at $r = R^{cut}$.

Further details of these methods are given elsewhere [Steinbach and Brooks, 1994].

2) Force shifting method

The force shifting method is employed in this chapter, firstly because it is easy in programming and secondly because it gives the local properties of water, which

are almost the same as those by the 3D-Ewald method, as is shown below. The interaction potential $u(r)$ is transformed into the shifted-force potential $u^{\mathrm{FSH}}(r)$ by the force shifting procedure:

$$u^{\mathrm{FSH}}(r) = \begin{cases} u(r) - u(R^{\mathrm{cut}}) - \left(\dfrac{\mathrm{d}u(r)}{\mathrm{d}r}\right)_{r=R^{\mathrm{cut}}} (r - R^{\mathrm{cut}}), & r \le R^{\mathrm{cut}}, \\ 0, & r > R^{\mathrm{cut}}. \end{cases} \tag{2.12}$$

When the Coulomb interaction of $u(r) = q_i q_j / r$ is employed, Equation (2.12) yields

$$u^{\mathrm{FSH}}(r) = \begin{cases} \dfrac{q_i q_j}{r}\left(1 - \dfrac{r}{R^{\mathrm{cut}}}\right)^2, & r \le R^{\mathrm{cut}}, \\ 0, & r > R^{\mathrm{cut}}. \end{cases} \tag{2.13}$$

In this chapter, the Coulomb and non-Coulomb interactions are handled by the force shifting method and the simple truncation procedure, respectively, in which the site–site interactions are calculated only when the center-to-center distance between molecules is less than or equal to R^{cut}.

3) Test of the force shifting method

Before the force shifting method is applied to the system with two-dimensional periodicity, it is used to simulate 216 SPC/E water molecules in the three-dimensional periodic cell at 1 g/cm^3 and 298 K. The results obtained are compared with those from the separate simulation using the 3D-Ewald technique which is the most reliable method in this case. Simulation details are given in Sections 2.3.4 and 3.2.4.

Figure 2.6 shows the pair correlation functions of O–O, O–H, and H–H. These indicate that the local structure of water is quite similar to that by the Ewald method, although the functions exhibit a little bit less amplitude. The self-diffusion coefficient is also evaluated to be 3.0×10^{-5} cm^2/s. The value is 20 % larger than that of 2.5×10^{-5} cm^2/s by the Ewald method. The slight discrepancy in these

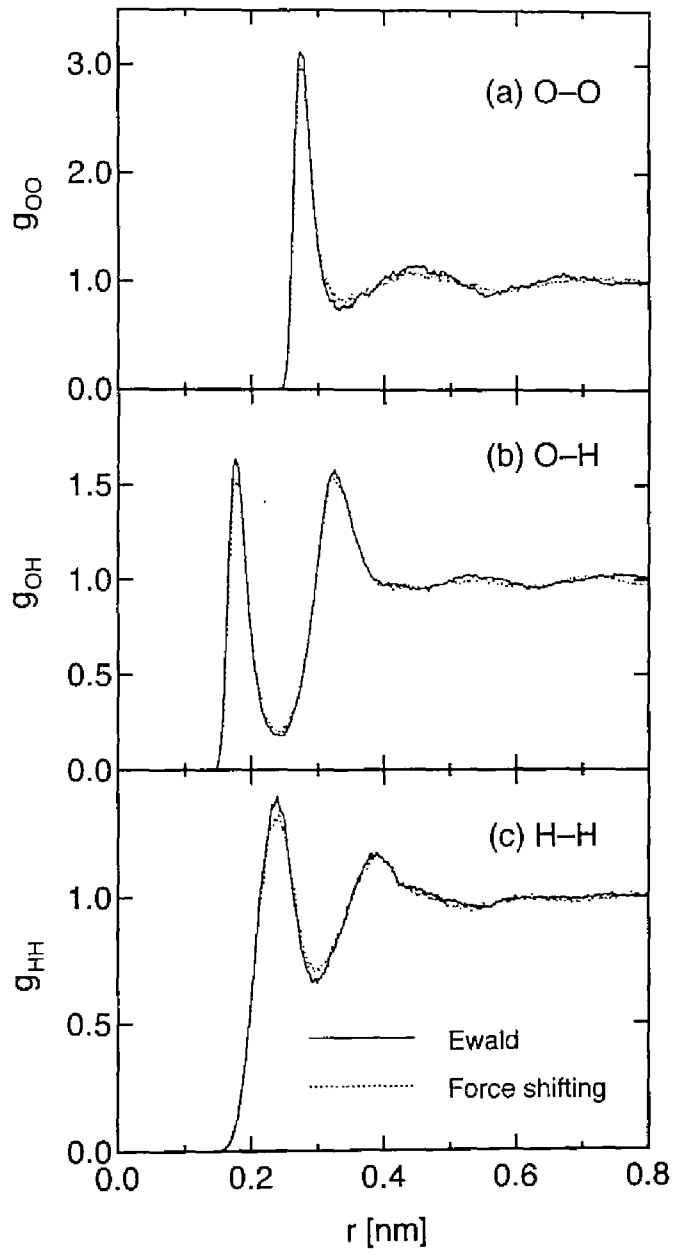

Figure 2.6. Site–site pair correlation functions of SPC/E water at 1 g/cm^3 and 298 K. Solid and dotted lines indicate the simulations using the Ewald method and the force shifting method, respectively.

properties comes from the use of Equation (2.13) that underestimates the interactions between water molecules even at small separations. Although application of the force shifting method to the Coulomb interactions is on the coarse side, this method is sufficiently available to capture, at least qualitatively, the local properties of water. The truncation methods have been further investigated in other studies [Prevost *et al.*, 1990; Feller *et al.*, 1995].

2.3.4 Simulation details

The MD simulation is performed using a program based on MDMPOL [Smith and Fincham, 1982], which is used also in Chapters 3 and 4 after being modified according to the purpose of each chapter. As described above, the short-range and long-range interactions are handled using the simple truncation and force shifting procedures with $R^{cut} = 0.82$ nm, respectively. The equations of motion, Equations (2.5) and (2.6), are solved using the leap-frog algorithm. The time step used is 2 fs in this chapter. More details are given elsewhere [Smith and Fincham, 1982; Allen and Tildesley, 1987].

The simulation is performed as follows:

(i) All the 216 molecules are placed at $6 \times 6 \times 6$ lattice points in the cubic cell with the dimensions 1.862 nm × 1.862 nm × 1.862 nm and the three-dimensional periodicity, which corresponds to the density of 1 g/cm^3.

(ii) The system is allowed to evolve for 50 ps, during which the temperature is kept at 298 K by velocity scaling.

(iii) Then, the two planar walls are inserted at $z = \pm 1.181$ nm and the periodicity of the direction z is removed.

(iv) After equilibration over 50 ps, the simulation is performed for 100 ps. Here, the temperature is adjusted to 298 K by velocity scaling at every 100th time step and the translational velocities of molecules are shifted at every time step

such that the center-of-mass velocity of the total system is zero in the directions x and y.

2.4 Results and discussion

In following Sections 2.4.1 to 2.4.4, the structure and dynamics of water adjacent to the hydrocarbon surface are discussed in terms of (i) density profiles of water molecules, (ii) numbers of hydrogen bonds and nearest neighbors, (iii) distributions of molecular orientations, and (iv) self-diffusion coefficients, using the averaged values at $\pm z$.

2.4.1 Density profiles of water molecules

Figure 2.7 shows the density profiles of O and H atoms as a function of z. The O profile, corresponding to the center-of-mass profile of H_2O, slightly oscillates to approach the constant value of 1 g/cm^3 from the interfacial region to the bulk region. Substantially, the surface repels water toward the bulk (i.e., the "dewetting"), although the O profile has two vague peaks next to the surface. It is known that this tendency is characteristic at the interface between water and a hydrophobic plane [Lee *et al.*, 1984; Lee and Rossky, 1994]. On the other hand, the hydrophilic surfaces tend to attract water such that about three dense layers of water molecules are formed [Spohr, 1989, 1990; Raghavan *et al.*, 1991a, 1991b; Anastasiou *et al.*, 1983; McCarthy *et al.*, 1996; Kjellander and Marcelja, 1985a; Boek *et al.*, 1992; Lee and Rossky, 1994]. The H profile rises from the zero value at the point closer to the wall than the O profile, indicating that the H atoms can approach closer to the surface than the O atoms.

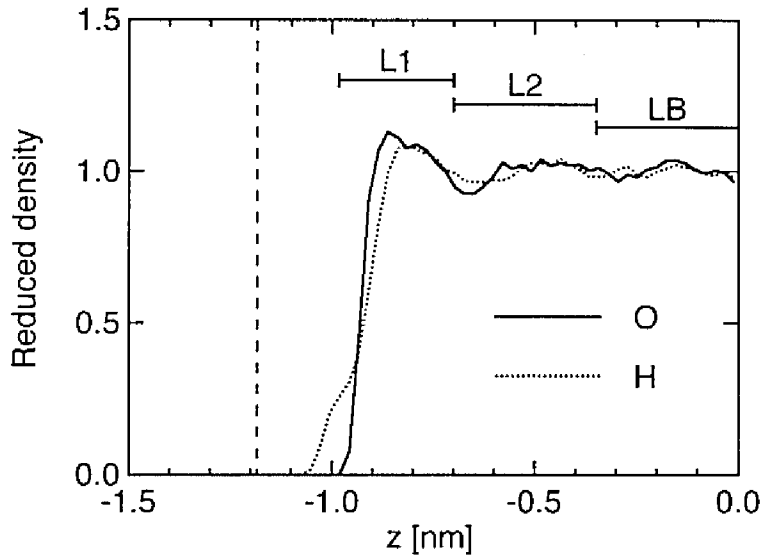

Figure 2.7. Density profiles of O and H atoms of water molecules near the hydrocarbon surface. Solid and dotted lines indicate O and H profiles, respectively. The vertical dashed line denotes the outermost plane of atoms in the wall.

2.4.2 Local coordination and hydrogen bonding

It is known that the network of hydrogen bonds between water molecules is sensitive to the environment. A pair of water molecules is regarded as nearest neighbors if their O–O distance is smaller than or equal to 0.35 nm, the distance at the first minimum of the O–O pair correlation function of SPC/E water as shown in Figure 2.6(a). Water molecules are regarded as hydrogen bonded if they are nearest neighbors and have a pair interaction energy less than or equal to the critical value of $\varepsilon_{HB} = -10$ kJ/mol, simultaneously. Figure 2.8 shows the average numbers of nearest neighbors n_{NN} and hydrogen bonds n_{HB} per water molecule as a function of z. The separate calculations suggest that the profile of n_{HB} is not influenced qualitatively by the threshold values of ε_{HB}. It is clear that the values of n_{NN} and n_{HB} in the region of $|z| < 0.6$ nm are almost constant at about 5.1 and 3.5, respectively, which agree well with those obtained in the separate simulation of the bulk water. However, the value of n_{HB} is reduced remarkably at the interface, which coincides well with the reduction of the value of n_{NN}. This decrease in n_{NN} and n_{HB} is an expected result, because a water molecule next to the wall has neighbors toward the bulk, but has no neighbor toward the surface.

The value n_{HB}/n_{NN}, which is a parameter to evaluate the fraction of hydrogen bonds out of the nearest-neighboring water molecules, is calculated as shown in Figure 2.9. It exhibits clearly that the value of n_{HB}/n_{NN} increases significantly in the interfacial region. The opposite behavior in the profiles of n_{HB} and n_{HB}/n_{NN} implies that water molecules next to the surface are hydrogen bonded with their neighbors quite efficiently. It is worth noting that similar results were reported for the immiscible liquid/liquid interfaces such as water/benzene [Linse, 1987], water/hexanol [Carpenter and Hehre, 1990], and water/chloroalkane [Benjamin, 1992; Chang and Dang, 1996]. This behavior of water molecules seems to be their self-defense against undesirable hydrophobic species. The efficient hydrogen-

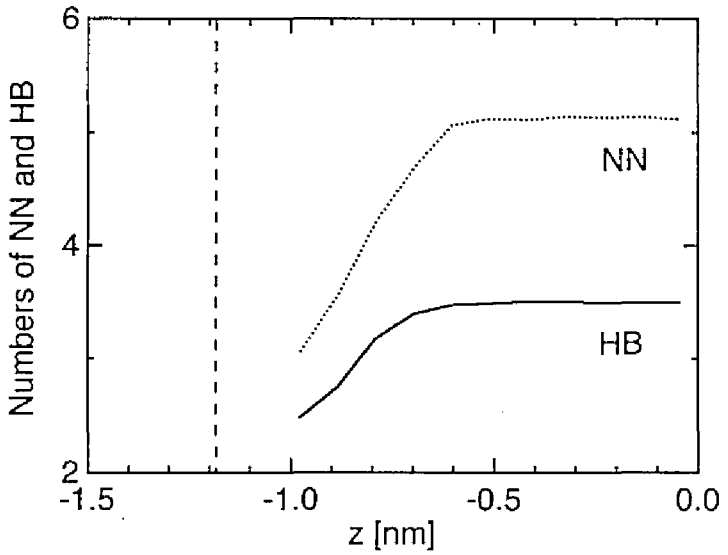

Figure 2.8. Average numbers of nearest neighbors n_{NN} and hydrogen bonds n_{HB} per water molecule. Solid and dotted lines indicate the values of n_{HB} and n_{NN}, respectively. The vertical dashed line denotes the outermost plane of atoms in the wall.

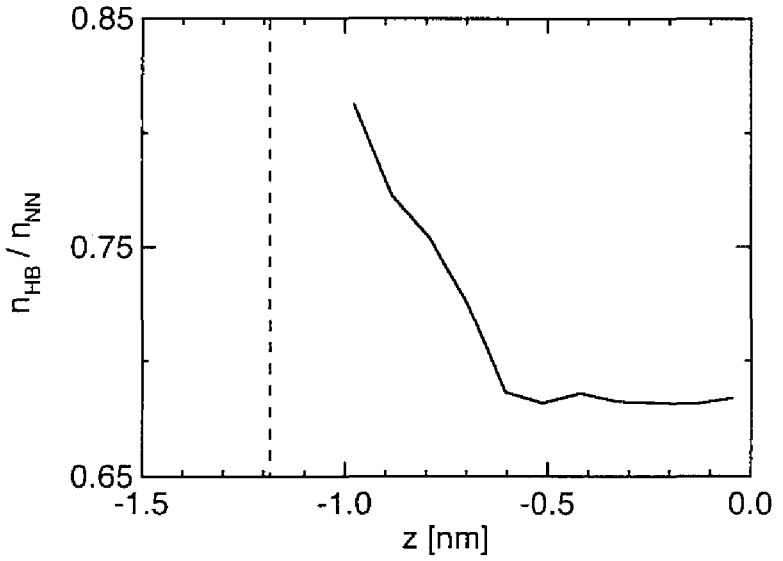

Figure 2.9. Value of n_{HB}/n_{NN} obtained from Figure 2.8, which is a parameter to estimate the fraction of hydrogen bonds out of the nearest-neighboring water molecules. The vertical dashed line denotes the outermost plane of atoms in the wall.

bonding of water at the hydrocarbon surface can be explained by the "icelike" structure formation as described below.

2.4.3 Orientational structure

Tetrahedral geometry of hydrogen bonding. The results presented above suggest a significant structural change of water next to the hydrocarbon surface, which arises from the strong water–water and weak water–surface interactions. It is known that a water molecule tends to be hydrogen bonded with the four neighbors to form a regular *tetrahedral* structure. Remember that the average number of hydrogen bonds in liquid water is 3.5 per molecule, as shown in Figure 2.8.

Judging from the tetrahedral geometry, at least one of four bonds are unavoidably broken when the planer wall is put into water, as shown in Figure 2.10. If the more hydrogen bonds are disrupted, the disadvantage to enthalpy becomes larger. In order to minimize the disadvantage of the overall system, water molecules keep away from the surface and reorient to form a well-ordered structure at the interface. The former behavior corresponds to the dewetting as mentioned in Section 2.4.1 and the latter corresponds to the icelike structure formation as illustrated in Figure 2.11 [Lee *et al.*, 1984]. This icelike structure is examined below extensively.

Definition of orientational parameters. The orientation of water molecules is investigated in detail as a function of z. For this reason, the fluid lamina is divided into the layers that are parallel to the xy plane and have a thickness of 0.093 nm, as defined in Table 2.1. Within each layer, the distributions of two orientational parameters, θ_μ and θ_{OH}, are evaluated: θ_μ is defined as the angle between the dipole vector of an H_2O and the surface normal $\mathbf{n}_z$ pointing away from the surface; and θ_{OH} is defined as the angle between the vector

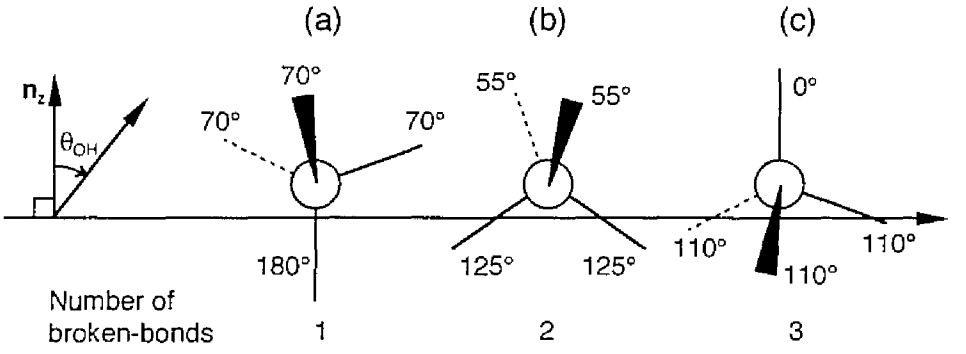

Figure 2.10. Ideal orientations of a water molecule next to the wall. In the bulk, a water molecule tends to be hydrogen bonded with the four neighbors to form a regular *tetrahedral* structure. Spheres and lines represent O atoms and hydrogen bonds, respectively. The number of bonds broken by the wall increases from (a) to (c).

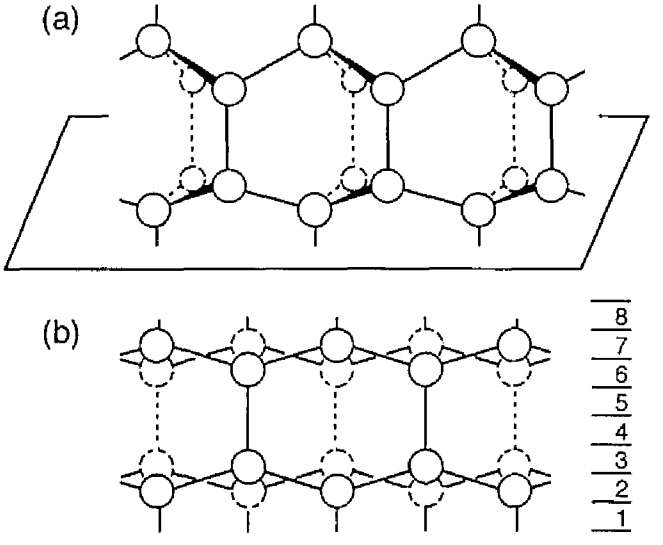

Figure 2.11. Schematic illustration of the structure of ice, after Lee *et al.* [1984]. Panels (a) and (b) show the three-dimensional structure and the two-dimensional projection, respectively. The layer intervals defined in Table 2.1 are also shown in panel (b). Spheres and lines represent O atoms and hydrogen bonds, respectively.

TABLE 2.1: Location of fluid layers used to analyze the molecular orientation

Layer number[a]	Range of |z|/nm
1	0.931–1.024
2	0.838–0.931
3	0.745–0.838
4	0.652–0.745
5	0.559–0.652
6	0.465–0.559
7	0.372–0.465
8	0.279–0.372
9	0.186–0.279
10	0.093–0.186
11	0.000–0.093

[a] The layers are parallel to the xy plane. The layer denoted 1 is closest to the wall.

of the OH bond and $\mathbf{n}_z$. The probability of angle θ_μ, $P_\mu(\theta_\mu)$, is calculated by using

$$P_\mu(\theta_\mu) = \frac{n_\mu(\theta_\mu)}{N \sin\theta_\mu \Delta\theta_\mu}, \tag{2.14}$$

where $n_\mu(\theta_\mu)$ is the number of the molecules with the angle between $\theta_\mu - \Delta\theta_\mu/2$ and $\theta_\mu + \Delta\theta_\mu/2$, and N is a normalizing constant chosen so that

$$\int_{0°}^{180°} P_\mu(\theta_\mu)\, d\theta_\mu = 1. \tag{2.15}$$

In the same way, the probability of angle θ_{OH}, $P_{OH}(\theta_{OH})$, is calculated.

Orientational distributions. The frequency distributions of P_μ and P_{OH} are shown in Figure 2.12. P_{OH} has two maxima at $\theta_{OH} = 70°$ and 180° for layer 1 and at $\theta_{OH} = 0°$ and 110° for layers 3–4, respectively. P_μ has a maximum at $\theta_\mu = 120°$ for layer 1 and at $\theta_\mu = 80°$ for layers 3–4, respectively. The favorable orientation of molecules in layer 1 coincides well with that observed in the ideal icelike structure, as in Figures 2.10(a) and 2.11(b). This indicates that the number of hydrogen bonds broken by the wall is one per water molecule, which agrees fairly

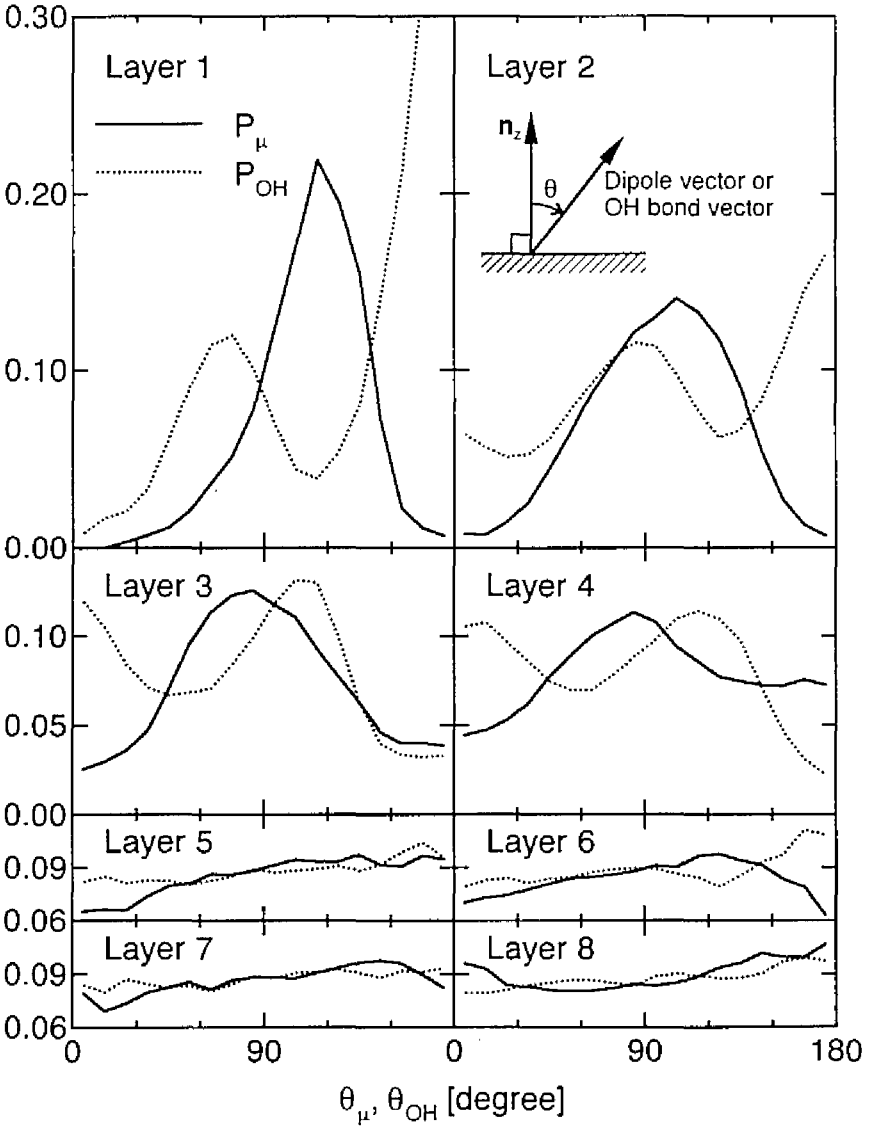

Figure 2.12. Orientational distributions $P_\mu(\theta_\mu)$ and $P_{OH}(\theta_{OH})$ of water molecules in layers 1–8 (see Table 2.1) near the hydrocarbon surface. θ_μ is defined as the angle between the dipole vector of an H_2O and the surface normal $\mathbf{n}_z$ pointing away from the surface, and θ_{OH} is defined as the angle between the OH bond vector and $\mathbf{n}_z$. Solid and dotted lines indicate distributions of P_μ and P_{OH}, respectively.

well with the value calculated by n_{HB} in Figure 2.8, that is, 2.5 – 3.5 = –1.0. The molecular orientation in layers 3–4 corresponds to that in Figures 2.10(c) and 2.10(b). The profiles of P_{OH} and P_{μ} for layer 2 are apparently symmetric with regard to $\theta_{OH} = \theta_{\mu} = 90°$. This indicates that a water molecule in layer 2 is intermediate between water molecules in layers 1 and 3 whose orientations are opposite to each other.

In the case of layers 5–8, molecules do not have their particularly favorable configurations, as seen from the vertical scales in Figure 2.12. In layer 6, however, P_{OH} has a maximum at $\theta_{OH} = 180°$ and a minimum at $\theta_{OH} = 120°$, and P_{μ} has a maximum $\theta_{\mu} = 120°$ and two minima at $\theta_{\mu} = 0°$ and 180°. The similar behavior is observed in the angular distributions in layer 1, indicating that the molecular orientation depicted in Figure 2.10(a) also appears in layer 6. It is worth noting that the 6th layer of $|z| = 0.465$–0.559 nm results in the second peak of the O atom profile next to the surface shown in Figure 2.7.

Thus, water molecules form the icelike structure with about 0.6 nm thickness near the hydrocarbon surface. This explains the efficient hydrogen-bonding at the interface shown in Figure 2.9. The icelike structure formation at the hydrophobic surface was confirmed by other simulations [Lee *et al.*, 1984; Lee and Rossky, 1994], theoretical studies [Kinoshita and Hirata, 1996], and experiments [Iiyama *et al.*, 1995; Bellissent-Funel *et al.*, 1996].

2.4.4 Diffusion

Evaluation methods. To probe the motion of water molecules near the surface, the fluid lamina is divided into the three layers, L1, L2, and LB, as defined in Figure 2.7 and Table 2.2. The self-diffusion coefficients parallel and perpendicular to the surface, D_{xy} and D_z, are calculated in the following way.

Figure 2.13 shows the lateral mean square displacement of molecules within

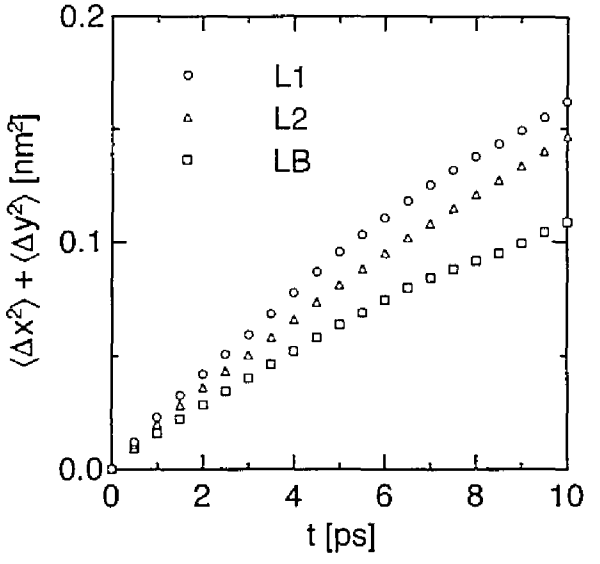

Figure 2.13. Lateral mean square displacements of water molecules within the different layers defined in Figure 2.7 and Table 2.2. Spheres, triangles, and squares indicate values for L1, L2, and LB, respectively.

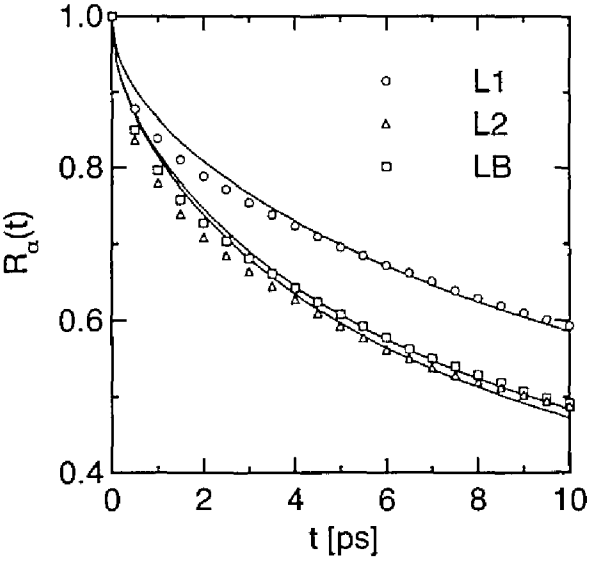

Figure 2.14. Residence autocorrelation functions, $R_\alpha(t)$, of water molecules within the different layers. Symbols are the same as in Figure 2.13. Solid lines show the fitting curves given by Equation (2.19).

TABLE 2.2: Diffusion coefficients of water molecules in the different layers near the hydrocarbon surface (in 10^{-5} cm^2/s)

Layer[a]	L1	L2	LB
D_{xy}[b]	3.7	2.8	2.5
D_z[c]	4.5	3.2	3.1
(D_z)[b]	(0.03)	(0.11)	(0.22)

[a] The range of $|z|$ is 0.70–0.98 nm for L1, 0.35–0.70 nm for L2, and 0.00–0.35 nm for LB (see Figure 2.7).
[b] Values are calculated by the mean square displacement.
[c] Values are calculated by the residence autocorrelation function.

each layer. D_{xy} is evaluated by the following equations and given in Table 2.2:

$$D_\xi = \lim_{t\to\infty} \frac{\langle |\xi(t) - \xi(0)|^2 \rangle}{2t} = \lim_{t\to\infty} \frac{\langle \Delta\xi^2 \rangle}{2t} \quad (\xi = x, y, z), \tag{2.16}$$

$$D_{xy} = \frac{1}{2}(D_x + D_y). \tag{2.17}$$

Likewise, D_z is calculated and given in the parentheses of Table 2.2. However, the values of D_z are unreasonably small compared with those of D_{xy} even in the bulklike region of LB, where water molecules are expected to have the same isotropic diffusivity as the bulk water, 3.0×10^{-5} cm^2/s. This suggests that Equation (2.16) is not appropriate, at least in this case, for evaluating the vertical diffusion coefficient of molecules within a thin film (see also Sections 3.3.6 and 5.3.1).

Alternatively, the residence autocorrelation function is introduced to quantify D_z appropriately following Sonnenschein and Heinzinger [1983]:

$$R_\alpha(t) = \mathbf{N}(0) \cdot \mathbf{N}(t) / \mathbf{N}^2(0), \tag{2.18}$$

where $\mathbf{N}(t)$ is a vector $(n_1, \ldots, n_{216})$ with $n_i = 1$ or 0 depending on whether molecule i resides in layer α or not at time t. Assuming that the molecules behave as Brownian particles and the density distribution in a layer is homogeneous at t =

0, $R_\alpha(t)$ is given by the following analytical expression derived from the diffusion equation [Sonnenschein and Heinzinger, 1983]:

$$R_\alpha(t) = \mathrm{erf}(\tau) + \frac{\exp(-\tau^2) - 1}{\sqrt{\pi}\,\tau}, \tag{2.19a}$$

$$\tau = \begin{cases} 2h / \sqrt{4D_z t} & \text{for half side closed layer,} \\ h / \sqrt{4D_z t} & \text{for open layer,} \end{cases} \tag{2.19b}$$

where h is the thickness of the layer. The half side closed layer corresponds to L1 and the open layer corresponds to L2 and LB. Equation (2.19a) is fitted to the simulated values of $R_\alpha(t)$ given by Equation (2.18) as shown in Figure 2.14 and the values of D_z are obtained as summarized in Table 2.2.

Diffusion coefficients. Table 2.2 suggests that the diffusion coefficients of water molecules increase as they approach the surface. In particular, the diffusivity in L1 increases remarkably, compared with that for the bulk water, 3.0×10^{-5} cm^2/s. The similar result was reported by Lee and Rossky [1994]. This is because the hydrogen-bonding network near the surface is disrupted, as shown in Figure 2.8 and the water–surface interaction of –1.93 kJ/mol is much weaker than the hydrogen bond of –30.0 kJ/mol, as described in Section 2.3.1. The significant increase of the vertical diffusion implies that water molecules at the interface can easily exchange themselves with those in the bulk; consequently, the icelike structure induced by the hydrocarbon surface is not necessarily stable. Unfortunately, there is no experimental data to support the high diffusivity of water molecules at the hydrophobic interface.

Table 2.2 shows also that diffusion coefficients are anisotropic even in LB. This indicates that water in LB does not display the same dynamical properties as the bulk water, although it has the same static properties as the bulk water, such as the density in Figure 2.7 and the hydrogen-bonding network in Figure 2.8.

2.5 Concluding remarks

The MD simulation of water at the hydrocarbon surface is carried out and the following conclusions are drawn.

(i) Water molecules keep away from the hydrocarbon surface not to form any adsorbed layer.

(ii) In order to minimize the hydrogen-bond breakage near the surface, water molecules form the icelike orientational structure with about 0.6 nm thickness next to the surface.

(iii) Water molecules at the interface display the high diffusivity to exchange themselves with those in the bulk, indicating that the icelike structure induced by the hydrocarbon surface is not necessarily stable.

(iv) Water in LB can be regarded as the bulk water with respect to the static properties, but not in terms of the dynamic properties.

3

Water at Hydrophilic Surfaces

—NaCl(001) and NaCl(011) Crystal Surfaces—

3.1 Introduction

The structure and dynamics of water molecules at the hydrophobic surface were discussed in the previous chapter. In this chapter, these properties at the hydrophilic surface are examined using the NaCl-crystal surface. Water/NaCl interfaces are interesting from a crystallographical point of view. An NaCl crystal is a typical crystal with various faces of different stability in water. It is known that the preferential adsorption of solvent molecules on a particular crystal face leads to the reduction of the growth rate of the face. Hence the structure and dynamics of the water/NaCl interface influence the growth rate of the crystal face and consequently determine the size, the shape, and even other properties of the crystal.

Ohtaki and co-workers [1988; Ohtaki and Fukushima, 1989] investigated the dissolution process of the cubiclike NaCl crystal with (001), (111), and (−1−1−1) faces of about 1.2×1.2 nm^2 in water and found that three Cl^- ions at the corners of the crystal dissolve into water in 7 ps and no Na^+ ion dissolves from any face. However, the interfacial features of water are still unclear, because the focus of interest was the ionic behavior rather than that the water behavior. Anastasiou *et al.* [1983] investigated the water behavior near the NaCl(001) surface and found that water molecules are adsorbed above Na^+ ions of the surface pointing their dipoles away from the surface and their motion is remarkably reduced. Unfortunately the

results seem to be deficient, because the density of water was chosen at 0.6 g/cm^3, which is much lower than the normal water density of 1 g/cm^3.

In this chapter, water/NaCl(001) and water/NaCl(011) interfaces are investigated in detail and compared. NaCl(011) is rougher in surface and lower in density than NaCl(001), although both the surfaces have their perfect crystal structures. Two types of simulations are performed to examine the following problems:

(I) The stability of the (001) and (011) faces of an NaCl crystal in water.

(II) The structure and dynamics of water molecules near these surfaces.

After confirming that both the NaCl(001) and NaCl(011) surfaces in water at 298 K are stable during the simulation, the attention is mainly focused on how water molecules at the interface are influenced by the detailed structure of the surface.

3.2 Methods

3.2.1 Molecular models

1) Ion–water interaction

The water model used is the same as described in Section 2.3.1. For sodium–water and chloride–water interactions the model proposed by Pettitt and Rossky [1986] is used, where the ion is treated as a Lennard-Jones sphere with a central unit charge. The ion–water potential is a sum of pairwise interactions between ion i, at position $\mathbf{r}_i$, and site b in SPC/E water molecule j, at position $\mathbf{r}_{jb}$:

$$u_{ij}^{\mathrm{IW}}(\mathbf{r}_{ij}, \Omega_j) = \sum_{b \in j} \left\{ \frac{q_i q_b}{r_{ib}} + 4\varepsilon_{ib} \left[\left(\frac{\sigma_{ib}}{r_{ib}} \right)^{12} - \left(\frac{\sigma_{ib}}{r_{ib}} \right)^{6} \right] \right\}, \tag{3.1}$$

where q is a point charge and r_{ib} represents the ion–site separation $|\mathbf{r}_i - \mathbf{r}_{jb}|$. The values of parameters ε_{ib} and σ_{ib} are given in Table 3.1.

TABLE 3.1: Parameters for ion–water potentials of the Pettitt–Rossky model

Ion (I)	Na^+	Cl^-
$\sigma_{IO}/10^{-10}$ m	2.72	3.55
$\sigma_{IH}/10^{-10}$ m	1.31	2.14
$\varepsilon_{IO}/10^{-21}$ J	0.93	2.5
$\varepsilon_{IH}/10^{-21}$ J	0.93	2.5

TABLE 3.2: Parameters for ion–ion potentials of the Tosi–Fumi model

	Na^+–Na^+	Na^+–Cl^-	Cl^-–Cl^-
A_{ij}	1.25	1.00	0.75
$C_{ij}/10^{-79}$ J m^6	1.68	11.2	116.0
$D_{ij}/10^{-99}$ J m^8	0.8	13.9	233.0
$(\sigma_i + \sigma_j)/10^{-10}$ m	2.340	2.755	3.170
$b/10^{-19}$ J	0.338	0.338	0.338
$\rho/10^{-10}$ m	0.317	0.317	0.317

2) Ion–ion interaction

The ion–ion interaction is modeled using the Born–Mayer–Huggins potential [Tosi and Fumi, 1964; Fumi and Tosi, 1964]:

$$u_{ij}^{II}(r) = \frac{q_i q_j}{r} + A_{ij} b \exp\left(\frac{\sigma_i + \sigma_j - r}{\rho}\right) - \frac{C_{ij}}{r^6} - \frac{D_{ij}}{r^8}, \tag{3.2}$$

where q_i is the charge on ion i, A_{ij} is the Pauling factor, and b, σ_i, ρ, C_{ij}, and D_{ij} are parameters depending the type of ion pairs. The values of parameters are listed in Table 3.2. Note that the second to fourth terms on the right-hand side of Equation (3.2) represent the Born repulsion by the electron cloud overlapping, the dipole–dipole attraction, and the dipole–quadrupole attraction, respectively.

3.2.2 H_2O–NaCl crystal interaction

To the author's knowledge, the potential for H_2O–NaCl crystal interaction based on the *ab initio* molecular orbital calculation has not been reported. Although the ion–water potentials given by Equation (3.2) were derived for Na^+ and Cl^- ions solvated in water at infinite dilution [Pettitt and Rossky, 1986], the H_2O–NaCl crystal interaction is calculated using the pair potentials; that is, the water–surface interaction is treated as "physisorption" in this study.

Figure 3.1 shows the interaction energy between an H_2O of various orientations and the NaCl surface with (001) and (011) faces, as a function of the perpendicular distance from the surface z'. The interaction energy of the H_2O above an Na^+ of the NaCl(001) surface has a minimum of –43 kJ/mol at $z' = 0.24$ nm, which agrees well with the minimum ranging from –46 to –29 kJ/mol at $z' = 0.23$ nm obtained from the *ab initio* periodic Hartree–Fock calculation [Taylor *et al.*, 1997] and the measured value of the differential heat of adsorption, 44 kJ/mol [Barraclough and Hall, 1974]. This manifests that the adsorbate–surface interaction is plausibly modeled here.

Comparison of potential curves in Figures 3.1(a) and (b) indicates that the NaCl(011) surface interacts with an H_2O more strongly than the NaCl(001). It is worth noting that in the case of NaCl(011) the binding energies of an H_2O above a midpoint of two nearest-neighboring Na^+'s and above an Na^+ are equal to –81 and –64 kJ/mol, respectively, which are several times larger in absolute value than the hydrogen-bonding energy between two H_2O's of –30.0 kJ/mol [Berendsen *et al.*, 1987]. Here it is emphasized that a slight difference in the surface geometry of crystals causes a significant change in the water–surface interaction, which leads to a considerable difference in the structure and dynamics of water molecules near the surfaces, as is discussed in Section 3.3. Note that the interaction of an H_2O with the NaCl surface is much stronger than that with the hydrocarbon surface of –1.93

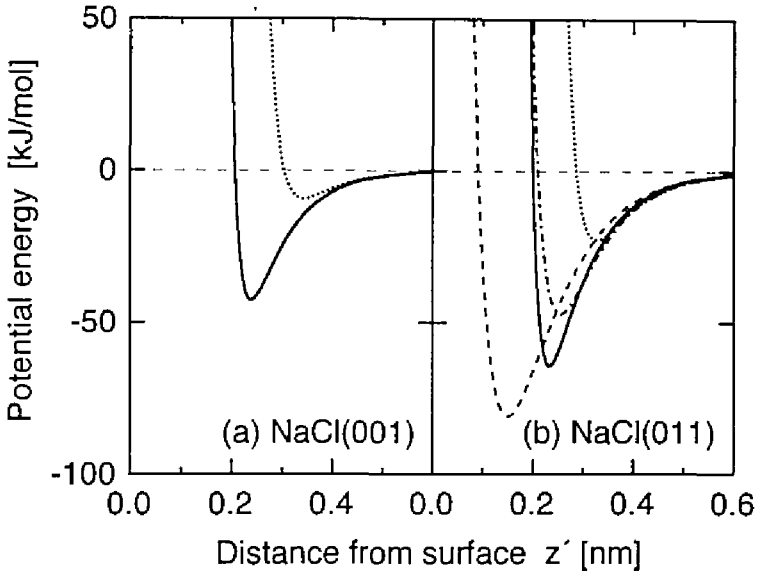

Figure 3.1. Interaction energy between an H_2O and an NaCl surface, as a function of the perpendicular distance from the surface z'. The profiles are calculated for the H_2O which is located at different lateral positions and oriented to various directions: above an Na^+ (solid lines) and above a midpoint of two nearest-neighboring Na^+'s (dashed line), pointing the dipole away from the surface, and above a Cl^- (dotted lines) and above a midpoint of two nearest-neighboring Cl^-'s (dashed–dotted line), pointing the dipole toward the surface (see Figure 3.11). (a) NaCl(001); (b) NaCl(011).

TABLE 3.3: Conditions of MD simulations of 216 water molecules confined between NaCl(001) or NaCl(011) surfaces

		Water/NaCl(001)	Water/NaCl(011)
Box length	L_x/nm	1.692	1.595
	L_y/nm	1.692	1.692
	L_z/nm	5.641	7.180
Location of outermost ions	z/nm	±1.26	±1.28
Cutoff distance	R^{cut}/nm	0.746	0.698
One-time step	Δt/fs	1	1
Average temperature	T/K	298	298

kJ/mol (compare Figures 2.3 and 3.1).

3.2.3 Basic cell

Figure 3.2 illustrates a rectangular cell composed of an aqueous lamina and an NaCl slab, where the periodic boundary conditions are applied in the three dimensions. The origin of coordinates is taken at the center of the aqueous lamina and the xy plane is taken to be parallel to the NaCl surface. Note that two separate slabs appear in Figure 3.2, but actually they are joined each other at $z = \pm L_z/2$ to form one slab because of the z-directional periodicity. The aqueous region contains 216 water molecules. The crystal slab is composed of either 12 lattice planes of 6 × 6 ions for NaCl(001), as shown in Figure 3.3(a), or 24 lattice planes of 4 × 6 ions for NaCl (011), as in Figure 3.3(b). It is confirmed by allowing the ions to move freely that both the crystal slabs are of stable thickness to keep their structural and dynamical properties solidlike in vacuum at 298 K. The slab lengths L_x and L_y are chosen such that the lattice constant of an NaCl crystal is equal to the literature value, 0.5641 nm [The Chemical Society of Japan, 1993]. The Na^+'s and Cl^-'s in the outermost layer of NaCl crystals are located at the place z given in Table 3.3 to satisfy the condition that the density of water at the central region is 1

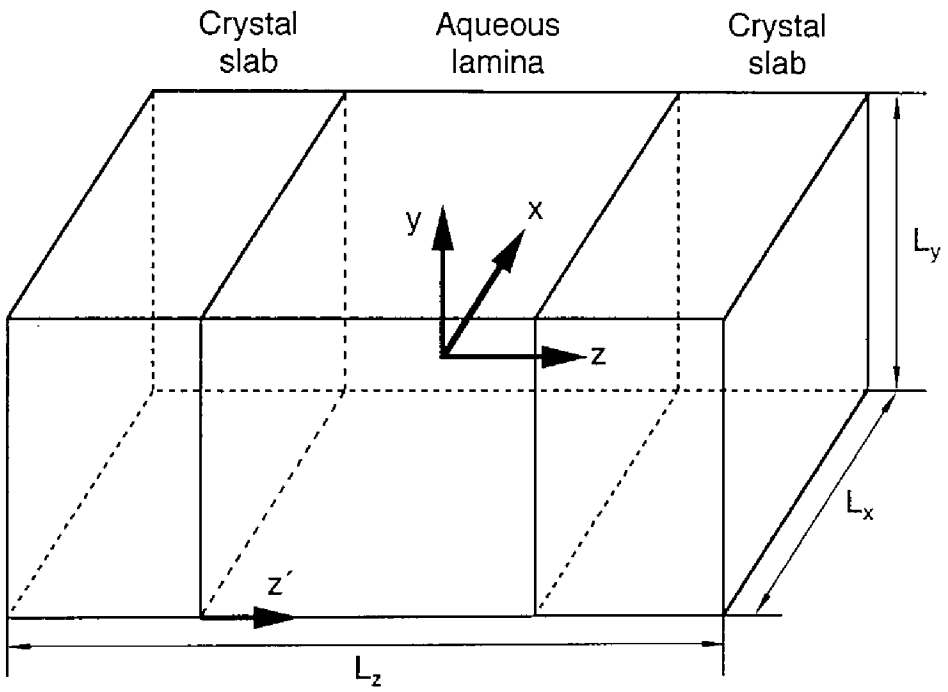

Figure 3.2. Basic cell for MD simulations. Shaded regions represent the NaCl crystal and the rest is water. The origin of coordinates is the center of the cell.

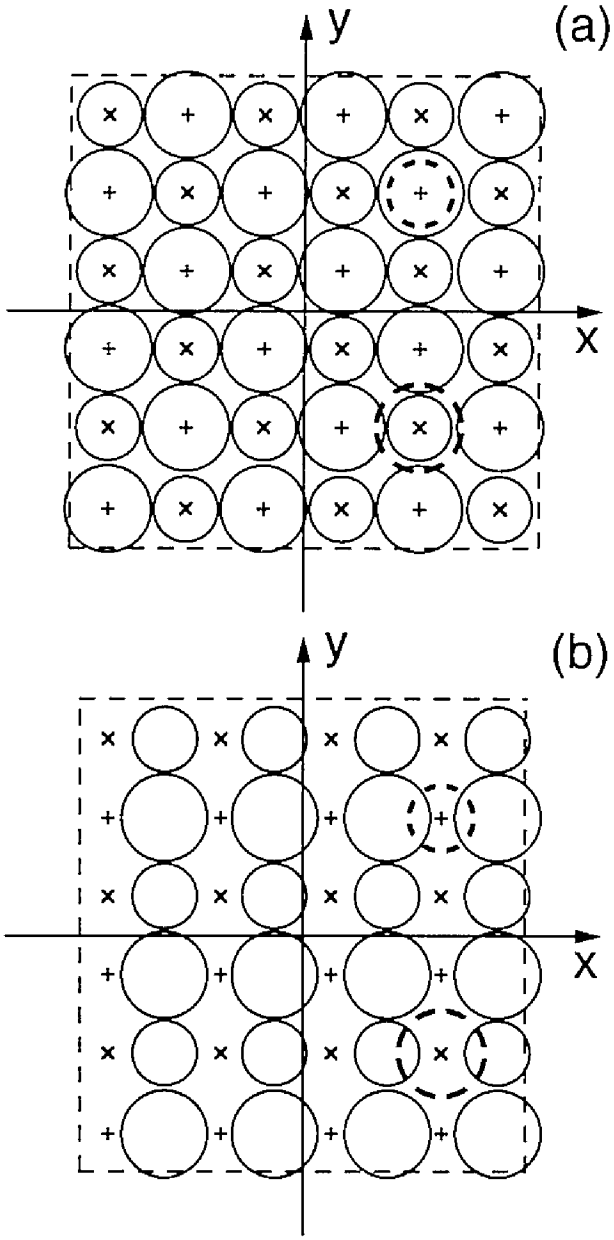

Figure 3.3. Arrangement of ions in an NaCl crystal surface. Small and large circles indicate Na^+ and Cl^- in the first layer from the interface, respectively; and symbols, + and ×, represent centers of Na^+ and Cl^- in the second layer, respectively. Dashed small and large circles denote adsorption sites for Na^+ and Cl^- ions, respectively, which are referred in Chapter 4. Dashed lines are periodic boundaries of the basic cell. (a) NaCl(001); (b) NaCl(011).

g/cm^3. The dimensions of the simulation box are summarized in Table 3.3.

3.2.4 Simulation details

The simulations are performed using the same program as in Section 2.3.4, except that the 3D-Ewald method is employed to handle the long-range Coulomb interactions. The time step used is 1 fs in this chapter.

The simulation procedure is as follows. After water of density 1 g/cm^3 and an NaCl-crystal slab are equilibrated at 298 K separately, they are put together. Then the ions in the crystal are fixed at the equilibrated positions and water molecules are allowed to re-equilibrate for 15–20 ps. Two types of simulations are implemented:

(I) When the stability of the NaCl surface in water is examined, all the ions are allowed to move for another 10 ps with the initial velocity corresponding to translational motions at 298 K. The average temperature is kept at 298 K by velocity scaling to compensate the temperature change due to the nonequilibrium processes such as the dissolution of ions.

(II) When the structure and dynamics of water near the NaCl surface are examined, the ions in the NaCl crystal are fixed and the simulation of water molecules is carried out for 15 ps without any scaling. The average temperature is found to be 298 K.

3.3 Results and discussion

3.3.1 Stability of NaCl surfaces

The NaCl(001) and NaCl(011) surfaces are confirmed to be stable in vacuum as described in Section 3.2.3, but this does not necessarily guarantee that they are

stable in water. Here the stability of the NaCl surfaces exposed to water is examined by the simulations of Type I. It is found that no ion dissolves from both NaCl(001) and NaCl(011) surfaces into water during 10 ps. The outermost ions fluctuate actively around their average positions of NaCl(001) and NaCl(011) and no significant difference in fluctuation is observed between these surfaces. This indicates that the NaCl(001) and NaCl(011) faces in water at 298 K are stable at least within the simulation period of 10 ps, which is in good coincidence with the results predicted by Ohtaki and co-workers [1988; Ohtaki and Fukushima, 1989]. Hence, it is plausible to assume that all the ions in the NaCl crystals are located stably at the time-averaged positions in the simulations of Type II.

In following Sections 3.3.2 to 3.3.6, the structure and dynamics of water adjacent to the NaCl(001) and NaCl(011) surfaces are investigated by the simulations of Type II. These properties are discussed in terms of (i) density profiles of water molecules, (ii) scatter plots of molecular positions on the surface, (iii) numbers of hydrogen bonds and nearest neighbors, (iv) distributions of molecular orientations, and (v) self-diffusion coefficients, using the averaged values at $\pm z$ except for the scatter plots.

3.3.2 Density profiles of water molecules

Figure 3.4 shows the density profiles of O and H atoms. Note that the profile of O atoms represents that for water molecules. The O profiles have sharp peaks next to the NaCl(001) and NaCl(011) surfaces, reflecting that many water molecules are attracted to the surfaces and form adsorbed layers. It is known that this tendency is characteristic at the interface between water and a hydrophilic surface, whereas a hydrophobic surface tends to repel water toward the bulk, as explained in Section 2.4.1. Comparison between the profiles in Figures 3.4(a) and (b) suggests that the structure of water close to NaCl(001) and NaCl(011) is different from each other.

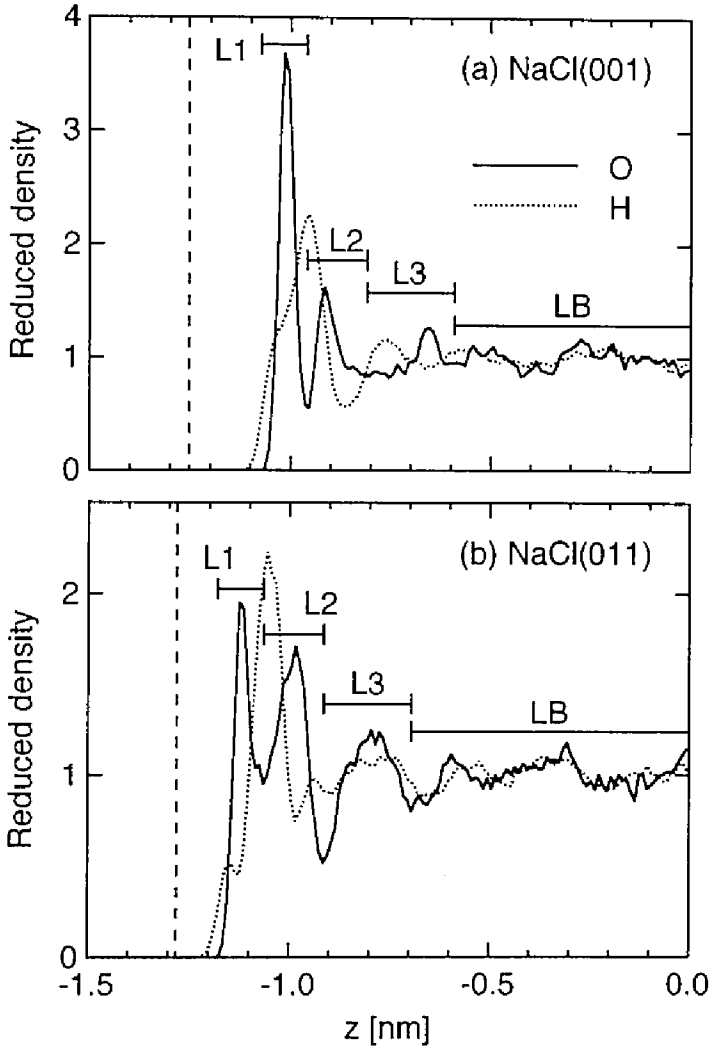

Figure 3.4. Density profiles of O and H atoms of water molecules near the NaCl crystal surface. Solid and dotted lines indicate O and H profiles, respectively. The vertical dashed line denotes the center of outermost ions in the NaCl crystal, as given in Table 3.3. (a) NaCl(001); (b) NaCl(011).

TABLE 3.4: Location of adsorbed layers parallel to the xy plane (L1, L2, L3, and LB), the average number of water molecules in layer α, $n_{water}(\alpha)$, and the number of typical adsorption sites for water molecules in layer α, $n_{site}(\alpha)$

		Water/NaCl(001)	Water/NaCl(011)
Range of $\|z\|$/nm	L1	0.96–1.07	1.07–1.18
	L2	0.81–0.96	0.92–1.07
	L3	0.60–0.81	0.70–0.92
	LB	0.00–0.60	0.00–0.70
$n_{water}(1)/n_{site}(1)$		17.7/18	10.8/12
$n_{water}(2)/n_{site}(2)$		15.3/18	16.0/12

The number of sharp peaks in the O profile indicates that at least two adsorbed layers of water molecules are formed near the NaCl(001) surface, while at least three layers are formed near the NaCl(011) surface. Since the second peak of the O profile in Figure 3.4(b) has a shoulder at $|z| = 1.02$ nm near the peak at $|z| = 0.99$ nm, the second layer is considered to be the "bilayer" composed of water molecules adsorbed on different relative positions of the surface.

To analyze further the layers, the water lamina is divided into three adsorbed layers of water molecules (L1, L2, and L3) and the bulklike region (LB), as shown in Figure 3.4 and Table 3.4. The minimum distance between L1 and the outermost plane of a crystal is 0.19 nm for NaCl(001) and 0.10 nm for NaCl(011), which indicates that a water molecule can approach the NaCl(011) surface about 0.1 nm closer than the NaCl(001) surface. This is probably due to the following reasons: (i) the NaCl(011) is rougher in surface than the NaCl(001), as shown in Figure 3.3; and (ii) a water molecule interacts with the NaCl(011) more strongly than the NaCl(001), as shown in Figure 3.1.

Average numbers of water molecules in L1 and L2 are calculated by integrating the O density profile and listed in Table 3.4 as well as the number of typical adsorption sites for water molecules in each layer (see Figure 3.5). In the case of NaCl(001), the adsorption sites for L1 are occupied completely by water

molecules and those for L2 are 85 % occupied. In the case of NaCl(011), the adsorption sites for L1 are 90 % covered, but those for L2 are fully covered. This will explain the presence of the bilayer described above.

3.3.3 Scatter plots of molecular positions on the surface

Scatter plots of positions of all the O atoms in the first three layers are displayed in Figure 3.5. Here the black-looking region means the probable location of water molecules on the surface. Figure 3.5 shows that the adsorption sites of water molecules on the NaCl(001) and NaCl(011) surfaces are different. In the case of NaCl(001), water molecules in L1 are adsorbed above an Na^+ and those in L2 are adsorbed above a Cl^-. In the case of NaCl(011), water molecules in L1 are adsorbed above a midpoint of the two nearest-neighboring Na^+'s and those in L2 are adsorbed mainly above a midpoint of the two nearest-neighboring Cl^-'s. As shown in Figure 3.5(b-ii), water molecules in L2 are adsorbed above an Na^+ of NaCl(011), which corresponds to the presence of the shoulder in the second peak of the O profile shown in Figure 3.4(b). This result implies that the outermost Na^+'s of NaCl(011) are masked by water molecules partly in L2 as well as in L1.

Thus, the adsorption sites of water molecules in L1 and L2 are different in the NaCl(001) and NaCl(011) surfaces. In both cases, water molecules in L1 are adsorbed on the Na^+'s somewhat more strongly than those in L2 are adsorbed on the Cl^-'s, as expected from Figure 3.1. However, water molecules in L3 behave more fluidlike apparently because of having no particular adsorption site on the surface, as illustrated in Figures 3.5(a-iii) and (b-iii).

3.3.4 Local coordination and hydrogen bonding

Figure 3.6 shows the average numbers of nearest neighbors n_{NN} and hydrogen bonds n_{HB} per water molecule as a function of z, whose definitions are the same as

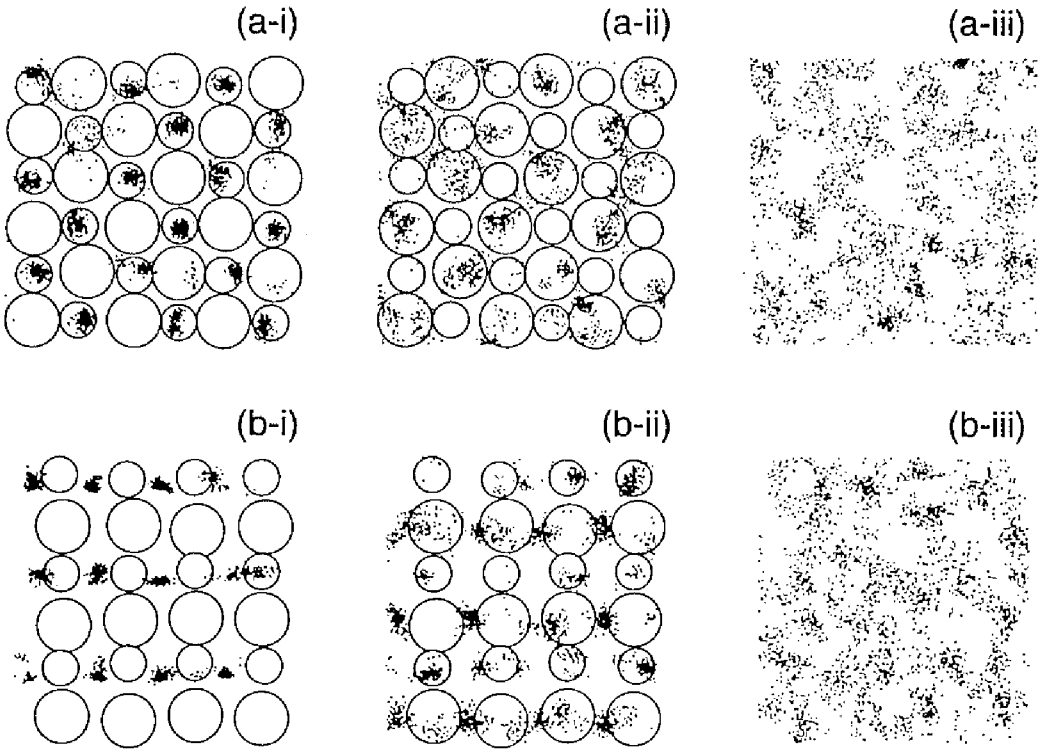

Figure 3.5. Scatter plots of positions of all the O atoms of water molecules in the different layers near the NaCl surface. Positions of O atoms (x, y) are marked by dots every 0.1 ps for 15 ps. Parts a and b in #1 in panel (#1-#2) indicate plots for surfaces of NaCl(001) and NaCl(011), respectively; and parts i, ii, and iii in #2 represent plots for adsorbed layers of L1, L2, and L3, respectively, which are defined as in Figure 3.4 and Table 3.4. Outermost Na^+'s and Cl^-'s of the NaCl crystal are depicted by small and large circles, respectively, but they are not shown in panels (a-iii) and (b-iii) because water molecules in L3 have no particular adsorption site.

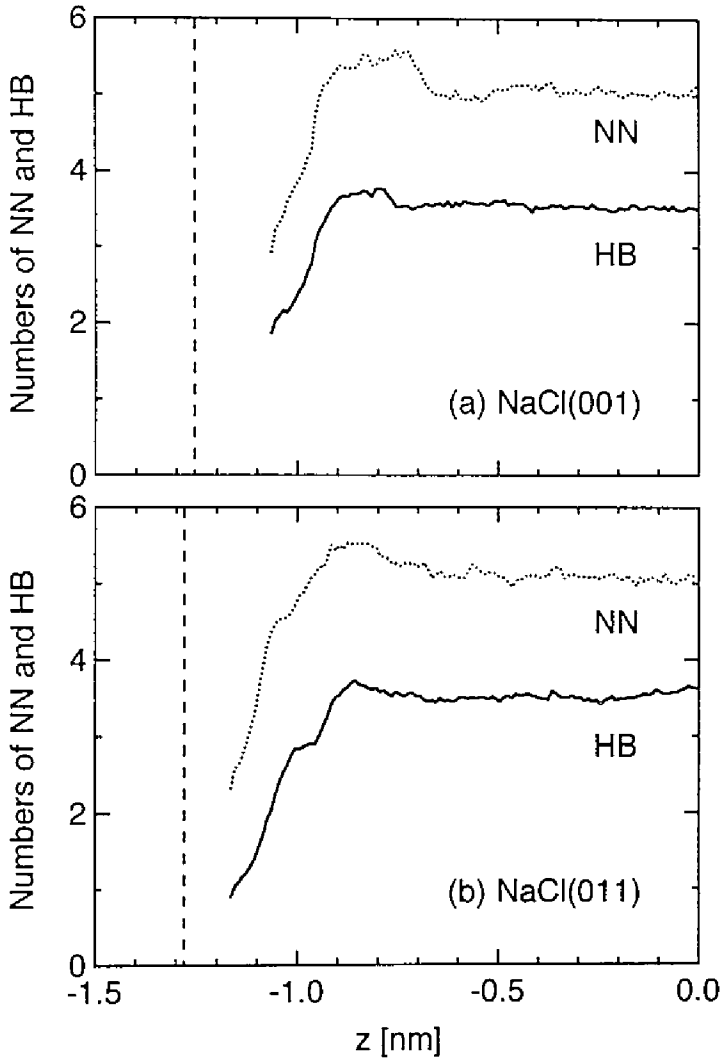

Figure 3.6. Average numbers of nearest neighbors n_{NN} and hydrogen bonds n_{HB} per water molecule. Solid and dotted lines indicate the values of n_{HB} and n_{NN}, respectively. The vertical dashed line denotes the center of outermost ions in the NaCl crystal, as given in Table 3.3. (a) NaCl(001); (b) NaCl(011).

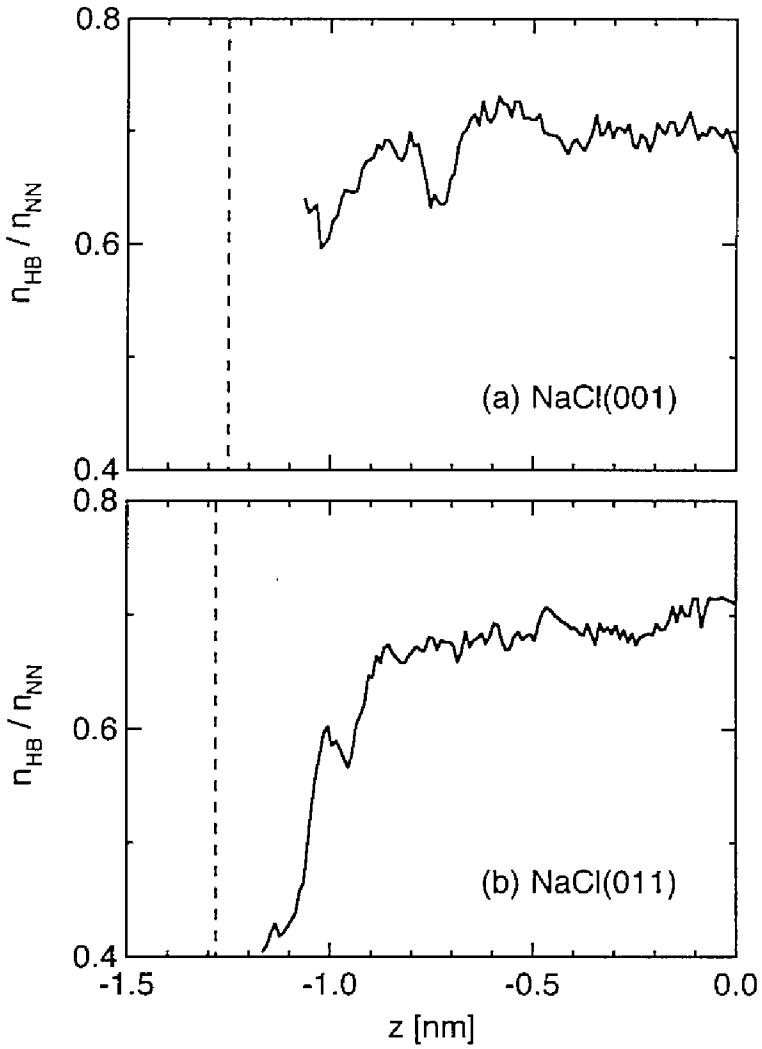

Figure 3.7. Value of n_{HB}/n_{NN} obtained from Figure 3.6, which is a parameter to estimate the fraction of hydrogen bonds out of the nearest-neighboring water molecules. The vertical dashed line denotes the center of outermost ions in the NaCl crystal, as given in Table 3.3. (a) NaCl(001); (b) NaCl(011).

in Section 2.4.2. The values of n_{NN} and n_{HB} in the range of $|z| < 0.5$ nm are almost constant at about 5.0 and 3.5, respectively, which coincide with those given by the separate simulation of the bulk water. These values increase slightly in the range of $|z| = 0.7$–0.9 nm. This increase is attributable to the dense layers of water molecules near the surface, as shown in Figure 3.4. However, the value of n_{HB} is reduced remarkably closer to the interface, which coincides well with the reduction of the value of n_{NN}. This behavior is similar to that of water near the surfaces of SiO_2, lecithin [Kjellander and Marcelja, 1985b], and fully hydroxylated silica [Lee and Rossky, 1994]. It seems that this behavior is characteristic of water close to a hydrophilic surface, although there exists some ambiguity because the value of n_{HB} is reduced only slightly in the case of the Pt(100) surface [Spohr, 1989]. The average number of hydrogen bonds broken by the crystal surface is 1.6 for NaCl(001) and 2.6 for NaCl(011), which are calculated by n_{HB} shown in Figure 3.6. These values are larger than 1.0 for the hydrocarbon surface given in Section 2.4.3.

The value n_{HB}/n_{NN} is calculated as shown in Figure 3.7. It exhibits clearly that the hydrogen-bonding network is disrupted remarkably at the NaCl(011) interface, while the network is destroyed at the NaCl(001) interface much less than expected from the significant decrease of n_{HB} shown in Figure 3.6(a). This is because the interaction of an H_2O with NaCl(011) is much stronger than the hydrogen bond between two H_2O's, while that with NaCl(001) is as strong as the hydrogen bond. On the other hand, n_{HB}/n_{NN} increases significantly at the hydrophobic surface although n_{HB} is reduced, as described in Section 2.4.2.

3.3.5 Orientational structure

Definition of orientational parameters. The results presented above exhibit that the structure of water near the NaCl surface is influenced greatly by the

features of the surface. Here the orientational structure of water molecules is investigated in terms of the distributions of angels θ_μ, θ_{OH}, and ϕ_{HH}, which are defined in Figure 3.8 schematically. The definitions of θ_μ and θ_{OH} are the same as in Section 2.4.3. ϕ_{HH} is defined as the angle between the projection of the HH vector on the xy plane and the x axis. One- and two-dimensional distributions of these angles of water molecules in L1 and L2 are evaluated. The probability distributions of $P_\mu(\cos\theta_\mu)$ and $P_{OH}(\cos\theta_{OH})$ are shown in Figure 3.9. The distributions of $P_{\mu,HH}(\cos\theta_\mu, \phi_{HH})$ are shown in Figure 3.10, which are averaged by considering the symmetric feature of the surfaces, C_{4v} for NaCl(001) and C_{2v} for NaCl(011). The favorable configurations of water molecules near the surface are determined from these distributions as illustrated in Figure 3.11, whose procedure is described below.

Orientational distributions. Figure 3.9 suggests that the molecular orientations near the NaCl(001) are different from those near the NaCl(011), as expected from the difference in the density profile and in the adsorption site of water molecules near the surfaces. The distributions of P_μ and P_{OH} for NaCl(011) have sharper peaks than those for NaCl(001). This is explained by the strong interaction between an H_2O and the NaCl(011) surface (compare Figures 3.1(a) and (b)).

NaCl(011) surface. Figure 3.9(b-i) shows that P_μ has two maxima at $\cos\theta_\mu$ = 1.0 and 0.6. This indicates that L1 is made of two types of "flip-up" molecules illustrated in Figures 3.11(b-i) and (b-ii). Here "flip-up" and "flop-down" denote the molecule pointing the dipole away from and toward the surface, respectively.

The flip-up molecule with $\cos\theta_\mu$ = 1.0 (i.e., θ_μ = 0°) has the two OH bonds 55° from $\mathbf{n}_z$ as in Figure 3.11(b-i), because of the internal geometry of an SPC/E water molecule (see Figure 2.2). This coincides with the peak of P_{OH} at $\cos\theta_{OH}$ = 0.6 shown in Figure 3.9(b-i). The molecule tends to orient the HH vector parallel

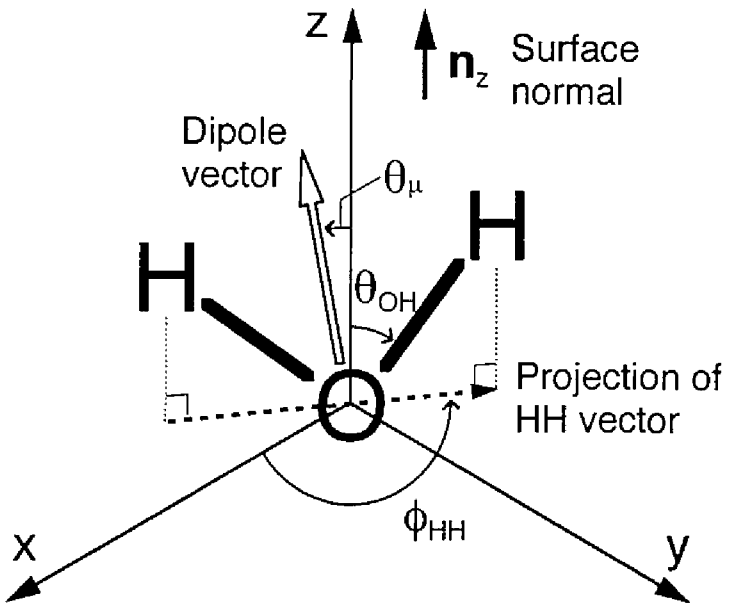

Figure 3.8. Schematic definition of angles θ_μ, θ_{OH}, and ϕ_{HH}, which determine the orientation of a water molecule on the NaCl crystal surface.

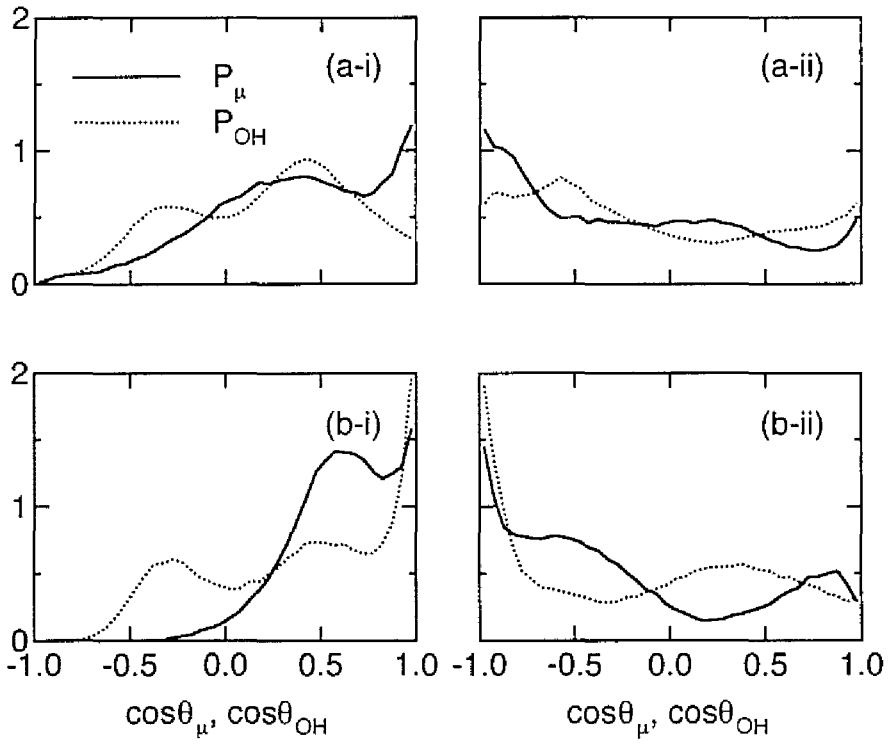

Figure 3.9. Orientational distributions $P_{\mu}(\cos\theta_{\mu})$ and $P_{OH}(\cos\theta_{OH})$ of water molecules in the different layers on the NaCl surface. Angles θ_{μ} and θ_{OH} are defined as in Figure 3.8. Solid and dotted lines indicate distributions of P_{μ} and P_{OH}, respectively. Parts a and b in #1 in panel (#1-#2) indicate distributions for surfaces of NaCl(001) and NaCl(011), respectively; and parts i and ii in #2 represent distributions for adsorbed layers of L1 and L2, respectively, which are defined as in Figure 3.4 and Table 3.4.

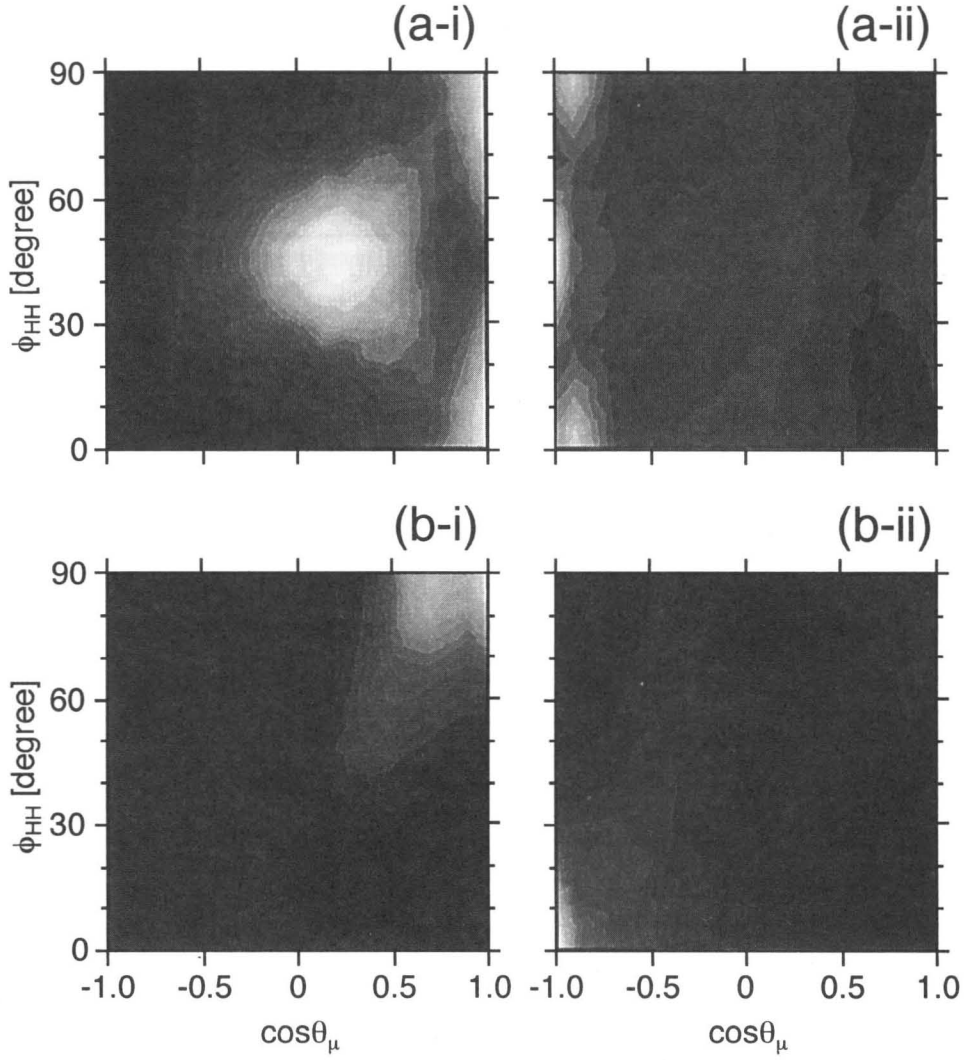

Figure 3.10. Two-dimensional orientational distributions, $P_{\mu,HH}(\cos\theta_\mu, \phi_{HH})$, of water molecules in the different layers on the NaCl surface. Angles θ_μ and ϕ_{HH} is defined as in Figure 3.8. The lighter-looking region means the more probable orientation, where the gray levels in four panels are arbitrary. Parts a and b in #1 in panel (#1-#2) indicate distributions for surfaces of NaCl(001) and NaCl(011), respectively; and parts i and ii in #2 represent distributions for adsorbed layers of L1 and L2, respectively, which are defined as in Figure 3.4 and Table 3.4. Each distribution is averaged by considering the symmetric feature of the surfaces, C_{4v} for NaCl(001) and C_{2v} for NaCl(011).

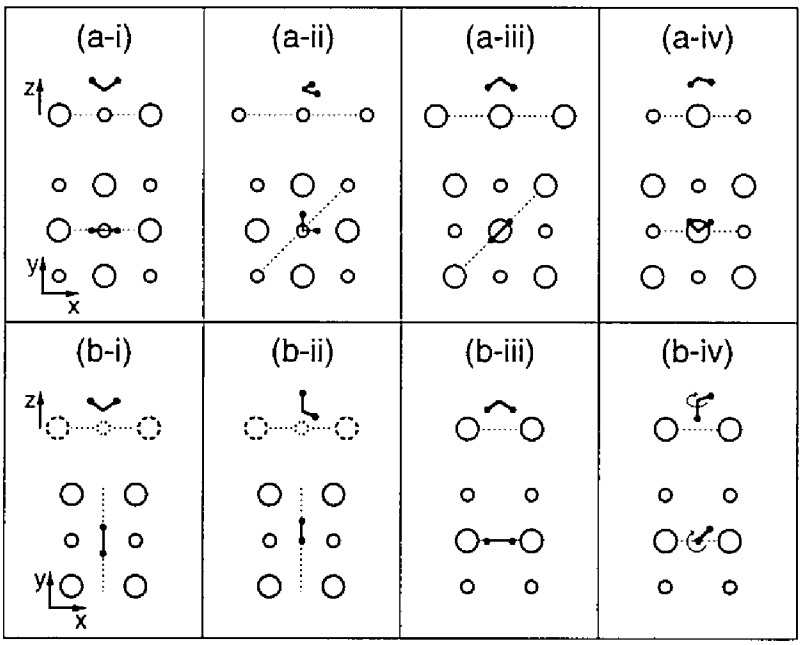

Figure 3.11. Favorable configurations of water molecules in the different layers on the surface. (a-i, a-ii) L1 on NaCl(001); (a-iii, a-iv) L2 on NaCl(001); (b-i, b-ii) L1 on NaCl(011); (b-iii, b-iv) L2 on NaCl(011). In each panel, the bottom picture represents the projection of a water molecule on the *xy* plane. The top picture represents the projection of the water molecule on the plane that is perpendicular to the *xy* plane and is crossing through the dashed line drawn in the bottom picture.

to the y axis, as shown in Figure 3.11(b-i). This is because $P_{\mu,\mathrm{HH}}$ has a maximum at $(\cos\theta_\mu, \phi_{\mathrm{HH}}) = (1.0, 90°)$, as in Figure 3.10(b-i).

The other flip-up molecule with $\cos\theta_\mu = 0.60$ (i.e., $\theta_\mu = 55°$) has the two OH bonds 0° and 110° from $\mathbf{n}_z$, as shown in Figure 3.11(b-ii), because P_{OH} has two peaks at $\cos\theta_{\mathrm{OH}} = 1.0$ and –0.3. The molecule tends to orient the projection of the HH vector parallel to the y axis, which is explained by the maximum of $P_{\mu,\mathrm{HH}}$ at $(\cos\theta_\mu, \phi_{\mathrm{HH}}) = (0.60, 90°)$.

When Figure 3.9(b-i) is reversed with respect to $\cos\theta_\mu = \cos\theta_{\mathrm{OH}} = 0$, it becomes qualitatively similar to Figure 3.9(b-ii). This indicates that water molecules in L2 favor two flop-down configurations shown in Figures 3.11(b-iii) and (b-iv), which are the inverted configurations of Figures 3.11(b-i) and (b-ii) with respect to the surface plane, respectively. As shown in Figure 3.11(b-iii), the flop-down molecule with $\cos\theta_\mu = -1.0$ orients the HH vector parallel to the x axis, because $P_{\mu,\mathrm{HH}}$ is maximal at $(\cos\theta_\mu, \phi_{\mathrm{HH}}) = (-1.0, 0°)$ as in Figure 3.10(b-ii). For the other flop-down molecule with $\cos\theta_\mu = -0.6$, $P_{\mu,\mathrm{HH}}$ around $\cos\theta_\mu = -0.6$ does not depend particularly on ϕ_{HH}. This suggests that this water molecule points toward the surface with one OH bond, around which the other OH bond can rotate freely, as illustrated in Figure 3.11(b-iv). It is worth noting that P_μ in Figure 3.9(b-ii) and $P_{\mu,\mathrm{HH}}$ in Figure 3.10(b-ii) have a minor peak around $\cos\theta_\mu = 0.85$, which coincides with the observation that water molecules in L2 near NaCl(011) are adsorbed above Na^+'s, as shown in Figure 3.5(b-ii).

NaCl(001) surface. Figures 3.10(a-i) and (a-ii) show that $P_{\mu,\mathrm{HH}}$ has a maximum at $(\cos\theta_\mu, \phi_{\mathrm{HH}}) = (1.0, 0°)$ (and $(1.0, 90°)$) for L1 and at $(\cos\theta_\mu, \phi_{\mathrm{HH}}) = (-1.0, 45°)$ for L2. Considering the molecular geometry, this maximum corresponds to the peak of P_{OH} at $\cos\theta_{\mathrm{OH}} = 0.6$ for L1 and at $\cos\theta_{\mathrm{OH}} = -0.6$ for L2 shown in Figures 3.9(a-i) and (a-ii), respectively. From these results, the favorable configurations for L1 and L2 are depicted in Figures 3.11(a-i) and (a-

iii), respectively. Note that the complete flip-up and flop-down molecules, whose dipoles are parallel to $\mathbf{n}_z$, are observed near the NaCl(011) surface also, apart from differences in the adsorption position and in the HH vector orientation.

The other maximum of $P_{\mu,\mathrm{HH}}$ is located at $(\cos\theta_\mu,\ \phi_{\mathrm{HH}}) = (0.25,\ 45°)$ for L1 and at $(\cos\theta_\mu,\ \phi_{\mathrm{HH}}) = (-0.80,\ 0°)$ (and $(-0.80,\ 90°)$) for L2. For the flip-up molecule in L1, P_{OH} has peaks at $\cos\theta_{\mathrm{OH}} = 0.4$ and -0.3. This indicates that one of the two H atoms is pointing away from the surface (i.e., $\cos\theta_{\mathrm{OH}} = 0.4$) and the other is pointing toward the surface (i.e., $\cos\theta_{\mathrm{OH}} = -0.3$), as illustrated in Figure 3.11(a-ii). For the flop-down molecule in L2, P_{OH} has no sharp peak. However, it is concluded from the location of the maximum of $P_{\mu,\mathrm{HH}}$ that two H atoms are pointing toward the surface, one of which is closer to the surface than the other, as illustrated in Figure 3.11(a-iv). Note that these two configurations shown in Figures 3.11(a-ii) and (a-iv) are not dominant in the vicinity of the NaCl(011) surface.

Influence of molecular orientations on hydrogen bonds. Hydrogen bonding is possible between the water molecules with such configurations as shown in Figures 3.11(a-i)–(a-iv), for example, between the molecules shown in Figures 3.11(a-ii) and (a-iv). However, hydrogen bonding between the water molecules in Figures 3.11(b-i)–(b-iv) is apparently impossible. These results will explain the observation that the hydrogen-bonding network is disrupted near the NaCl(011) surface much more than near the NaCl(001) surface, as shown in Figure 3.7.

3.3.6 Diffusion

The motion of water molecules in the first three layers is illustrated in Figure 3.5 previously. Here the motion is investigated quantitatively in terms of the self-diffusion coefficients of water molecules in L1, L2, L3, and LB. The diffusion

TABLE 3.5: Diffusion coefficients of water molecules in the different layers near the NaCl surfaces (in 10^{-5} cm^2/s).

	Water/NaCl(001)				Water/NaCl(011)			
Layer[a]	L1	L2	L3	LB	L1	L2	L3	LB
D_x	0.13	0.34	1.51	3.06	<0.01	0.66	1.95	3.53
D_y	0.12	0.37	1.73	2.51	0.03	0.30	0.94	2.84
D_{xy}	0.13	0.35	1.62	2.79	0.01	0.48	1.44	3.18
D_z	<0.01	0.04	0.20	1.79	<0.01	0.04	0.24	2.50

[a] L1, L2, L3, and LB are defined as in Figure 3.4 and Table 3.4.

coefficients are calculated by the mean square displacement using Equation (2.16), as summarized in Table 3.5.

Anisotropic diffusivity. The diffusion coefficients in L1, L2, and L3 are reduced significantly compared with that of the bulk water, 2.5×10^{-5} cm^2/s, and anisotropic because of $D_x \approx D_y > D_z$. The diffusivity of water molecules decreases as they approach the surface. Especially, water in L1 and L2 on the surface is "solidlike" since the diffusion coefficients are much smaller than that of the fluid water.

As far as the lateral diffusion coefficient D_{xy} is concerned, water in L1 on the NaCl(011) is more solidlike than that on the NaCl(001), as expected from the difference in the binding energy of a water molecule on these surfaces. On the other hand, water in L2 on the NaCl(011) is less solidlike than that on the NaCl(001), although the binding energy is larger in absolute value for NaCl(011) than for NaCl(001). This result can not be explained by the binding energy, but by the fact that the hydrogen-bonding network near the NaCl(011) surface is disrupted more significantly than that near the NaCl(001), as shown in Figure 3.7. Thus the binding energy and the hydrogen-bonding energy must be taken into account simultaneously to explain the diffusivity of water molecules near the surface.

Influence of interfacial structures on molecular diffusivity. D_x and D_y in the first three layers are isotropic in the case of NaCl(001) because of the surface symmetry C_{4v}, while these coefficients are anisotropic in the case of NaCl(011) because of the surface symmetry C_{2v}. At the water/NaCl(011) interface, D_x in L1 is negligibly small because the favorable configurations of water molecules in L1 on NaCl(011) do not allow themselves to diffuse along the x axis, as shown in Figures 3.11(b-i) and (b-ii). D_y in L2 is smaller than D_x because the y-directed diffusion of water molecules in L2 is obstructed by the favorable configuration shown in Figure 3.11(b-iii) and the "ridge" structure along the x axis of adsorbed water molecules in L1 shown in Figure 3.5(b-i). The similar anisotropy of the diffusion is observed also for molecules in L3. These results indicate that the molecular diffusion near the surface is very sensitive to the nature of the surface.

It is also found that the diffusion coefficients are anisotropic even in LB near the NaCl(001) and NaCl(011) surfaces. This indicates that water in LB does not display the same dynamical properties as the bulk water, although it has the same static properties as the bulk water, such as the density in Figure 3.4 and the hydrogen-bonding network in Figure 3.6.

3.4 Concluding remarks

MD simulations of water/NaCl(001) and water/NaCl(011) interfaces are carried out and the following conclusions are drawn.

(i) Both the (001) and (011) faces of an NaCl crystal without any lattice defect are stable in water at 298 K, at least within the period of 10 ps.

(ii) Water molecules in L1 and L2 near the NaCl(001) and NaCl(011) surfaces

reduce their diffusivity and are regarded as "solidlike."

(iii) A slight difference in the feature between NaCl(001) and NaCl(011) surfaces causes a significant change in the water–surface interaction, the number and structure of adsorbed layers, the adsorption point of water molecules, the perturbation of the hydrogen-bonding network, and the molecular diffusion near the surface.

(iv) Water molecules in LB can be regarded as bulk with respect to the static properties, but the dynamic behavior is still influenced by the existence of the crystal surface.

Investigations in Chapters 2 and 3 elucidate the basic features of water at hydrophobic and hydrophilic surfaces. These information is very useful in simplifying molecular models, by which simulations of the larger and more complex systems become possible, as is described in Chapter 5.

Part II

Adsorption of Ions and Surfactants onto Liquid/Solid Interfaces

4
Ion Adsorption onto Water/NaCl Crystal Interfaces

4.1 Introduction

The behavior of water molecules near the NaCl-crystal surface was examined in Chapter 3. Succeedingly, the attention is focused on the behavior of solute ions, Na^+ and Cl^-, approaching the NaCl surface in water. This ionic behavior at the interface is fundamentally important in understanding not only the crystal growth but also many industrial processes such as the dispersion of colloidal particles, the membrane separation, and the electrode reactions.

In this chapter, free energy profiles for Na^+ and Cl^- adsorption onto the NaCl(001) and NaCl(011) surfaces in water are evaluated using MD simulations. Discussion yields how stably the ions adsorb on the surface and how the adsorption is affected by the ionic size and the surface structure. The similar simulation procedure is also applicable to evaluate the interaction forces between macroscopic colloidal particles in a fluid, as is described in Chapter 6.

4.2 Methods

All the molecular models, basic cell, and algorithms employed are the same as described in Section 3.2, unless specified. The different point to note is that one solute ion is introduced in water between NaCl-crystal surfaces to evaluate the

solvent-averaged interaction against the surface. The details are described below.

4.2.1 Potential of mean force (PMF)

The following system is considered: 215 water molecules and one solute ion, either Na^+ or Cl^-, are confined between two surfaces of an NaCl crystal. Then, where is the adsorption pathway of the ion onto the water/crystal interface? To describe the pathway, let us use the mean force acting on the ion at position $\mathbf{r}$, $\mathbf{F}^{tot}(\mathbf{r})$, and the potential of mean force (PMF), $W^{tot}(\mathbf{r})$, which are attributable to the surface and solvent contributions. Because the solid surface used has an atomistic structure, W^{tot} depends on the lateral position (x, y) and also on the perpendicular distance from the nearest wall z'. The most probable path will be continuous (global) minimum points of W^{tot} as a function of z', which is written as $\mathbf{r}_{path} = (x_{min}(z'), y_{min}(z'), z')$. Hence, the following relation must be satisfied:

$$\frac{\partial W^{tot}}{\partial x} = \frac{\partial W^{tot}}{\partial x} = 0 \quad \text{at given } z',$$

$$\text{i.e.,} \quad F_x^{tot}(\mathbf{r}_{path}) = F_y^{tot}(\mathbf{r}_{path}) = 0. \tag{4.1}$$

For simplicity, the notation $W^{tot}(z')$ or W^{tot} is used for the PMF on the most probable path and the notation $\mathbf{F}^{tot}(z')$ or $\mathbf{F}^{tot}$ is used for the mean force.

To calculate $W^{tot}(z')$ satisfying Equation (4.1), the SHAKE method [Spohr, 1993] and the umbrella sampling method [Rose and Benjamin, 1991] were employed in MD simulations. These methods are sophisticated and the most reliable, but time-consuming unfortunately.

In this study, $W^{tot}(z')$ is evaluated on a pathway for Na^+ and Cl^- adsorption onto an NaCl surface in vacuum. It is found that the path is the perpendicular line above an "adsorption site" shown in Figure 3.3 (see Section 4.3.1). A series of MD simulations are performed, constraining the ion at discrete points on the path

by assigning the heavy mass [Perera and Berkowitz, 1993]. During each simulation, the total force on the ion at time step τ, $\mathbf{F}^{tot}(\tau)$, is integrated to obtain the mean force:

$$F_{\xi}^{tot} = \langle F_{\xi}^{tot}(\tau) \rangle_{run} = \frac{1}{\tau_{run}} \sum_{\tau=1}^{\tau_{run}} F_{\xi}^{tot}(\tau) \quad (\xi = x, y, z'), \tag{4.2}$$

where τ_{run} is the total simulation step. Supposing that Equation (4.2) satisfies Equation (4.1), the potential $W^{tot}(z')$ can be obtained by integrating $F_{z'}^{tot}$ from the large separation z'_0 to a given separation z':

$$W^{tot}(z') = -\int_{z'_0}^{z'} F_{z'}^{tot}(z')\, dz' . \tag{4.3}$$

In the same way, the ion–surface interaction force and the potential in vacuum, $F_{z'}^{surf}(z')$ and $W^{surf}(z')$ can be obtained. The solvent contributions, $F_{z'}^{solv}(z')$ and $W^{solv}(z')$, are calculated by

$$F_{z'}^{solv}(z') = F_{z'}^{tot}(z') - F_{z'}^{surf}(z'), \tag{4.4}$$

$$W^{solv}(z') = W^{tot}(z') - W^{surf}(z'). \tag{4.5}$$

Note that the PMF obtained here is identical to the free energy profile for ion adsorption in water.

4.2.2 Simulation details

The Na^+'s and Cl^-'s in the NaCl crystal are fixed at their given positions, as mentioned in Sections 3.2.4 and 3.3.1. A series of simulations are performed in the following way:

(i) Starting from the equilibrated water/NaCl crystal system which was calculated in Section 3.2.4, a water molecule near the center of the water lamina is replaced by either Na^+ or Cl^- such that the ion is perpendicularly above the

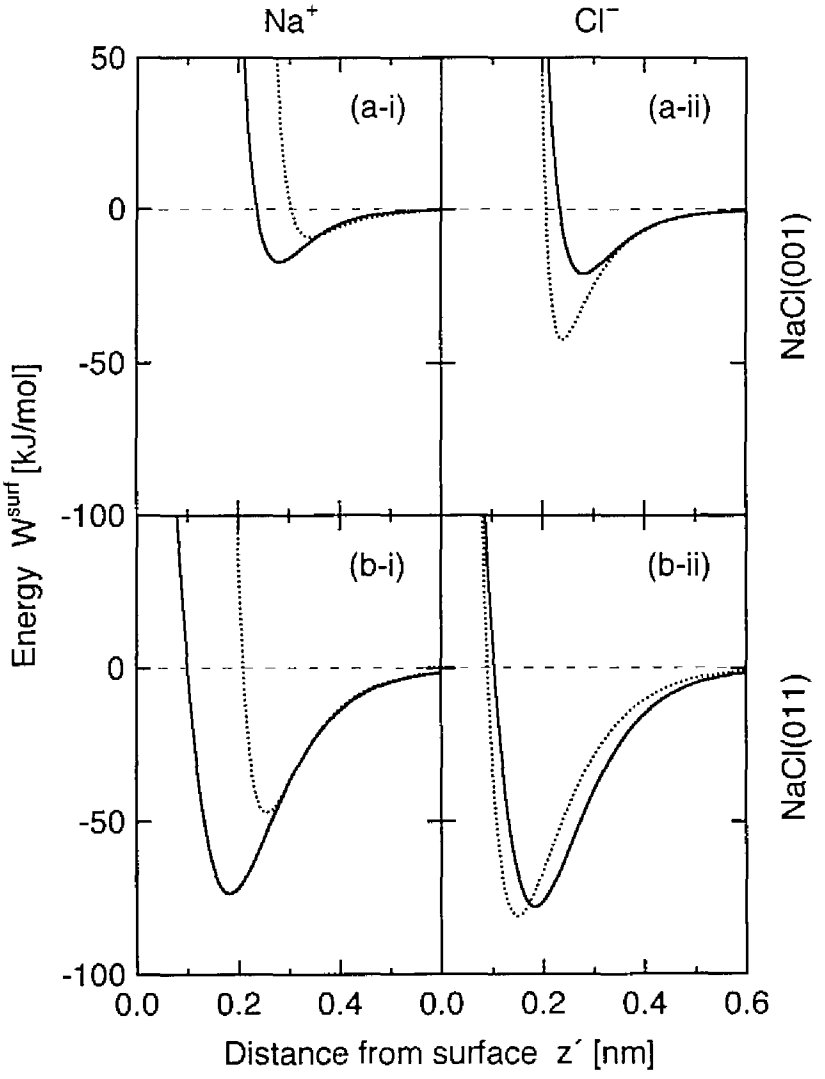

Figure 4.1. Interaction potentials in vacuum, W^{surf}, of Na^+, Cl^-, and H_2O above their adsorption sites on the NaCl crystal surface, which are illustrated in Figure 3.3. In each panel, the solid line represents the ion–surface interaction: (a-i) Na^+–NaCl(001); (b-i) Na^+–NaCl(011); (a-ii) Cl^-–NaCl(001); and (b-ii) Cl^-–NaCl(011). The dotted line represents the interaction of the H_2O above the same adsorption site as that for the ion.

adsorption site shown in Figure 3.3.

(ii) Since the system is disturbed by inserting the ion, it is equilibrated over 16 ps, constraining the ion at the given position.

(iii) The force acting on the ion is integrated for 26 ps to obtain the mean force, using Equation (4.2).

(iv) Then, an external force is assigned to the ion along the $-z'$ direction for 2–4 ps such that it moves to a new position.

(v) In order to equilibrate water molecules around the ion, the system is allowed to evolve for 4 ps with the ion constrained at the new position.

Repeating the procedure from (iii) to (v), one can obtain the force–distance profile. The time step used is 2 fs. The temperature is adjusted to 298 K by velocity scaling at every 200th step. Values of $F_x^{\mathrm{tot}}(z')$ and $F_y^{\mathrm{tot}}(z')$ are confirmed to be nearly zero within the statistical accuracy. The potential $W^{\mathrm{tot}}(z')$ is calculated using Equation (4.3) with the trapezoidal rule, in which no smoothing procedure is employed. A simulation system is usually electroneutral, but the present system is not. In practice, the non-electroneutrality is negligible when the system employed is enough large, as in other studies [Spohr, 1993; Heinzinger, 1996].

4.3 Results and discussion

4.3.1 Ion–surface and water–surface interactions in vacuum

It is found that in vacuum an ion, Na^+ or Cl^-, adsorbs most stably above a counter ion of the NaCl(001) surface and above a midpoint of two nearest-neighboring counter ions of the NaCl(011), as illustrated in Figures 3.3(a) and (b), respectively. These points are referred to as "adsorption sites."

The interaction potentials in vacuum, $W^{\mathrm{surf}}(z')$, of Na^+, Cl^-, and H_2O

perpendicularly above their adsorption sites of NaCl(001) and NaCl(011) surfaces are calculated, as shown in Figure 4.1. Note that the favorable configuration of an H_2O on the adsorption site is determined from Figure 3.11 and the same as in Figure 3.1. Comparison of $W^{surf}(z')$ between Figures 4.1(a-i) and (b-i) and between Figures 4.1(a-ii) and (b-ii) indicates that the NaCl(011) surface interacts with the adsorbates of Na^+, Cl^-, and H_2O more strongly than the NaCl(001). The Na^+ interacts with the NaCl surface more strongly than the H_2O and its stable point is closer to the surface than that of the H_2O, in both the cases of NaCl(001) and NaCl(011). On the other hand, the Cl^- interacts with the surfaces less strongly than the H_2O and its stable point is further apart from the surfaces than that of the H_2O. The author emphasizes that the characteristics of water adsorption influence significantly the free energy profile for ion adsorption, as described below.

4.3.2 Ion–surface interactions in water

The mean force on Na^+ and Cl^- ions in water, $F_{z'}^{tot}$, is calculated as shown in Figures 4.2 and 4.3, respectively, in which the surface and solvent contributions, $F_{z'}^{surf}$ and $F_{z'}^{solv}$, are also given. Here the positive and negative values indicate the repulsive and attractive forces, respectively. The error in the time-averaged value of $\langle F_{z'}^{tot}(\tau)\rangle_{run}$ by Equation (4.2), $\sigma(\langle F_{z'}^{tot}(\tau)\rangle_{run})$, is estimated by the following equation [Allen and Tildesley, 1987]:

$$\sigma^2\left(\langle F_{z'}^{tot}(\tau)\rangle_{run}\right) = 2\tau_F \cdot \sigma^2\left(F_{z'}^{tot}(\tau)\right) / \tau_{run}, \tag{4.6}$$

where

$$\sigma^2\left(F_{z'}^{tot}(\tau)\right) = \frac{1}{\tau_{run}} \sum_{\tau=1}^{\tau_{run}} \left[F_{z'}^{tot}(\tau) - \langle F_{z'}^{tot}(\tau)\rangle_{run}\right]^2. \tag{4.7}$$

Here τ_F is the time step of the force correlation. It is found that the statistical errors of $F_{z'}^{tot}$ are almost within ±30 kJ/(mol·nm), which is sufficiently smaller than the

absolute values of $F_{z'}^{tot}$. Figures 4.2 and 4.3 show that $F_{z'}^{solv}$ is more significant than $F_{z'}^{surf}$ in the range of $z' = 0.4$–0.7 nm for NaCl(001) and $z' = 0.3$–0.7 nm for NaCl(011). This indicates that solvent molecules play an important role in the adsorption of solute ions.

By integrating the forces numerically, the energy profiles of W^{tot}, W^{surf}, and W^{solv} corresponding to $F_{z'}^{tot}$, $F_{z'}^{surf}$, and $F_{z'}^{solv}$ in Figures 4.2 and 4.3, are calculated as shown in Figures 4.4 and 4.5. Every PMF (= W^{tot}) exhibits one or two minima adjacent to the surface, between which the barrier peak exists. Figures 4.6 and 4.7 illustrate the corresponding configurations of the hydrated ion on near the surface, which are determined from the PMF's presented here and the density distributions of water molecules around the ion given elsewhere [Sakakibara, 1997].

1) Adsorption of Na^+ ion

Na^+–NaCl(001). Figure 4.4(a) shows that W^{tot} has two minima at $z' = 0.28$ and 0.56 nm, which are referred to as the first and second minima, respectively. These minima correspond to the "direct adsorption" shown in Figure 4.6(a-i) in which the Na^+ is adsorbed directly on the surface, and the "solvent-separated adsorption" shown in Figure 4.6(a-ii) in which the Na^+ is adsorbed on the surface interposing a water molecule.

At the first minimum of W^{tot}, both W^{surf} and W^{solv} have a minimum. The magnitude of the minimum of W^{surf} is deeper than that of W^{solv}. Hence the stabilization of Na^+ in this minimum is mainly due to the solute–surface interaction and partly due to the solute–water interactions. On the other hand, the second minimum of W^{tot} is largely attributable to W^{solv}, indicating that the solvent-separated adsorption is caused largely by the solute–solvent interactions. Comparison between these minimum values of W^{tot} implies that the direct adsorption is as favorable as the solvent-separated adsorption. Matsui and Jorgensen [1992] evaluated the free energy profiles for Na^+ adsorption onto the

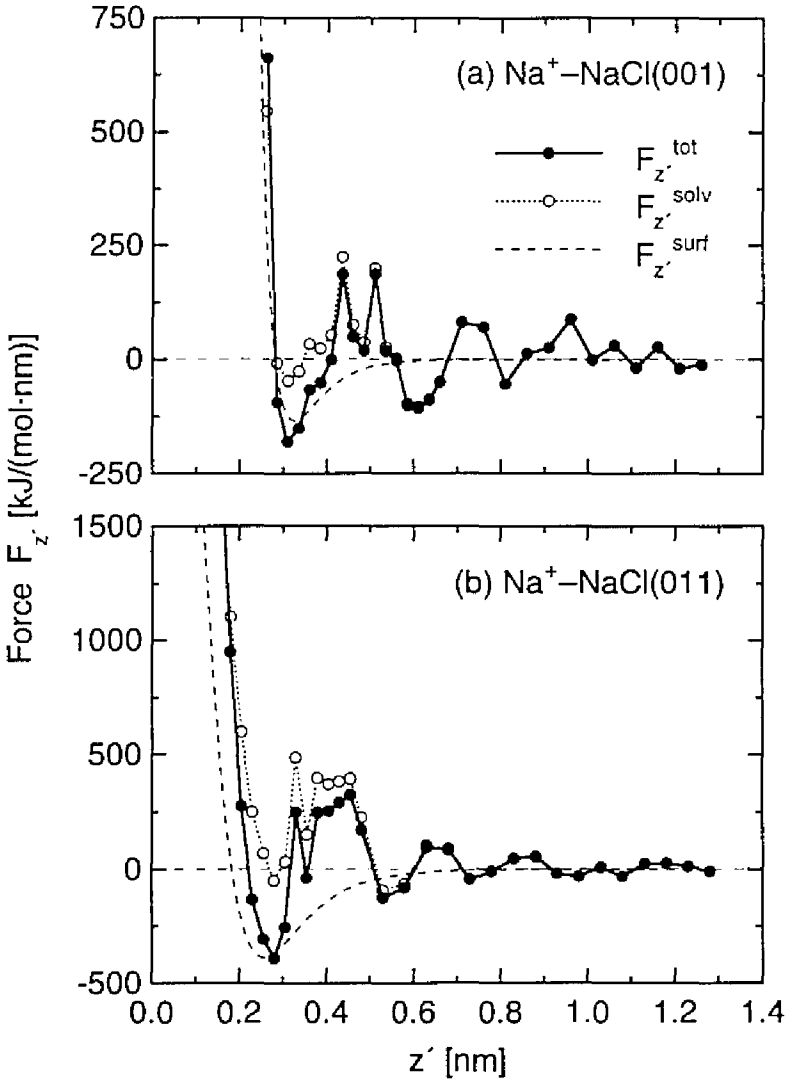

Figure 4.2. Mean force acting on Na^+ as a function of z'. Solid circles indicate the total force $F_{z'}^{tot}$, and open circles and dashed lines represent the solvent and surface contributions, $F_{z'}^{solv}$ and $F_{z'}^{surf}$, respectively. (a) NaCl(001); (b) NaCl(011).

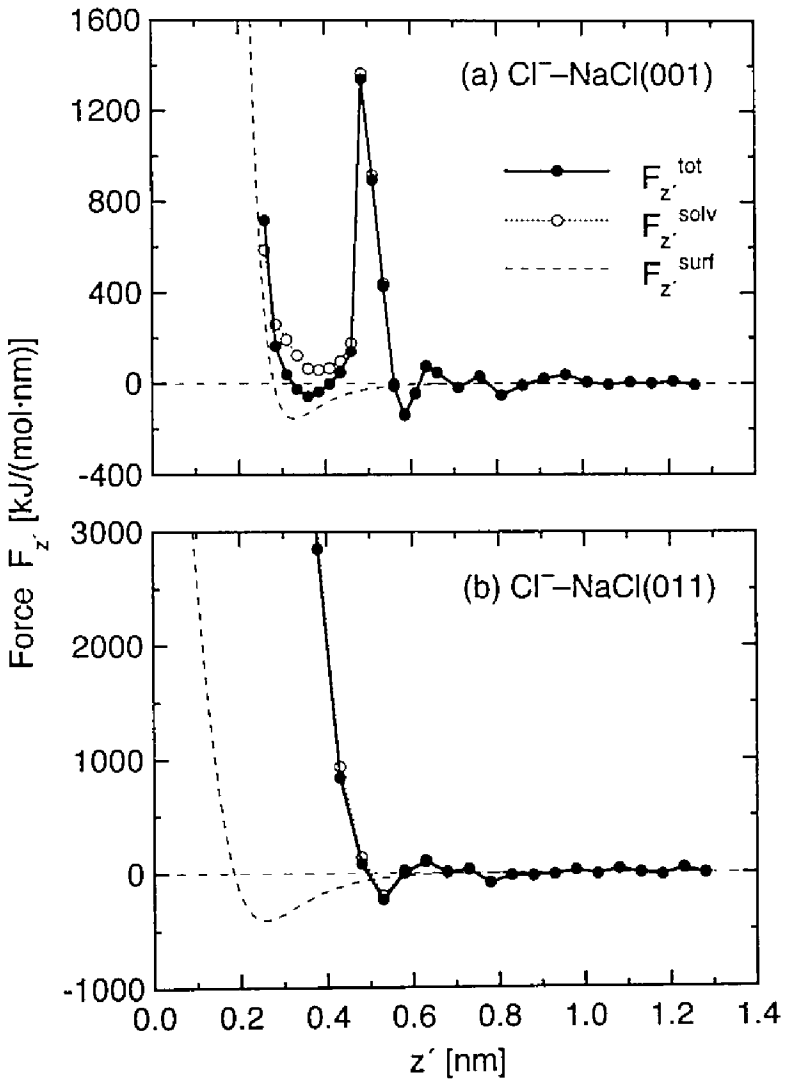

Figure 4.3. Mean force acting on Cl^- as a function of z'. Symbols are the same as in Figure 4.2.

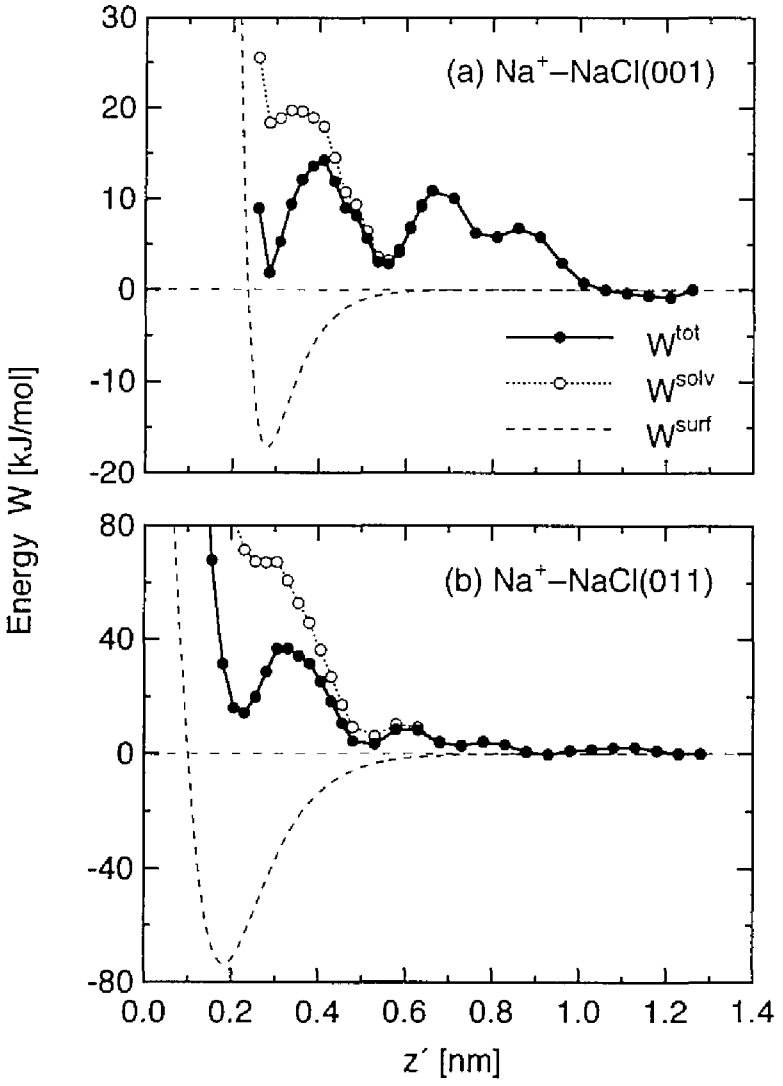

Figure 4.4. Potential of mean force for Na^+. Solid circles indicate the total potential W^{tot}, and open circles and dashed lines represent the solvent and surface contributions, W^{solv} and W^{surf}, respectively. (a) NaCl(001); (b) NaCl(011).

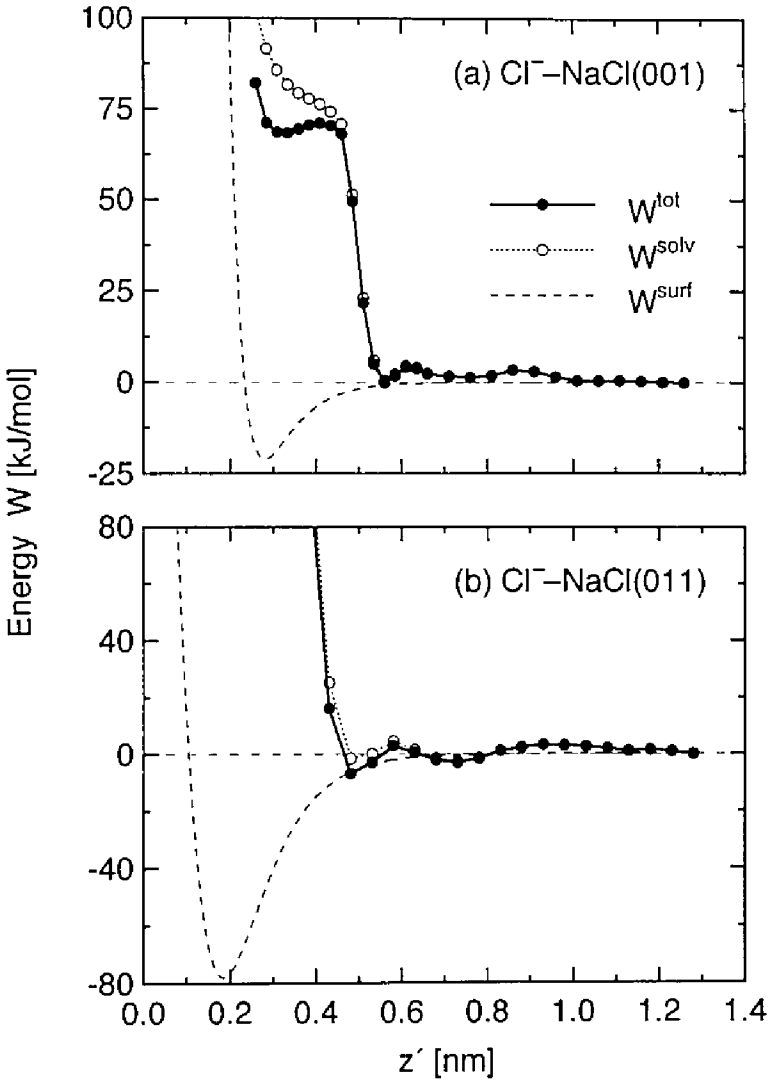

Figure 4.5. Potential of mean force for Cl^-. Symbols are the same as in Figure 4.4.

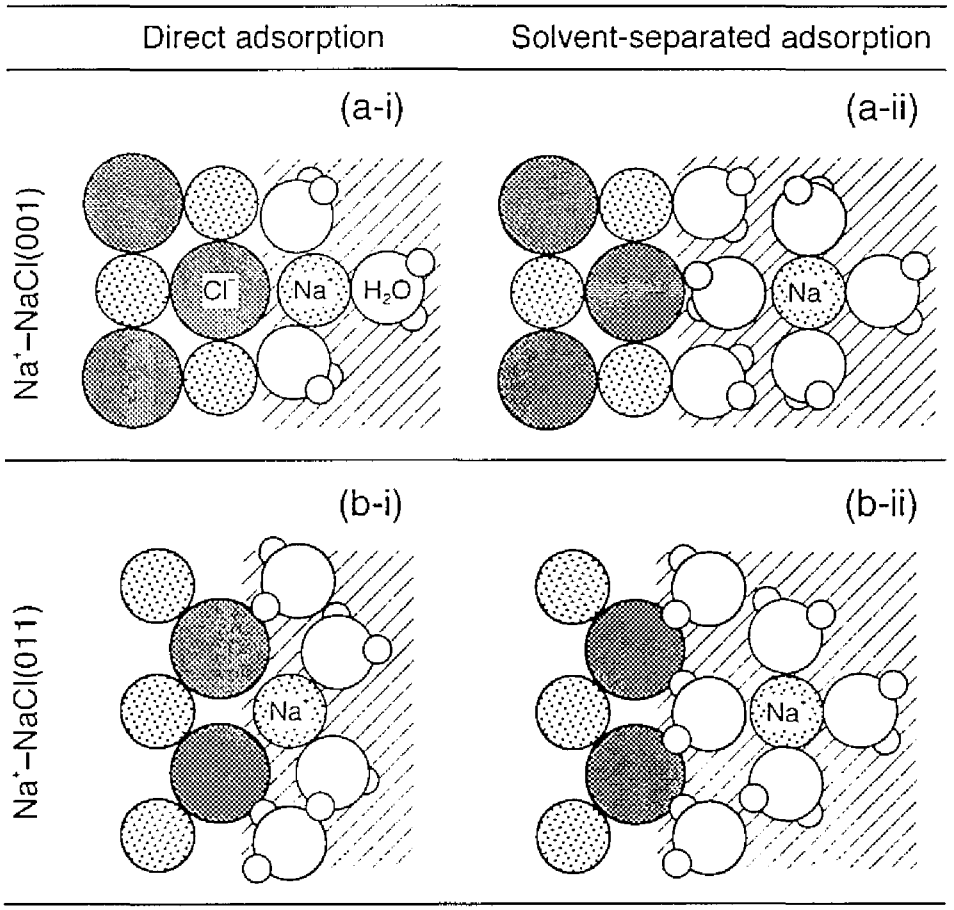

Figure 4.6. Typical configurations of Na^+ at the first and second minima of PMF shown in Figure 4.4 and water molecules near the surface. (a) NaCl(001); (b) NaCl(011).

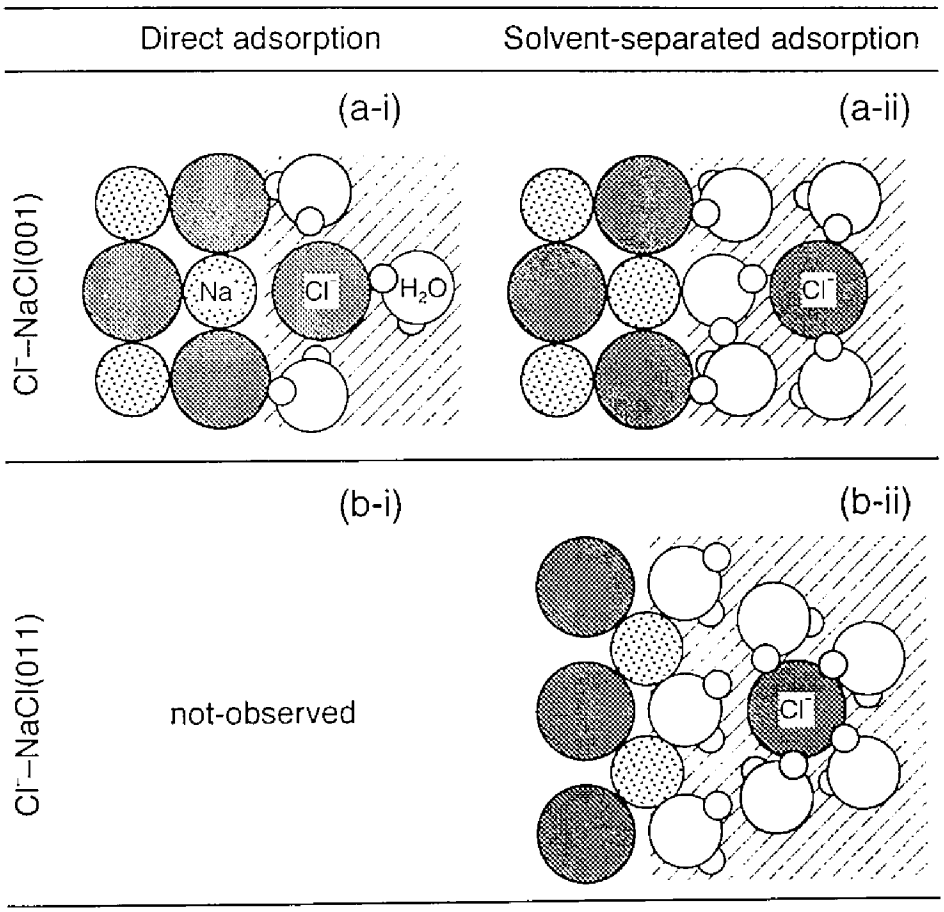

Figure 4.7. Typical configurations of Cl^- at the first and second minima of PMF shown in Figure 4.5 and water molecules near the surface. (a) NaCl(001); (b) NaCl(011).

smooth metal electrode in water and tetrahydrofuran and found that only a single minimum is observed in both cases, which indicates the solvent-separated adsorption. This implies that the atomistic structure of the surface plays an important role in the direct adsorption of an ion.

In order to adsorb directly onto the surface, the Na^+ must overcome the barrier peak of W^{tot} at $z' = 0.41$ nm which is completely due to the solute–water interactions. Figures 4.8(a-i) and (a-ii) display the scatter plots of positions of all the O atoms in H_2O's in L1 and L2 on the surface, when the Na^+ ion is fixed in the first minimum and at the barrier peak of W^{tot}, respectively. Here L1 and L2 were defined previously as in Figure 3.4(a) and the black-looking region means the probable location of water molecules on the surface. As explained in Section 3.3.3, most water molecules in L1 and L2 are located above Na^+ and Cl^- of NaCl(001), respectively.

Figure 4.8(a-i) shows that the water molecules are pulled a little closer to the solute Na^+ and placed above Na^+'s of the surface, which are their favorable positions. This explains why the first minimum of W^{tot} is deep enough and why the minimum of W^{solv} does exist even though it is shallow as shown in Figure 4.4(a). On the other hand, Figure 4.8(a-ii) shows the following features: (i) the solute Na^+ pushes out the water molecule interposed between the surface and itself; and (ii) the water molecules around the solute Na^+ are not placed in their favorable locations. The former behavior requires the energy corresponding to the binding energy of an H_2O on NaCl(001), which is 9 kJ/mol as shown in Figure 4.1(a-i). The latter indicates that the interaction force acts on the Na^+ such that the water molecules recover their favorable adsorption on the NaCl surface. These reflect on the magnitude of the barrier of W^{solv} at $z' = 0.41$ nm, 15 kJ/mol, but the net energy barrier is reduced to the barrier of W^{tot} by the solute–surface attraction of W^{surf}. Thus the energy barrier of W^{tot}, ΔG^{bar}, is determined.

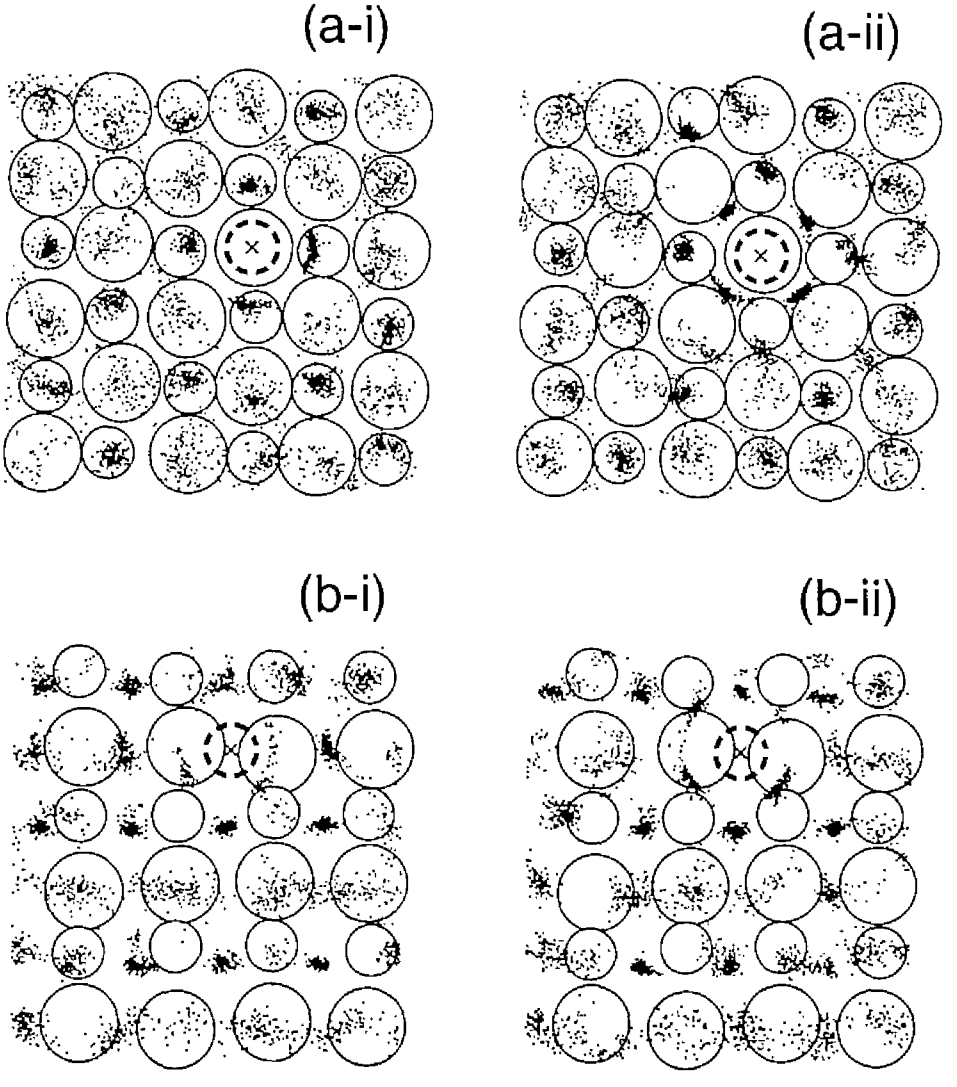

Figure 4.8. Scatter plots of positions of all the O atoms in H_2O's in L1 and L2 on the NaCl surface, when Na^+ is fixed in the first minimum and at the barrier peak of PMF shown in Figure 4.4. Parts a and b in #1 in panel (#1-#2) indicate plots for surfaces of NaCl(001) and NaCl(011), respectively; and parts i and ii in #2 represent plots for the ion fixed in the first minimum and at the barrier peak, respectively. Positions of the O atoms (x, y) are marked by dots every 0.2 ps for 26 ps and the solute ion is marked by the dashed circle. Outermost Na^+'s and Cl^-'s of the NaCl crystal are depicted by small and large circles, respectively.

Na^+–NaCl(011). Figure 4.4(b) shows that W^{tot} has two minima at $z' = 0.23$ and 0.53 nm and the barrier peak at $z' = 0.33$ nm. The direct adsorption at the first minimum shown in Figure 4.6(b-i) is caused by the solute–surface interaction. The solvent-separated adsorption at the second minimum shown in Figure 4.6(b-ii) is caused mainly by the solute–water interactions. The magnitude of these minima indicates that the solvent-separated adsorption is more favorable than the direct adsorption.

As mentioned in Section 3.3.3, water molecules in L1 and L2 tend to be located above a midpoint between two nearest-neighboring Na^+'s and Cl^-'s of NaCl(011), respectively. Figure 4.8(b-i) illustrates that the water molecules around the solute Na^+ placed in relatively favorable positions; but they are placed in somewhat unfavorable positions, as in Figure 4.8(b-ii). The former behavior explains why the solvent contribution of W^{solv} to the first minimum of W^{tot} is negligible, as shown in Figure 4.4(b). The latter indicates that the energy barrier of W^{solv}, which is estimated to be 61 kJ/mol from Figure 4.4(b), is mostly ascribed to the energy required to push out a water molecule bound on NaCl(011), which is 47 kJ/mol as shown in Figure 4.1(b-i).

Energy barrier for direct adsorption. It is difficult to compare the above results with the corresponding experimental and simulation data since these data are hardly available. However, as for the energy barrier, ΔG^{bar}, which is given by the difference of W^{tot} between the barrier peak and the second minimum, the value for Na^+ adsorption on the water/Pt(100) interface was reported to be about 25 kJ/mol [Rose and Benjamin, 1991]. The values of ΔG^{bar} for Na^+ adsorption on water/NaCl(001) and water/NaCl(011) interfaces obtained in the present simulations are 11 and 33 kJ/mol, respectively. The author considers that these values agree fairly well and the difference is attributable to the detailed characteristics of the interaction energies among ions, water molecules, and the

material surfaces. The reason why ΔG^{bar} for NaCl(011) is larger than that for NaCl(001) is mainly because the water molecule which the solute Na^+ has to push out is bound on the NaCl(011) more strongly than on the NaCl(001), as expected from Figures 4.1(a-i) and (b-i).

2) Adsorption of Cl^- ion

Cl^-–NaCl(001). Figure 4.5(a) shows that W^{tot} has two minima at $z' = 0.34$ and 0.56 nm, which indicate the direct adsorption and the solvent-separated adsorption illustrated in Figures 4.7(a-i) and (a-ii), respectively. The magnitude of these minima suggests that the solvent-separated adsorption is more favorable than the direct adsorption.

Figures 4.9(a-i) and (a-ii) picture the density distributions of adsorbed water molecules on the surface when the Cl^- is fixed in the first minimum and at the barrier peak ($z' = 0.41$ nm), respectively. The positions of water molecules around the solute Cl^- do not look to be too far from their favorable positions in both cases. This implies that the force to recover the favorable adsorption is not too strong. Then, why ΔG^{bar} is so high compared with that for the Na^+–NaCl system? It is considered that there are following two contributions in the energy to push out a water molecule bound on the surface: (i) the contribution of the binding energy of a water molecule on the surface; and (ii) the geometric contribution which arises from a combination of the ionic size and the lattice arrangement of the surface. The binding energy of an H_2O on NaCl(001) is –43 kJ/mol as shown in Figure 4.1(a-ii), but only this can not explain the high energy barrier of $\Delta G^{bar} = 71$ kJ/mol. Hence the large value of ΔG^{bar} is attributable to the geometric reason that the large Cl^- must push out the stable water molecule contained in the hollow site, as illustrated in Figure 4.7(a-ii).

Cl^-–NaCl(011). Figure 4.5(b) shows that W^{tot} has a minimum at $z' = 0.48$ nm, but has no minimum in the region of $z' < 0.48$ nm; that is, the PMF is

repulsive and direct adsorption of the Cl^- on the NaCl(011) is very unfavorable. Figure 4.9(b-ii) illustrates the density distribution of adsorbed water molecules when the Cl^- is fixed at $z' = 0.38$ nm ($W^{tot} = 108$ kJ/mol). The point to note is that a water molecule can not be pushed out to be interposed between the Cl^- and the surface. Because the water molecule is adsorbed on the hollow site tightly as illustrated in Figure 4.7(b-ii), the geometric contribution will be extremely repulsive. This is the reason why ΔG^{bar} is remarkably large.

Energy barrier for direct adsorption. The value of ΔG^{bar} for Cl^-–NaCl(001) is found to be 71 kJ/mol, which is much larger than the value of 4 kJ/mol for Cl^-–Pt(100) reported by Rose and Benjamin [1991]. This difference is explained as follows. In the adsorption of Cl^- on NaCl(001), the adsorption sites of Cl^- and H_2O are the same and so a water molecule contained in the hollow site must be pushed out completely. In the adsorption of Cl^- on Pt(100), water molecules are pushed just aside, because the Cl^- adsorbs in between the bound water molecules [Rose and Benjamin, 1991].

3) Adsorption characteristics of Na^+ and Cl^- ions

The characteristics of Na^+ and Cl^- adsorption are compared and summarized as follows:

(i) Na^+ and Cl^- ions are adsorbed on the NaCl-crystal surfaces either directly (i.e., direct adsorption) or with a water molecule interposed between the surface and themselves (i.e., solvent-separated adsorption). The former adsorption is mainly attributable to the solute–surface interaction and the latter is entirely due to the solute–water interactions.

(ii) Na^+ and Cl^- ions are adsorbed more stably on the surfaces under solvent-separated conditions in most cases. This agrees with the results given elsewhere [Sakakibara, 1997]; even though the ions are placed at the their direct adsorption points, they move to the points for their solvent-separated

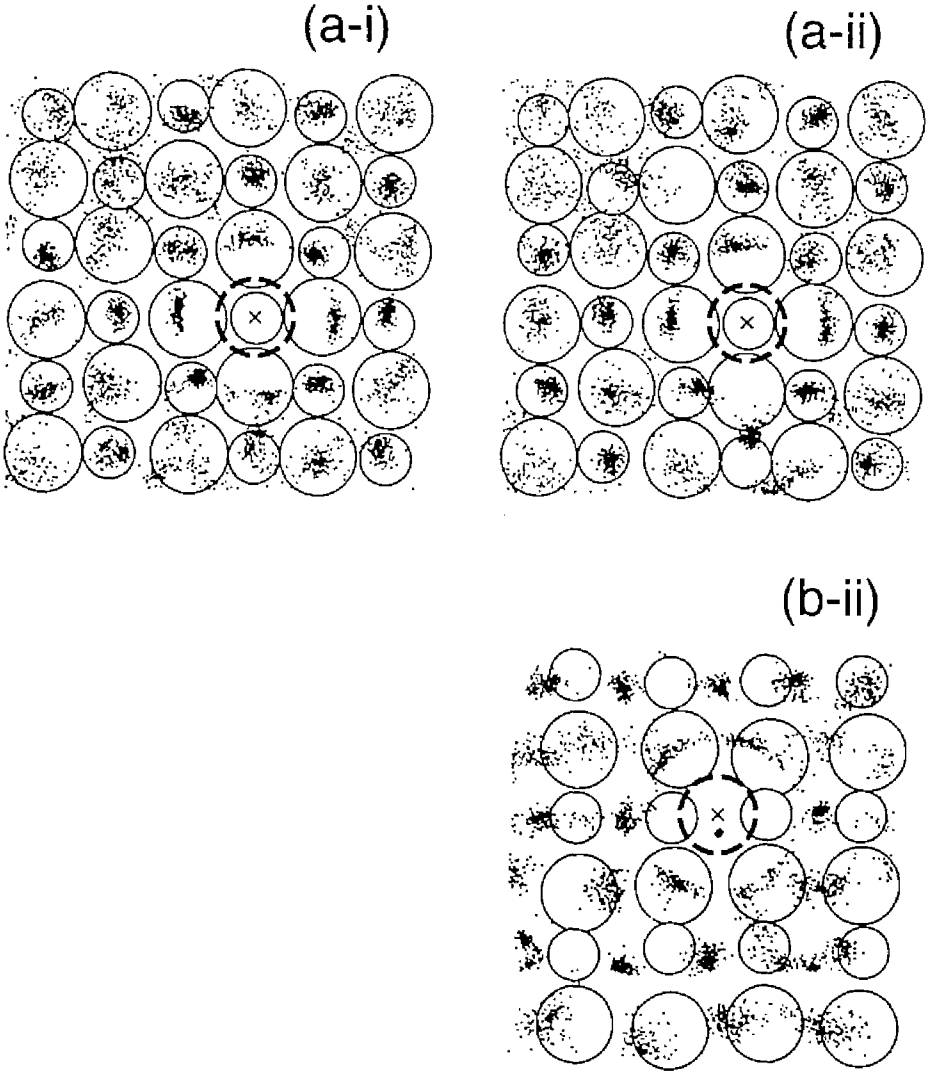

Figure 4.9. Scatter plots of positions of all the O atoms in H_2O's in L1 and L2 on the NaCl surface, when Cl^- is fixed in the first minimum and at the barrier peak of PMF shown in Figure 4.5. Plots in panels (a-i) and (a-ii) are obtained through the same procedure as in Figure 4.8. The plot corresponding to panel (b-i) is not shown because no first minimum is obtained in this case, and panel (b-ii) represents the plot for the ion fixed at the barrier of PMF, $z' = 0.38$ nm ($W^{\infty} = 108$ kJ/mol).

adsorption or diffuse into the bulk water.

(iii) The Na^+ adsorb directly onto the NaCl surface more easily than the Cl^-, where the direct adsorption of Cl^- on NaCl(011) is impossible. This is due to the geometric reason that the large Cl^- must push out a stable water molecule contained in the hollow site.

4.3.3 Solvation of solute ions

The hydration number of the solute ion, n_h, is calculated as a function of z' and shown in Figure 4.10. Water molecules are regarded as belonging to the hydration shell around the ion if the ion–oxygen distance is less than or equal to 0.30 nm for an Na^+ and 0.40 nm for a Cl^-, which are the distance at the first minimum of the ion–oxygen pair correlation function in the bulk. Every n_h is nearly constant in the range of $z' > 0.7$ nm and increases slightly as the solute ion approaches the point in which the ion is adsorbed under the solvent-separated condition. This increase is probably because the ion approaches the denser layer of adsorbed water molecules, as shown in Figure 3.4 previously. But when the ion comes closer to the surface, n_h decreases. This decrease is mainly because the solute ion pushes out the water molecule on the adsorption site and partly because the ion itself dehydrates. Comparison of n_h between NaCl(001) and NaCl(011) suggests that the decreases for NaCl(011) are more remarkable than those for NaCl(001). This also explains why the values of ΔG^{bar} for NaCl(011) are larger than those for NaCl(001).

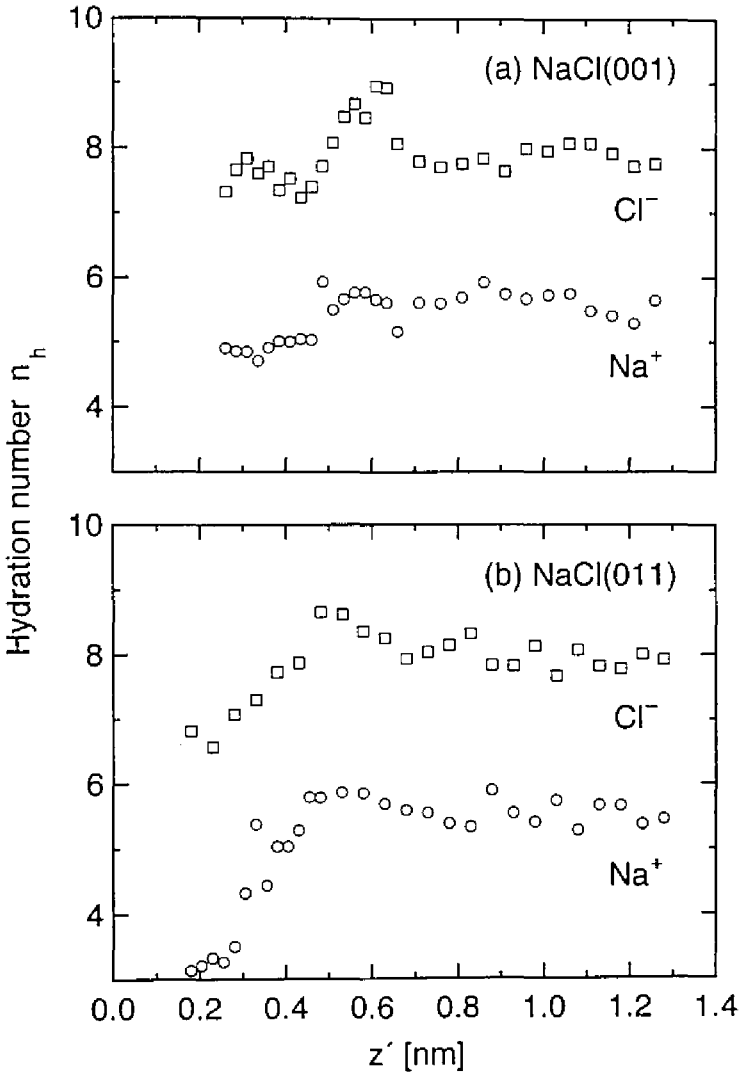

Figure 4.10. Hydration number of a solute ion, n_h, as a function of z'. Circles and squares indicate Na^+ and Cl^-, respectively. (a) NaCl(001); (b) NaCl(011).

4.4 Concluding remarks

In this chapter, free energy profiles for Na^+ and Cl^- adsorption onto the NaCl(001) and NaCl(011) surfaces are evaluated using MD simulations and the following conclusions are drawn:

(i) Na^+ and Cl^- ions are adsorbed on the NaCl-crystal surface either directly (i.e., direct adsorption) or with a water molecule interposed between the surface and themselves (i.e., solvent-separated adsorption).

(ii) Both ions are adsorbed more stably on the NaCl surface under solvent-separated conditions in most cases.

(iii) In the case of direct adsorption, Na^+ adsorbs on the NaCl surface more easily than Cl^- in which the direct adsorption of Cl^- on NaCl(011) is impossible.

(iv) The solute–surface and solvent–surface interactions are strongly affected by the lattice arrangement of the surface; hence, the free energy profile largely depends not only on the size of the solute ion but also on the lattice arrangement.

5
Surfactant Adsorption onto Liquid/Solid Interfaces

5.1 Introduction

This chapter focuses on the MD simulation of the surfactant aggregation at a liquid/solid interface. For this purpose, the simple description of water, oil, and surfactant molecules is given and applied also to the interactions between these molecules and a solid surface. It is necessary to examine whether this model can capture the basic characteristics of water/solid interfaces and micellar solutions. The results given by the simple model simulations are compared in detail with those by atomistic model simulations, presented in Chapters 2 and 3, and other studies.

Thereafter, the surfactant aggregation on the solid surface in a micellar solution is simulated. The mechanism of the adsorption and aggregation of surfactants on the surface is proposed. How this mechanism is influenced by the concentration and molecular structure of surfactants is discussed in detail.

5.2 Methods

5.2.1 Simple model for oil/water/surfactant systems

The simple description of an oil/water/surfactant system has been developed by Telo da Gama and Gubbins [1986] and by Smit [1988; Smit *et al.*, 1990]. The

starting point of this model is to consider four types of particles, that is, waterlike, oillike, headlike, and taillike particles, which are referred to as w, o, h, and t particles, respectively. The w and h particles are hydrophilic, while the o and t particles are hydrophobic. By use of these particles, water, oil, and surfactant molecules are modeled as illustrated in Figure 5.1: a water molecule consists of one w particle; an oil molecule consists of one o particle; and a surfactant molecule is composed of a headgroup of h particles and a tail chain of t particles, whose neighboring pairs are connected together by the harmonic potential, u_{ij}^{bond}, with spring length l_0 and spring constant k:

$$u_{ij}^{\text{bond}}(r) = \frac{1}{2} k (r - l_0)^2, \tag{5.1}$$

where r is the distance between particles i and j. The values of $l_0 = d_S$ and $k = 1.4 \times 10^4 \varepsilon_S / d_S^2$ are used, where d_S and ε_S are the size and energy parameters for the Lennard-Jones potential, respectively, as described below. It is confirmed that this spring is stiff enough to constrain the separations of all the connected particles to be $d_S \pm 0.02\, d_S$.

In addition to the harmonic potentials, pairs i and j between four species of particles (w, o, h, and t) interact each other via the shifted Lennard-Jones (12–6) potential with energy parameter ε_{ij}, core diameter d_{ij}, and cutoff radius R_{ij}^{cut}:

$$u_{ij}(r) = \begin{cases} \phi_{ij}(r) - \phi_{ij}(R_{ij}^{\text{cut}}), & r \le R_{ij}^{\text{cut}}, \\ 0, & r > R_{ij}^{\text{cut}}, \end{cases} \tag{5.2a}$$

$$\phi_{ij}(r) = 4\varepsilon_{ij} \left[\left(\frac{d_{ij}}{r} \right)^{12} - \left(\frac{d_{ij}}{r} \right)^{6} \right]. \tag{5.2b}$$

The values of parameters used are as follows: $\varepsilon_{ij}/k_B = \varepsilon_S/k_B = 119.8$ K and $d_{ij} = d_S = 0.3405$ nm for all interactions, and $m_S = 39.948$ g/mol for the mass of all particles, which correspond to the values for argon.

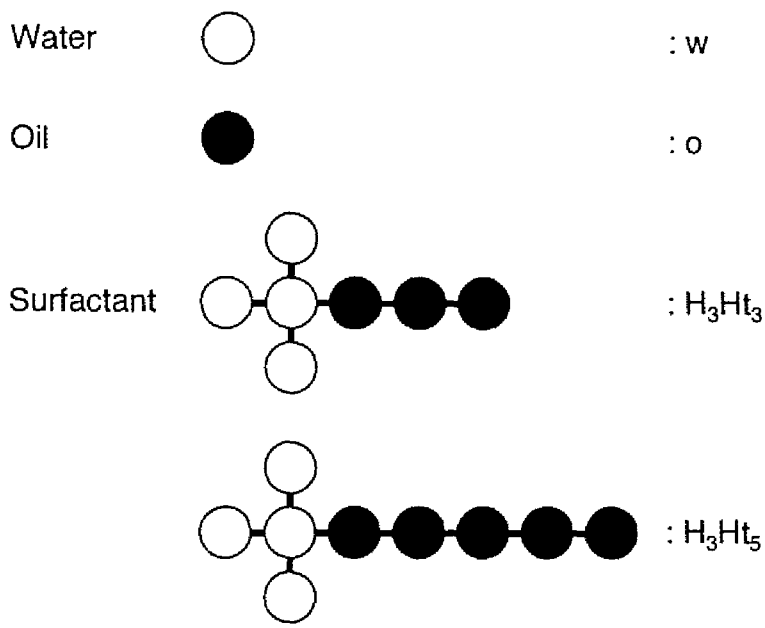

Figure 5.1. Illustration of the simple models of water, oil, and surfactant molecules. Symbols w, o, H, and t denote waterlike, oillike, headlike, and taillike particles, respectively. Two surfactants used are displayed.

TABLE 5.1: Cutoff radius R_{ij}^{cut} for Lennard-Jones interactions between four species of particles, w, h (or H), o, and t (in unit of d_S)

	w	h (H)	o	t
w	2.5	2.5	$2^{1/6}$	$2^{1/6}$
h (H)	2.5	2.5 ($2^{1/6}$)	$2^{1/6}$	$2^{1/6}$
o	$2^{1/6}$	$2^{1/6}$	2.5	2.5
t	$2^{1/6}$	$2^{1/6}$	2.5	2.5

To represent the hydrophilicity and hydrophobicity, different values of R_{ij}^{cut}, $2.5d_S$ and $2^{1/6}d_S$, are chosen depending on the types of pairs. The intraspecies interaction includes repulsive and attractive forces using $R_{ij}^{cut} = 2.5d_S$, while the interspecies interaction is completely repulsive using $R_{ij}^{cut} = 2^{1/6}d_S$ (see Figure 5.3). Nonionic and ionic surfactants are modeled using $R_{ij}^{cut} = 2.5d_S$ and $2^{1/6}d_S$ for h–h interaction, respectively. In the latter case, only the repulsion exists between particles of the headgroups, which are designated by H instead of h. This is analogous to the electrostatic repulsion between charged headgroups of real ionic surfactants. The values of R_{ij}^{cut} are summarized in Table 5.1. Note that the model surfactant is flexible compared with a real surfactant whose conformation is restricted by the bending and torsional angles. Although it is possible to incorporate the potentials of these angles into the model surfactant, this spoils the advantage of the simple model, that is, the *simplicity*.

By connecting different number of particles h (or H) and t in different arrangement, the simple model can create surfactants with various molecular architectures. In the present study, two types of the surfactants, H_3Ht_3 and H_3Ht_5, are considered as illustrated in Figure 5.1, which are different in tail length but the same in repulsive headgroup.

5.2.2 Simple model for solid walls

The solid wall, illustrated in Figure 5.2, is represented by the structureless (10–4–3) potential [Steele, 1973]:

$$u_{wj}(z) = \begin{cases} \psi(z) - \psi(Z_{wj}^{cut}), & z \le Z_{wj}^{cut}, \\ 0, & z > Z_{wj}^{cut}, \end{cases} \tag{5.3a}$$

$$\psi(z) = 2\pi\varepsilon_{ws}\rho_w d_{ws}^2 \Delta \left[\frac{2}{5}\left(\frac{d_{ws}}{z}\right)^{10} - \left(\frac{d_{ws}}{z}\right)^{4} - \frac{d_{ws}^4}{3\Delta(z + 0.61\Delta)^3} \right], \tag{5.3b}$$

where z is the perpendicular distance between the center of a Lennard-Jones particle and the outermost plane of the solid wall, Z_{wj}^{cut} is the cutoff separation, ρ_w is the number density of atoms in the solid wall, and Δ is the separation between lattice planes. ε_{ws} and d_{ws} are the cross-parameters for wall–solution interaction, which are written by

$$\varepsilon_{ws} = (\varepsilon_w \varepsilon_s)^{1/2}, \qquad d_{ws} = \frac{1}{2}(d_w + d_s). \tag{5.4}$$

The parameters for the graphite surface are used following Steele [1973, 1974]:

$$\begin{aligned} \varepsilon_w/k_B &= 28.0\ \text{K}, & d_w &= 0.340\ \text{nm}, \\ \rho_w &= 114\ \text{nm}^{-3}, & \Delta &= 0.335\ \text{nm}. \end{aligned} \tag{5.5}$$

Using these values, the particle–wall potential given by Equation (5.3b) is calculated as shown in Figure 5.3.

To represent the hydrophilic and hydrophobic walls, the idea of the simple model is applied also to the particle–wall interaction; that is, when a particle and a wall are of the same kind, their interaction includes repulsive and attractive forces using $Z_{wj}^{cut} = \infty$ (i.e., no truncation), but otherwise they interact only through the repulsion using $Z_{wj}^{cut} = 0.994 d_s$ $(= Z_{min})$.

When a basic cell with dimensions $L_x \times L_y \times L_z$ is given, a particle located at z

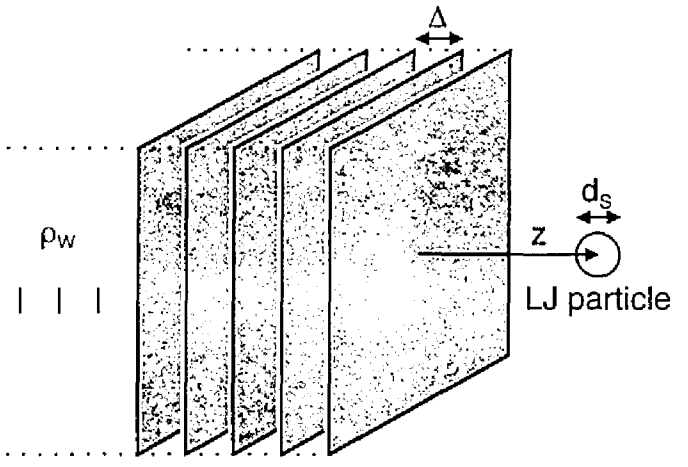

Figure 5.2. Schematic of the solid wall represented by the structureless (10–4–3) potential. The solid wall is a sequence of crystallographic planes separated by distance Δ. ρ_w denotes the number density of atoms per volume of the solid.

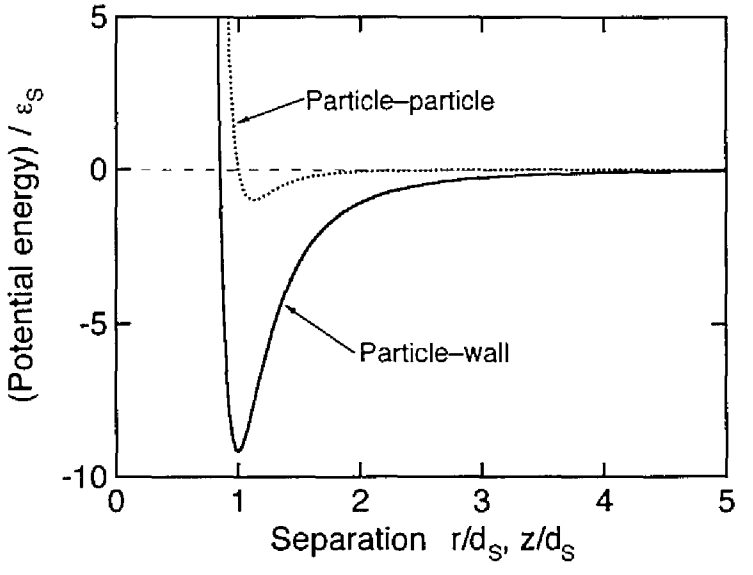

Figure 5.3. Potential energies for particle–particle and particle–wall interactions represented by Equations (5.2b) and (5.3b), respectively.

experiences the external potential, $u_{wj}^{ext}(z)$, given by the superposition of u_{wj} from two planar walls, whose outermost planes are positioned at $z = -L_z/2$ and $+L_z/2$:

$$u_{wj}^{ext}(z) = u_{wj}(z + L_z/2) + u_{wj}(L_z/2 - z), \tag{5.6}$$

where the origin of coordinates is taken at the center of the cell. The effective length of this cell in the z direction is defined as the separation between the points of $z = -L_z/2 + Z_{min}$ and $L_z/2 - Z_{min}$, where each u_{wj} on the right-hand side of Equation (5.6) has a minimum.

5.2.3 Driving force of surfactant adsorption on the surface

It is found that the surfactants of H_3Ht_3 and H_3Ht_5 do not adsorb on the hydrophilic wall in a waterlike fluid, as far as the potentials described in Section 5.2.2 are used for particle–wall interactions; but the surfactants do adsorb on the hydrophobic wall. In a real system, the surfactant adsorption on a hydrophilic surface is promoted mainly by the strong electrostatic head–surface interactions. A hydrophobic surface interacts weakly with a surfactant through the van der Waals attraction, but water molecules dislike the hydrophobic tail of the surfactant to repel it toward the surface; that is, the surfactant adsorption on the hydrophobic surface is induced by the solvent.

For this reason, the adsorption of model surfactants is promoted by the following presumption. The H particle centered in the surfactant headgroup, which is denoted by H′, interacts with the hydrophilic wall ten times more strongly than the other H particles and w particles; that is, the energy parameter for H′–wall interaction is given by $10\varepsilon_{ws}$. Although this assumption is very rough, it mimics the real system in which a charged headgroup of a surfactant interacts with a hydrophilic surface more strongly than a water molecule (see Appendix A). On the other hand, no additional force is incorporated into the interactions between the

TABLE 5.2: Systems of MD simulations

System	N^a	$L_x \times L_y \times L_z{}^b$	Wall	Fluid	$X_{surf}{}^c$	ρ^*	T^*
I	4,000	17.9 × 17.9 × 19.9	Hydrophilic	w	0.00	0.7	1.00
II	4,000	17.9 × 17.9 × 19.9	Hydrophobic	w	0.00	0.7	1.00
III	19,652	30.4 × 30.4 × 30.4		H_3Ht_5/w	0.92–15.2	0.7	2.40
IV	19,652	30.4 × 30.4 × 30.4		H_3Ht_3/w	0.71–12.5	0.7	1.35
V	19,652	30.4 × 30.4 × 32.1	Hydrophilic	$H_3H't_5$/w	2.66, 9.75	0.7	2.40
VI	19,652	30.4 × 30.4 × 32.1	Hydrophilic	$H_3H't_3$/w	2.07, 7.73	0.7	1.35
VII	19,652	30.4 × 30.4 × 32.1	Hydrophobic	H_3Ht_5/w	2.66, 9.75	0.7	2.40
VIII	19,652	30.4 × 30.4 × 32.1	Hydrophobic	H_3Ht_3/w	2.07, 7.73	0.7	1.35

[a] Total number of particles.
[b] Dimensions of the basic cell in unit of d_S.
[c] Volume fraction of dosed surfactants in unit of volume %; that is, $X_{surf} = (n_{site}N_{surf}/N) \times 100$, where N_{surf} denotes the number of surfactants with n_{site} sites.

surfactant and the hydrophobic wall.

5.2.4 Definition of micelles

When a surfactant solution is treated, a micelle is identified as a cluster of surfactants whose tails are in contact with each other. Two surfactants are considered to belong to the same micelle if the minimum distance between their tail sites is less than $1.4d_S$. According to the clustering procedure [Stoddard, 1978], neighboring surfactants are found out and then all the surfactants are partitioned into micelles and free monomers, which are mutually exclusive.

5.2.5 Simulation details

Eight systems are considered as summarized in Table 5.2, which are classified roughly into the following three systems: (I, II) a waterlike fluid confined within two planar walls; (III, IV) a bulk surfactant solution; and (V–VIII) a surfactant solution between walls. When Systems I, II, and V–VIII are simulated, the

periodic boundary conditions are applied in the two directions parallel to the walls. Systems III and IV are simulated with three-dimensional periodicity. The dimensions of the cell with total 4,000 or 19,652 particles are chosen such that the reduced density of the particles, ρ^* (= $\rho\ d_S^3$), is equal to 0.7. The equation of motion is integrated by the leap-frog method with a time step of $\Delta t = 0.00464\tau_0$, where $\tau_0 = d_S(m_S/\varepsilon_S)^{1/2}$. The reduced temperature, T^* (= k_BT/ε_S), is kept at the constant values listed in Table 5.2 by velocity scaling if necessary.

In order to compute the Lennard-Jones interactions between a large number of particles efficiently, the layered link cell (LLC) procedure connecting with the Verlet neighbor list is employed on the Cray T-94/4128 vector computer [Rapaport, 1988; Grest *et al.*, 1989]. In this procedure, the neighbor list for force calculations is built up as follows: the pairs of interacting particles i and j are found out according to the link cell (LC) algorithm; subsequently, the identity numbers of the pairs, (i, j), are sorted systematically using the "layering algorithm" in order to vectorize all of the force loops. The neighbor list is updated automatically following Chialvo and Debenedetti [1990]. Internal forces of surfactants given by Equation (5.1) are computed in the vector fashion using the multi-color method [Müller-Plathe and Brown, 1991].

The detailed simulation procedures for Systems I–VIII are given as follows.

Systems I, II: Waterlike fluid between planar walls. 4,000 waterlike particles at $T^* = 1.00$ are equilibrated in the cubic cell with a side length of $17.9d_S$ and the three-dimensional periodicity. Then two planar walls are inserted at $z = \pm 9.93d_S$ and the periodicity in the z direction is removed. After that, the system is allowed to re-equilibrate over 4×10^4 time steps by velocity scaling. The simulation is performed for 1×10^3 time steps without scaling.

Systems III, IV: Bulk surfactant solution. After 19,652 waterlike particles are equilibrated at the given temperature, some of the particles are

connected at random by the springs of Equation (5.1) such that a specific number of surfactants are constructed. But all the particles of the surfactants are still regarded as w particles to prevent the surfactants from assembling spontaneously, which are referred to as *pseudo*-surfactants. For stable computation, the spring constant k is started from the initial value of $1.4\varepsilon_S/d_S^2$ and gradually increased to the final value of $1.4 \times 10^4 \varepsilon_S/d_S^2$ for 3×10^4 time steps. Then the system is equilibrated over 4×10^4 time steps, in which *pseudo*-surfactants hardly assemble. Thereafter, the head and tail particles are treated as H and t particles, respectively, and the surfactants are allowed to assemble for 1.5×10^5 time steps with temperature scaling at every 100th step. The equilibrated surfactant solution is simulated by the successive calculation over 1.5×10^5 time steps with scaling at every 200th step.

Through this procedure, which seems to be intricate, the self-assembly of surfactants becomes possible. The more refined procedure is presented in Section 7.3.2.

Systems V–VIII: Surfactant solution between planar walls. Since the initial configurations of surfactants may affect the surfactant aggregation under the limited numbers of molecules, two types of configurations are prepared:

(I) A solvent and *pseudo*-surfactant mixture between the walls is equilibrated over 7×10^4 time steps as mentioned above.

(II) The same procedure as Type I is taken except that H′ particles of the surfactants are treated as H particles, where the surfactants have no driving force of the adsorption and are designated by *inert*-surfactants.

Note that Type II is available only when the hydrophilic surface is employed. During these preparations, the *pseudo*-surfactants neither aggregate anywhere nor adsorb on the hydrophilic and hydrophobic surfaces in Type I. In the case of Type II, the *inert*-surfactants aggregate in the bulklike region and hardly adsorb on the

hydrophilic surface. Thereafter, the *pseudo*-surfactants or *inert*-surfactants replaced by the true surfactants, they are allowed to both aggregate and adsorb for 3×10^5 time steps with scaling at every 200th step.

Simulations starting from the configurations of Types I and II would correspond to the following conditions:

(I) Surfactant monomers are putted into water on a solid wall, in which the monomers assemble in the bulk and adsorb onto the wall.

(II) A wall is inserted into an equilibrated surfactant solution, in which the aggregates formed adsorb onto the wall.

5.3 Verification of the simple model

First of all, it should be checked whether the simple model used can represent the basic characteristics of water/solid interfaces and micellar solutions. The former problem is examined in Section 5.3.1 using Systems I and II and the latter is examined in Section 5.3.2 using Systems III and IV.

5.3.1 Waterlike fluids near solid walls

Density profiles. Figure 5.4 shows the density profile of waterlike particles near the wall, which is hydrophilic for System I and hydrophobic for System II. About four layers of the particles are formed near the hydrophilic surface, whereas the hydrophobic surface repels the particles toward the middle region of the cell such that no distinct layer is formed anywhere. The similar features were observed also in the atomistic model simulations, as described in Sections 2.4.1 and 3.3.2.

Diffusion coefficients. To probe the motion of particles near the surface, the fluid lamina is divided into three interfacial layers (L1, L2, and L3) and the

TABLE 5.3: Diffusion coefficients D^{*} [a] of waterlike particles in the different layers for Systems I and II

	System I (hydrophilic wall)				System II (hydrophobic wall)			
Layer [b]	L1	L2	L3	LB	L1	L2	L3	LB
D_x^{*} [c]	0.09	0.09	0.11	0.12	0.24	0.14	0.11	0.10
D_y^{*} [c]	0.08	0.09	0.11	0.13	0.21	0.13	0.11	0.10
D_z^{*} [d]	0.01	0.03	0.07	0.11	0.26	0.12	0.10	0.10
(D_z^{*}) [c]	(≈0.00)	(≈0.00)	(≈0.00)	(0.12)	(≈0.00)	(0.01)	(0.01)	(0.09)

[a] $D^{*} = D/d_S(\varepsilon_S/m_S)^{1/2}$.
[b] The range of $|z|$ in unit of d_S is 8.40~ for L1, 7.42–8.40 for L2, 6.57–7.42 for L3, and 0.00–3.50 for LB (see Figure 5.4).
[c] Values are calculated by the mean square displacement.
[d] Values are calculated by the residence autocorrelation function.

bulklike region (LB), as defined in Figure 5.4 and Table 5.3. The self-diffusion coefficients of D_ξ in the direction ξ (= x, y, z) are calculated within these layers using Equation (2.16), as given in Table 5.3. The values of D_z, which are given in parentheses, are nearly zero in the thin layers of L1, L2, and L3, but they are almost equal to those of D_x and D_y in LB with a thickness of $3.5d_S$. This implies that Equation (2.16) is not appropriate for evaluating the vertical diffusion coefficient of particles within a thin film, as pointed out in Section 2.4.4. Alternatively, the residence autocorrelation function using Equations (2.18) and (2.19) gives the appropriate values of D_z as in Table 5.3.

It is found that the diffusion coefficients of waterlike particles in L1, L2, and L3 decrease near the hydrophilic surface compared with those in LB, while they increase near the hydrophobic surface. This tendency becomes more significant as the particles are closer to the surfaces. These features are in qualitative agreement with the results by the atomistic model simulations discussed in Sections 2.4.4 and 3.3.6.

Thus, the results of density profiles and diffusion coefficients manifest that the simple model used can mimic, at least qualitatively, the water/solid interfaces with

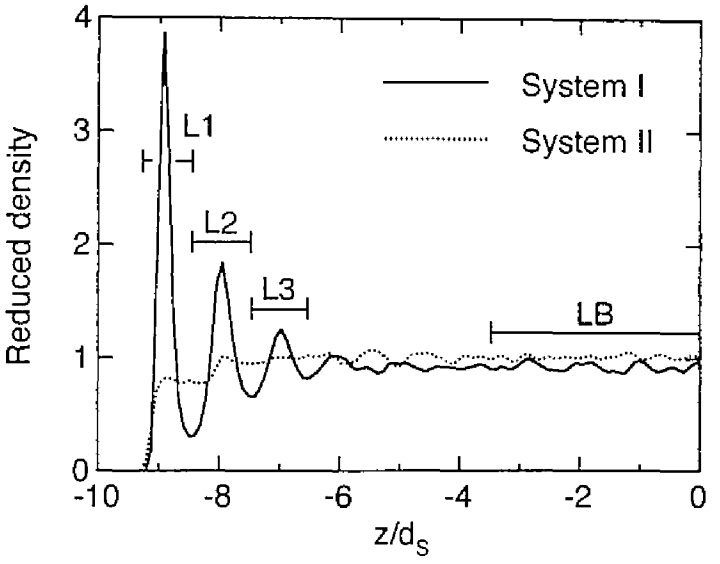

Figure 5.4. Density profile of waterlike particles near the planar wall. Solid and dotted lines represent the profiles near the hydrophilic wall (System I) and near the hydrophobic wall (System II), respectively.

respect to the static structure and the diffusional motion of layered particles.

5.3.2 Self-assembly of surfactants

Snapshot. A surfactant solution in the bulk is investigated in detail using System III. Figure 5.5 displays a typical snapshot of the H_3Ht_5 surfactants in 3.48 vol % solution. Surfactants assemble spontaneously to form micelles, at least apparently, in which the headgroups are directed outward, while the tail chains are folded inside to be away from waterlike particles. It is also observed that a few surfactants are dissolved in the solvent as free monomers.

Aggregate size distributions. For quantitative treatment of a micellar solution, the size distributions of aggregates are calculated to determine the critical micelle concentration (CMC). The volume fraction of surfactants in aggregates of size n, $X(n)$, is depicted in Figure 5.6 for various values of the dosed surfactant concentration, X_{surf}. The point to observe is that the distribution has a maximum and a minimum only when X_{surf} becomes larger than the value of about 3 vol %. Otherwise the distribution decreases monotonically. This behavior is identical to (i) the basic assumption in a theory of micelle formation dynamics [Lang and Zana, 1987] and coincides with (ii) the results by other simulations [Larson, 1992; Rector *et al.*, 1994; Haliloglu and Mattice, 1994; Desplat and Care, 1996] and (iii) those by the analytical models [Hoeve and Benson, 1957; Wennerström and Lindman, 1979].

Critical micelle concentration. The free monomer concentration $X(1)$ as a function of X_{surf} is shown in Figure 5.7, where the dotted line indicates the relation $X(1) = X_{surf}$. $X(1)$ is directly proportional to X_{surf} up to $X_{surf} \approx 1$ vol %, implying that the surfactants do not form aggregates. This is consistent with the monotonic decrease of $X(n)$ in Figure 5.6. At $X_{surf} > 3$ vol %, $X(1)$ becomes nearly constant, from which the CMC is taken to be about 3 vol % for an H_3Ht_5 surfactant solution

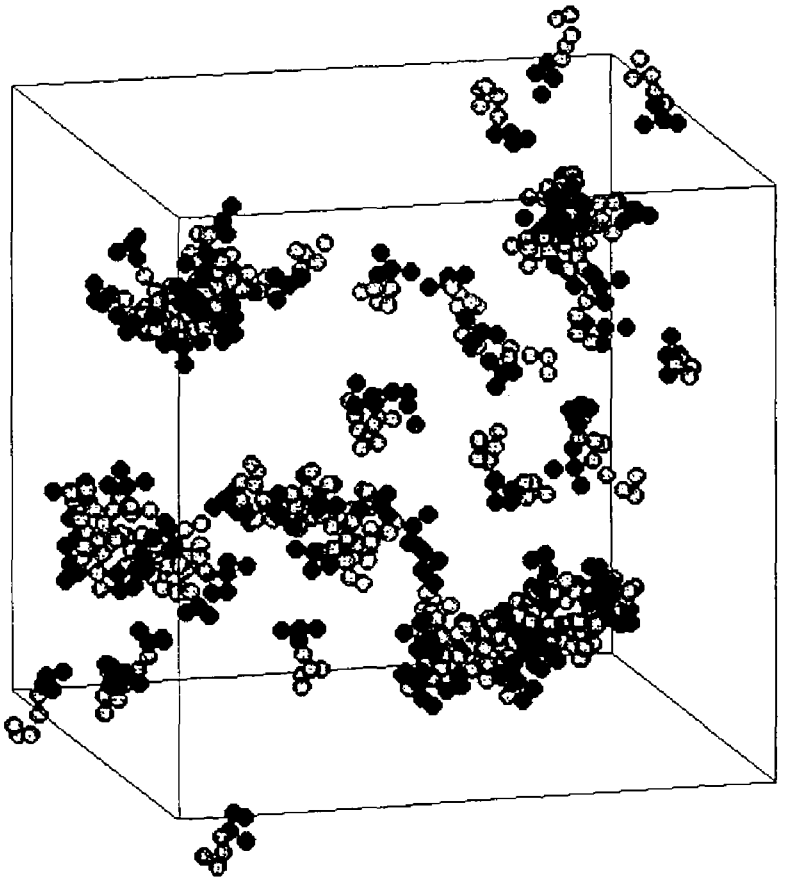

Figure 5.5. Typical snapshot of System III at X_{surf} = 3.48 vol %. Dark and light spheres display the headlike and taillike particles of surfactants, respectively. All solvent particles are not shown for clarity. The simulation cell is depicted by lines.

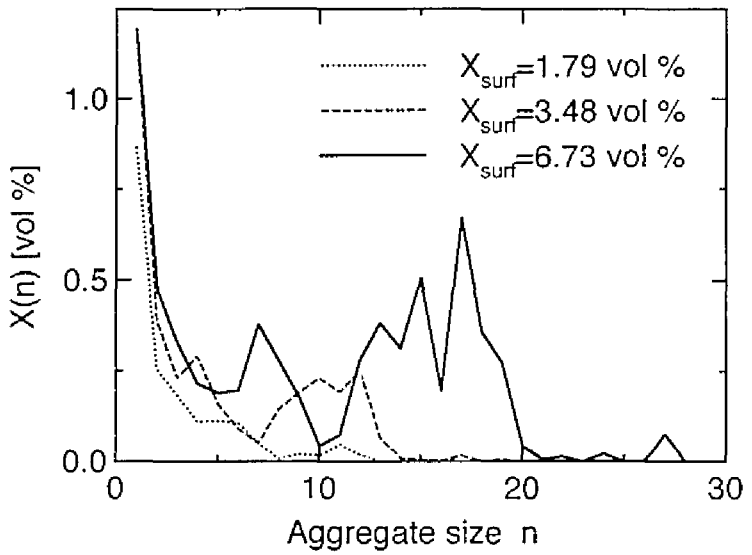

Figure 5.6. Size distributions of surfactant aggregates in System III at various values of X_{surf}. $X(n)$ denotes the volume fraction of surfactants in aggregates of size n. Dotted, dashed, and solid lines represent the distributions at X_{surf} = 1.79, 3.48, and 6.73 vol %, respectively. Each distribution is obtained by averaging over 150 configurations taken every 1,000th time step.

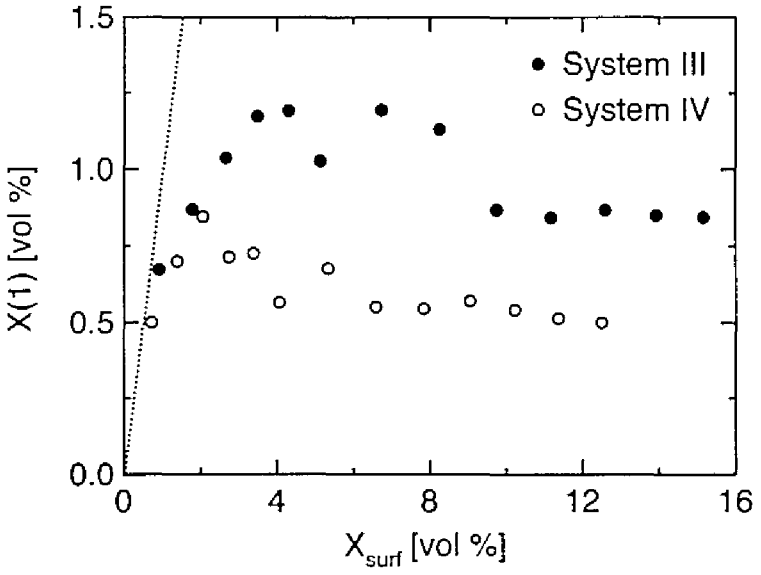

Figure 5.7. Free monomer concentration $X(1)$ as a function of the dosed surfactant concentration X_{surf}. Solid and open circles represent the plots for Systems III and IV, respectively. The dotted line indicates the relation of $X(1) = X_{surf}$. Each plot is obtained in the same way as in Figure 5.6.

at $T^* = 2.40$. Thereafter $X(1)$ starts to fall at the point of $X_{surf} \approx 9$ vol % and becomes nearly constant again. Similar behavior was reported in other studies and explained in the way that micelles interact with each other when X_{surf} is above the CMC [Brindle and Care, 1992; Desplat and Care, 1996]. This mechanism remains, however, to be examined more extensively.

The same features as described above appear in System IV and the CMC of an H_3Ht_3 surfactant solution at $T^* = 1.35$ is estimated to be about 2 vol %. In addition to the "ionic" surfactants of H_3Ht_5 and H_3Ht_3, "nonionic" surfactant solutions of h_2t_5 (see Table 5.1) are simulated separately. It is found that the CMC of the model nonionic surfactant solution is much lower than that of the model ionic surfactant solution. This agrees qualitatively with the behavior of real surfactant solutions.

All the above results confirm that the simple model used can capture, at least qualitatively, the characteristics of micellar solutions. Note that the temperature is kept at relatively high values following Smit and co-workers [1993b; Karaborni *et al.*, 1993, 1994], such that the surfactant solutions have typical aggregate size distributions and the CMC in the concentration ranges limited by the number of molecules.

5.4 Results and discussion

In Section 5.4.1, the aggregation of surfactants on the smooth hydrophilic wall is investigated using Systems V and VI listed in Table 5.2. The types of surfactants used are $H_3H't_5$ and $H_3H't_3$, which are different in tail length but the same in headgroup. Two values of the dosed surfactant concentration X_{surf} are chosen as given in Table 5.2. The results presented are obtained by the simulations using the initial configurations of Type I unless specified.

In Section 5.4.2, the surfactant aggregation on the hydrophobic wall is also examined using Systems VII and VIII.

5.4.1 Surfactant aggregation on hydrophilic walls

Micellar solutions between hydrophilic walls are examined mainly by graphic visualization of surfactants. At the end of this section, the mechanism of the adsorption and aggregation of surfactants is proposed and how the mechanism is influenced by the concentration and molecular structure of surfactants is discussed in detail.

1) $H_3H't_5$ solution of low concentration

Snapshot in the first stage. Figure 5.8 displays the snapshots of the $H_3H't_5$ surfactant solution of X_{surf} = 2.66 vol % between the hydrophilic walls. As expected, it is found that surfactants in the initial configurations neither aggregate anywhere nor adsorb on the surface. Figure 5.8(a) shows that some surfactants are adsorbed on the walls with their headgroups and tail chains pointing toward and away from the surface, respectively, at 1×10^4 time step. This is because the hydrophilic surface favors hydrophilic particles more than hydrophobic particles.

Snapshots in the middle stage. At 2.2×10^5 time step, surfactants form a small aggregate on the surface, which is referred to as the "2D-aggregate." One may suppose that an aggregate formed in the bulklike region adsorbs directly on the bare surface to construct the 2D-aggregate; this behavior is called the "direct aggregate adsorption." However, this 2D-aggregate formation hardly occurs during the simulation, which starts from the configurations of Type I.

To explore the surfactant aggregation on the surface extensively, the attention is focused on the surfactants in the rectangular box drawn in Figure 5.8(b) and their time evolutions are displayed in Figure 5.9. As shown in Figure 5.8(a), free monomers in the bulklike region adsorb at the unoccupied points of the surface;

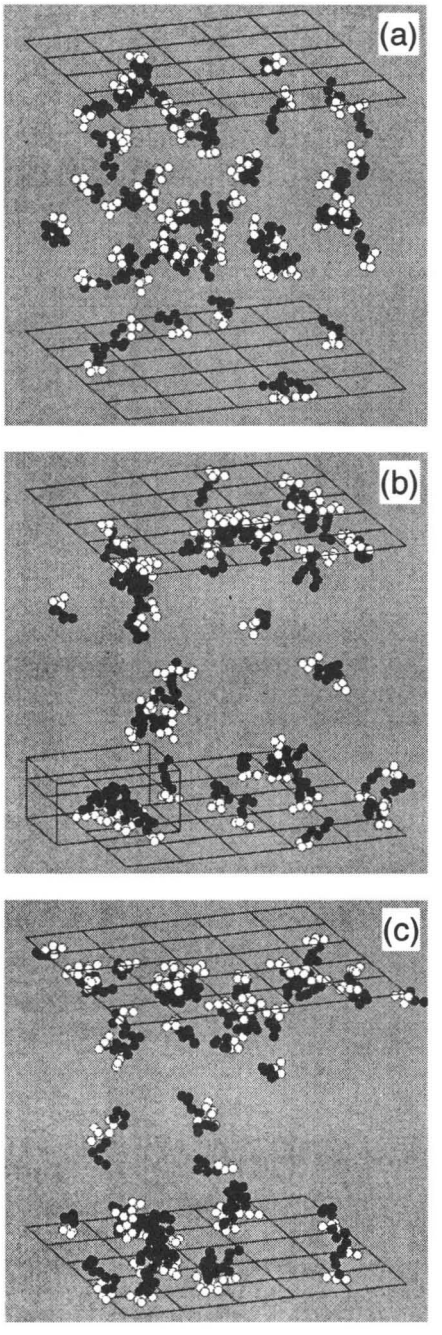

Figure 5.8. Snapshots of System V at X_{surf} = 2.66 vol %. White and black spheres display the headlike and taillike particles of surfactants, respectively, and two grid planes represent the walls. All solvent particles are not shown for clarity. (a) 1×10^4 time step; (b) 2.2×10^5 time step; (c) 3×10^5 time step.

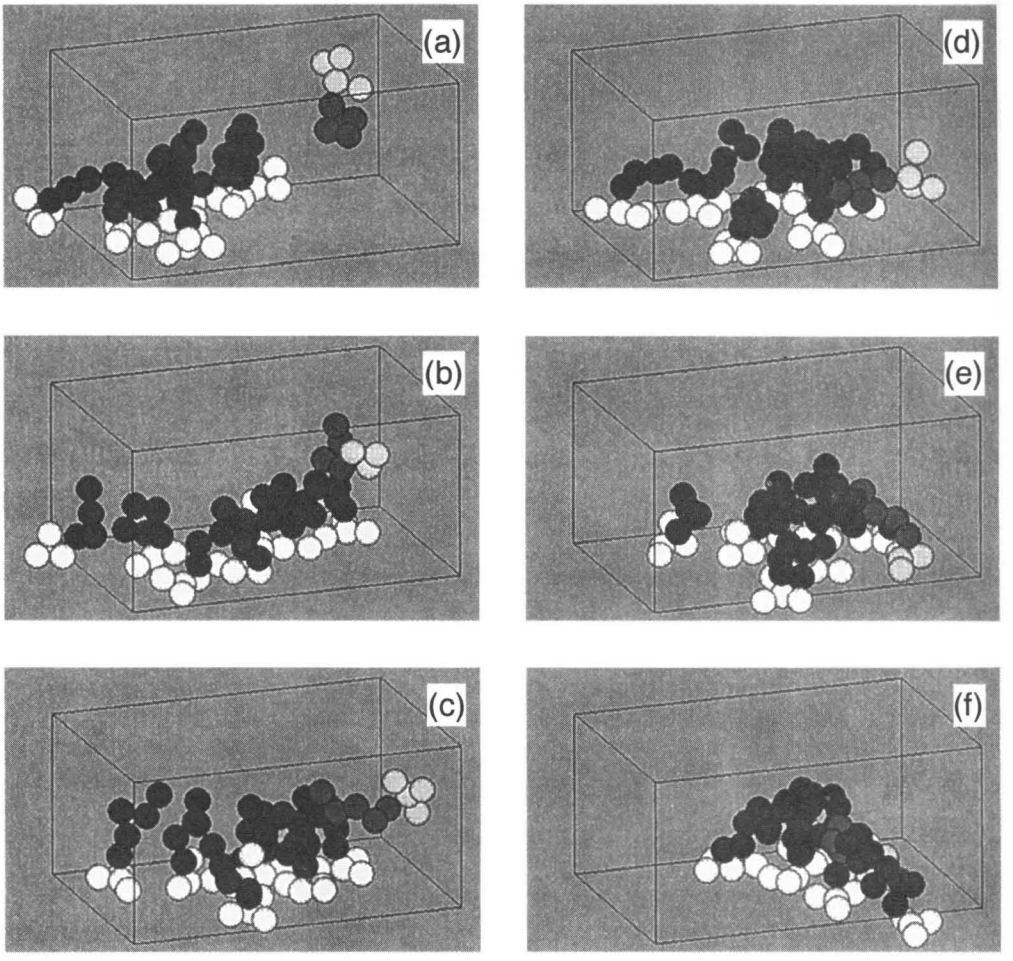

Figure 5.9. Time evolutions of the $H_3H'_{t_5}$ surfactants in the rectangular box shown in Figure 5.8(b). Notice the movement of the surfactant whose headlike and taillike particles are displayed by the light and dark gray spheres, respectively. (a) 2.05×10^5 time step; (b) 2.08×10^5 time step; (c) 2.13×10^5 time step; (d) 2.14×10^5 time step; (e) 2.16×10^5 time step; (f) 2.2×10^5 time step.

this is named the "direct monomer adsorption." In addition to that behavior, monomers frequently adsorb near the points occupied by the other surfactants because of the favorable tail–tail interactions; this is named the "tail-induced monomer adsorption." For example, as shown in Figures 5.9(a) and (b), a free monomer approaches the surfactant aggregate on the surface to make tail-to-tail contact. This surfactant moves around keeping the tail-to-tail contact during about 5×10^3 time steps, as shown in Figures 5.9(b)–(d). After that, the surfactant puts the head down to adsorb on the surface and consequently joins into the 2D-aggregate, as displayed in Figures 5.9(e) and (f).

Another point to observe in Figure 5.9 is that the small 2D-aggregates and the isolated surfactants fluctuate (or diffuse) transversely on the surface and assemble by the tail–tail attraction to grow into the larger 2D-aggregate shown in Figure 5.9(f); this behavior is called the "surface-diffusion growth."

Snapshot in the last stage. Figure 5.8(c) shows that after 3×10^5 time steps most of the surfactants adsorbed on the surface are incorporated into the 2D-aggregates. The 2D-aggregates diffuse laterally on the surface, assembling and splitting repeatedly. This indicates that they are not absolutely stable. Careful observation of snapshots manifests that surfactants migrate from one 2D-aggregate to another at the time scale of 1×10^4 steps.

Influence of initial configurations on the surfactant aggregation. The simulation is performed using the configurations of Type II. This shows that the 2D-aggregates are formed by the direct aggregate adsorption as well as by the tail-induced monomer adsorption and the surface-diffusion growth; the former mechanism is slower than the latter mechanisms. The reason why the aggregate adsorption hardly occurs in the simulation of Type I is probably because free monomers adsorb onto the surface rapidly before they aggregate in the bulklike region, as expected in Section 5.2.5.

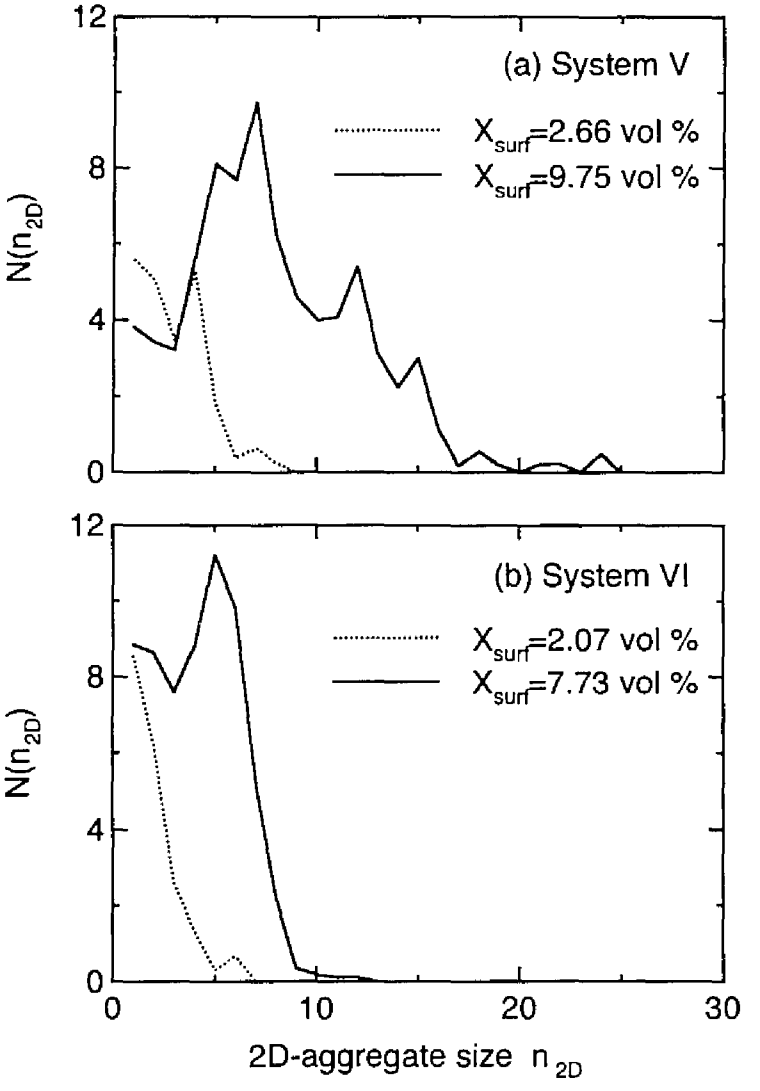

Figure 5.10. Size distribution of 2D-aggregates on the surface. $N(n_{2D})$ denotes the number of surfactants in 2D-aggregates of size n_{2D}. Dotted and solid lines indicate the distributions at low and high concentrations, respectively. (a) System V; (b) System VI. Each distribution is obtained by averaging over 50 configurations taken every 1,000th time step of the last 5×10^4 configurations.

Size distribution of 2D-aggregates. To quantify the 2D-aggregates in equilibrium, their size distribution is evaluated as shown in Figure 5.10. A surfactant molecule is regarded as adsorbed on the surface only when the distance between the H´ particle and the surface is less than $Z_{min} + 0.5d_S$. Then the 2D-aggregates are identified in the same way as described in Section 5.2.4. The interesting point to note is that the distribution has a minimum and a maximum. This behavior is found also in the size distribution of aggregates in the bulk, as shown in Figure 5.6. Similar results were reported by Wijmans and Linse [1997], where the adsorption of $h_{10}t_{10}$ surfactants at the hydrophobic interface was simulated by the lattice MC method.

2) $H_3H't_5$ solution of high concentration

Figure 5.11 displays the snapshots of the $H_3H't_5$ surfactant solution of X_{surf} = 9.75 vol %, which is higher than the last case of X_{surf} = 2.66 vol %. Figure 5.11(a) depicts the initial configurations of surfactants. At 1×10^4 time step, it is shown that some surfactants adsorb on the wall, some form micelles in the bulklike region, and the others are dissolved in the solvent as free monomers. After 3×10^5 time steps most surfactants are adsorbed on the wall to form 2D-aggregates, which are larger in size and located closer each other, compared with those at X_{surf} = 2.66 vol % shown in Figure 5.8(c). Figure 5.10(a) shows the influence of X_{surf} on the 2D-aggregate size quantitatively. The difference in size explains the observation that the 2D-aggregates at X_{surf} = 9.75 vol % fluctuate less on the surface, that is, are more stable compared with those at X_{surf} = 2.66 vol %.

Careful observation manifests that the 2D-aggregates are formed by the tail-induced monomer adsorption, the surface-diffusion growth, and the *indirect* aggregate adsorption that differs from the direct aggregate adsorption as follows. An aggregate, which is formed in the bulklike region, remains fluctuating without adsorbing directly onto the bare area during 5×10^3 to 1×10^4 time steps, because

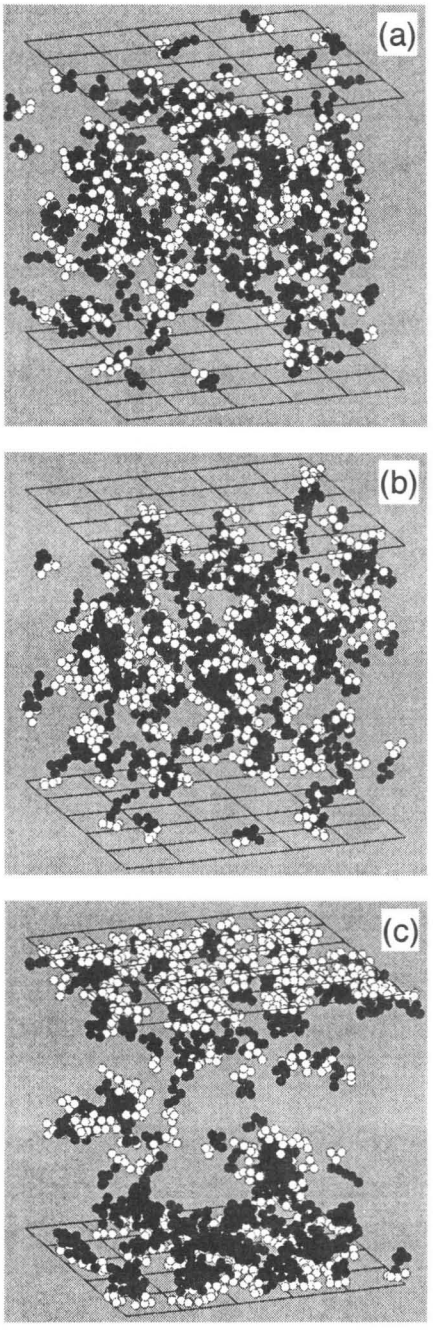

Figure 5.11. Snapshots of System V at X_{surf} = 9.75 vol %. Symbols are the same as in Figure 5.8. (a) 0 time step; (b) 1×10^4 time step; (c) 3×10^5 time step.

the surface has been already occupied by surfactants in parts. Then a few surfactants are pulled out of the aggregate to join the 2D-aggregate on the surface because of the tail–tail attraction; after fluctuating for a while, they adsorb completely on the surface. The rest of the broken aggregate return to the bulklike region because of steric repulsion. This adsorption is named the "tail-induced aggregate adsorption." This behavior of an aggregate is, however, hardly found in the simulations at the lower concentration of $X_{surf} = 2.66$ vol %.

3) $H_3H't_3$ solutions of low and high concentrations

The aggregation of $H_3H't_3$ surfactants with a shorter hydrophobic tail than $H_3H't_5$ is examined at $X_{surf} = 2.07$ and 7.73 vol %. Figure 5.12 shows the snapshots of the surfactant solutions after 3×10^5 time steps. Figures 5.10(b) and 5.12 suggest that the total number of surfactants on the surface and the size of 2D-aggregates increase as the dosed surfactant concentration is higher. Comparison between Figures 5.10(a) and (b) indicates that the larger 2D-aggregates are formed as the surfactant tail is longer. This characteristic is also observable when one make a comparison between Figures 5.8(c) and 5.12(a) and between Figures 5.11(c) and 5.12(b). Inspection of snapshots suggests that the 2D-aggregates of $H_3H't_3$ surfactants fluctuate assembling and splitting much more actively than those of $H_3H't_5$ surfactants, although the $H_3H't_3$ solutions are lower in temperature than the $H_3H't_5$ solutions. The decreases in size and stability of the $H_3H't_3$ aggregates are explained by the weaker attraction between the short tails. Mechanisms of the adsorption and aggregation are almost the same in both the cases of $H_3H't_3$ and $H_3H't_5$ surfactants at each concentration.

4) Mechanisms of adsorption and aggregation of surfactants on the hydrophilic surface

Five mechanisms. On the basis of the present simulations, five mechanisms of surfactant adsorption and aggregation on the hydrophilic surface are proposed

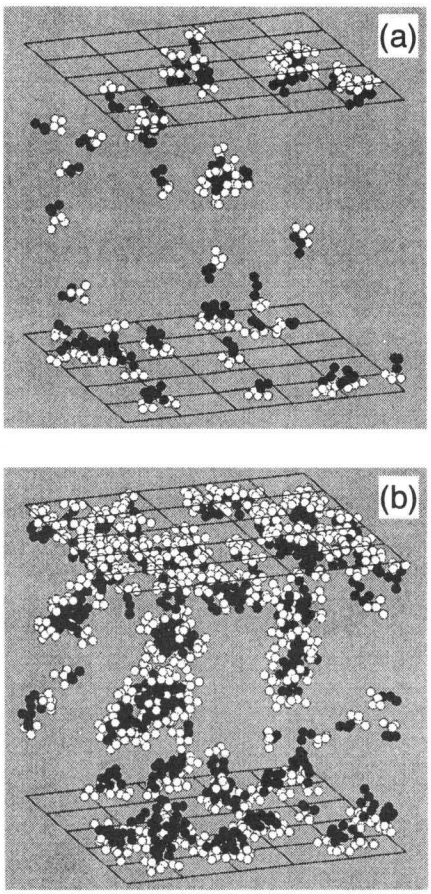

Figure 5.12. Final snapshots of System VI after 3×10^5 time steps. Symbols are the same as in Figure 5.8. (a) $X_{surf} = 2.07$ vol %; (b) $X_{surf} = 7.73$ vol %.

as illustrated in Figure 5.13, where the frequency of appearance of the mechanisms decreases from panels (a) to (e). The two mechanisms in Figures 5.13(a) and (e) are promoted by the strong head–surface interactions, while the rest in Figures 5.13(b)–(d) are induced by the favorable tail–tail interactions. Hence, the latter three mechanisms are more frequent as the surfactant tail is longer. The author emphasizes that the two mechanisms shown in Figures 5.13(b) and (c) are dominant in the surfactant aggregation on the surface and those in Figures 5.13(d) and (e) are secondary. The latter two are still less frequent as the surfactant concentration is lower, because the surfactants hardly aggregate in the bulk. As the number of surfactants adsorbed on the surface increases, the direct adsorption of monomers and aggregates shown in Figures 5.13(a) and (e) is less frequent.

Aggregation in the bulk and at the interface. Finally, it is considered why the islandlike aggregates were observed in AFM measurements even though the concentration of dosed surfactants was much below the CMC [Fukuda, 1996]. Figures 5.6 and 5.10(a) show that at the low concentration of about 3 vol % (≈ CMC), the size distribution of $H_3H't_5$ aggregates on the surface has a peak at n_{2D} = 4, while the corresponding peak is absent in the bulk. In the case of the $H_3H't_3$ solutions near the CMC, the size distributions have peaks neither on the surface nor in the bulk, as shown in Figure 5.10(b). These indicate that the solid/liquid interface is as favorable as the bulk for the $H_3H't_3$ aggregation, whereas the interface is more favorable for the $H_3H't_5$ aggregation. Hence, this demonstrates that the interface becomes more favorable for the surfactant aggregation than the bulk as the surfactant tail is longer. Supposing that a surfactant has a longer tail than the surfactants used here, the aggregation can occur at the interface even when the dosed surfactant concentration is well below the CMC.

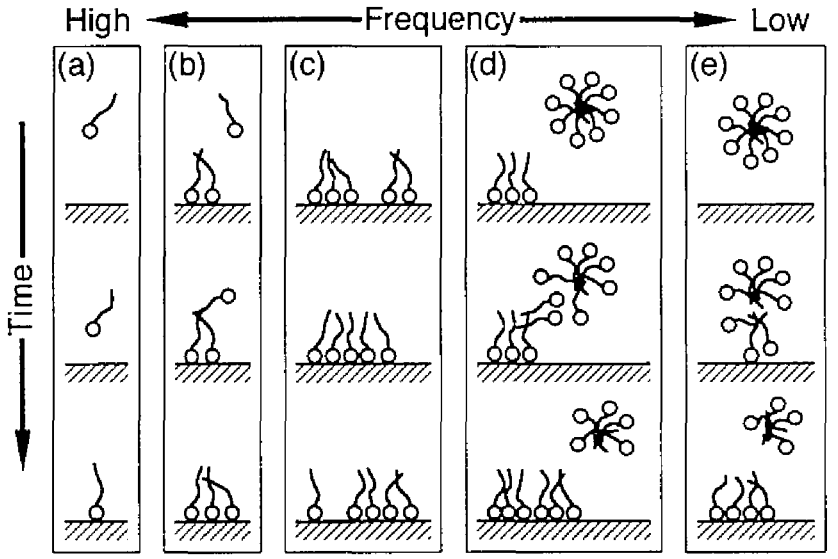

Figure 5.13. Mechanisms of the adsorption and aggregation of surfactants on the hydrophilic surface. (a) Direct monomer adsorption; (b) tail-induced monomer adsorption; (c) surface-diffusion growth; (d) tail-induced aggregate adsorption; (e) direct aggregate adsorption. The frequency of appearance of the five mechanisms decreases from panels (a) to (e).

5.4.2 Surfactant aggregation on hydrophobic walls

The simulations are performed using Systems VII and VIII, which are the same systems as employed in Section 5.4.1, but the wall used here is hydrophobic. Figures 5.14 and 5.15 display the snapshots of final configurations of Systems VII and VIII, respectively. It is shown that surfactants are adsorbed on the wall, laying down their tail chains on the surface and keeping their headgroups away from the surface. In contrast to this *lying* adsorption of surfactants, the *standing* adsorption is observed at the hydrophilic surface as shown in Figure 5.9.

5.5 Concluding remarks

In this chapter, the simple description of water, oil, and surfactant molecules is given and applied also to the molecule–wall interactions. Using this simple model, MD simulations of water/solid interfaces and micellar solutions are performed. The results are compared with those by the atomistic model simulations, presented in Chapters 2 and 3 and other studies. This demonstrates that the simple model can capture the basic characteristics of water/solid interfaces and micellar solutions.

Thereafter, the surfactant aggregation on the hydrophilic and hydrophobic surfaces in micellar solutions is investigated in detail. This study is the first to give the possible mechanisms of interfacial aggregation of surfactants, which have never been expected and can not be investigated by the atomistic simulation because of the lack of computational power.

Thus, the simple model simulation is a powerful tool to reveal the physics underlying in surfactant solutions. This simulation method can be applied also to larger and more complex systems, which include surfactants, polymers, and macroscopic colloidal particles, as is described in next two chapters.

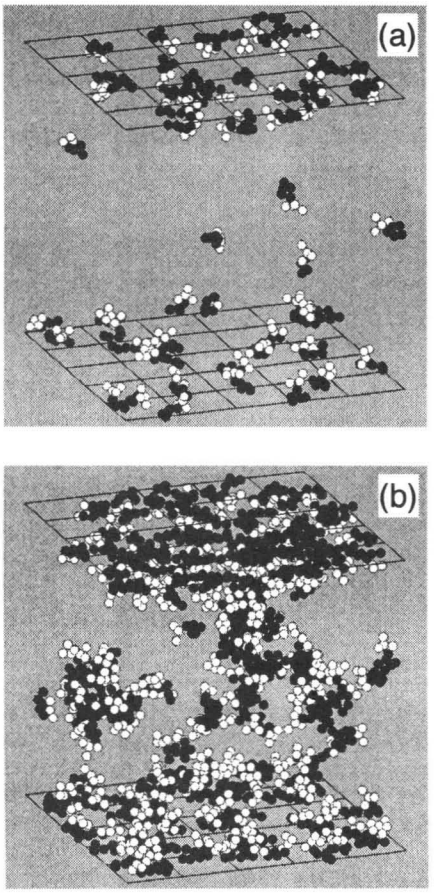

Figure 5.14. Final snapshots of System VII after 3×10^5 time steps. Symbols are the same as in Figure 5.8. (a) $X_{surf} = 2.66$ vol %; (b) $X_{surf} = 9.75$ vol %.

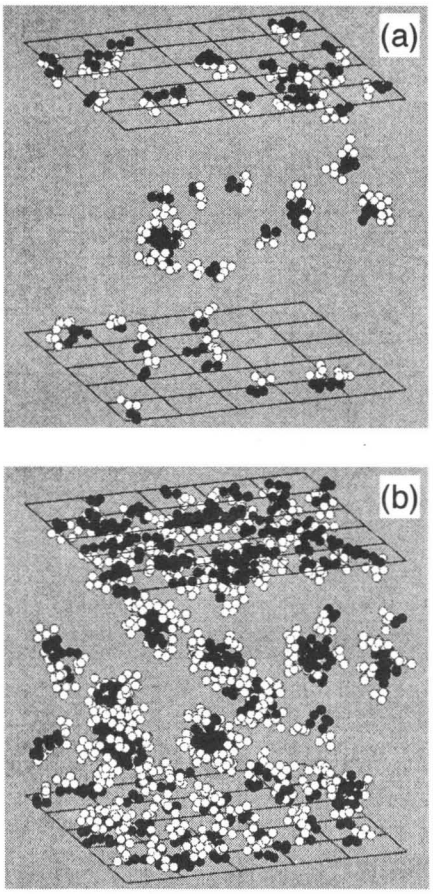

Figure 5.15. Final snapshots of System VIII after 3×10^5 time steps. Symbols are the same as in Figure 5.8. (a) X_{surf} = 2.07 vol %; (b) X_{surf} = 7.73 vol %.

Part III

Interaction Forces between Colloidal Particles in Fluids

6
Surface Forces in Simple Fluids

6.1 Introduction

This chapter presents a new method to evaluate the interaction forces between two large spheres in a fluid using MD simulations. This method is applied to the system shown in Figure 6.1, in which a pair of spherical structureless macroparticles is immersed in a pure simple fluid. The results are compared with those by other simulations using the grand canonical ensemble (GCE) and by the integral equation theory (IET).

A large system is required to allow solvent particles to locate between the macroparticles and exchange themselves with those in the bulk reservoir. This indicates that the present method consumes much computation time. However, this method has the following advantages over the GCE simulation and the IET:

(i) A spherical surface can be introduced in this method, which is more realistic than a planar wall commonly used in the GCE simulation.

(ii) Detailed features of a fluid film between surfaces are obtained.

(iii) The phase separation of the fluid film and the interface between the phases can be expressed without any artifact if occur; for example, condensation, evaporation, and bridging of liquid and vapor.

(iv) This method is easily extended to investigate the surface forces in a mixture and a complex fluid.

How robust this method is will turn out clearly in next chapter, where the fluid

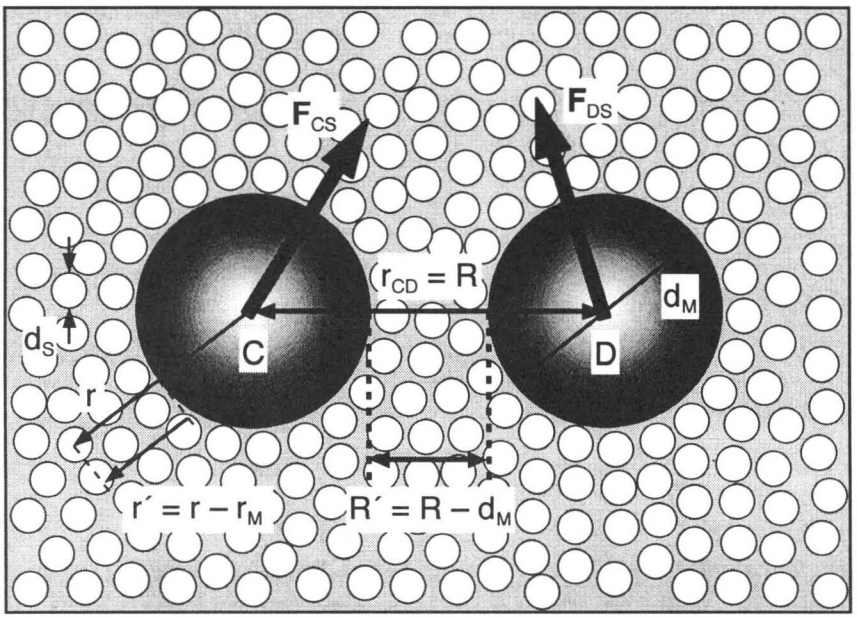

Figure 6.1. Illustration of the basic cell including two macroparticles and a large number of solvent particles. The cell is depicted two-dimensionally for clarity.

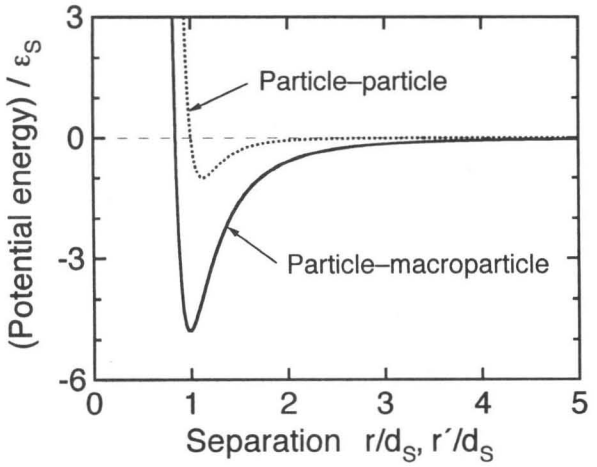

Figure 6.2. Potential energies for particle–particle and particle–macroparticle interactions represented by Equations (6.1b) and (6.2b), respectively. r' indicates the distance from the macroparticle surface, $r - r_M$, as shown in Figure 6.1.

employed is mixed and complex.

6.2 Molecular models

6.2.1 Simple fluids

The interaction between solvent particles is represented in the same way as described in Section 5.2.1:

$$u_{SS}(r) = \begin{cases} \phi(r) - \phi(R_{SS}^{cut}), & r \le R_{SS}^{cut}, \\ 0, & r > R_{SS}^{cut}, \end{cases} \tag{6.1a}$$

$$\phi(r) = 4\varepsilon_S \left[\left(\frac{d_S}{r} \right)^{12} - \left(\frac{d_S}{r} \right)^{6} \right]. \tag{6.1b}$$

Two types of fluids are employed:

(i) A Lennard-Jones (LJ) fluid of $R_{SS}^{cut} = 2.5d_S$, where the interparticle interaction includes the repulsive and attractive forces.

(ii) A soft-sphere (SS) fluid of $R_{SS}^{cut} = 2^{1/6}d_S$, where the interaction includes the short-range repulsion only.

The thermodynamic state of the fluid is chosen to be identical to that used in other simulations [Snook and van Megen, 1980; Magda *et al.*, 1985] and the IET studies [Kjellander and Sarman, 1990, 1991; Sarman, 1990; Kinoshita *et. al.*, 1996b]; that is, $\rho^* = \rho d_S^3 = 0.5925$ and $T^* = k_B T/\varepsilon_S = 1.2$. This is because the simulation data can be easily compared with the results by these studies.

6.2.2 Solvophilic and solvophobic macroparticles

The shifted (10–4–3) potential is used for particle–macroparticle interaction [Steele, 1973]:

TABLE 6.1: Systems of constrained MD simulations

System	Fluid [a]	Macroparticle pair	Diameter d_M	Box length L
I	Soft-sphere	Solvophobic	$10d_S$, $20d_S$	$56.8d_S$, $57.6d_S$
II	Lennard-Jones particle	Solvophobic	$10d_S$	$56.8d_S$
III	Soft-sphere	Solvophilic	$10d_S$	$56.8d_S$
IV	Lennard-Jones particle	Solvophilic	$10d_S$	$56.8d_S$

[a] The total number of particles N is 108,000 and the thermodynamic state is $\rho^* = \rho d_S^3 = 0.5925$ and $T^* = k_B T/\varepsilon_S = 1.2$.

$$u_{MS}(r) = \begin{cases} \infty, & r \le r_M, \\ \psi(r) - \psi(R_{MS}^{cut}), & r_M < r \le r_M + R_{MS}^{cut}, \\ 0, & r > r_M + R_{MS}^{cut}, \end{cases} \tag{6.2a}$$

$$\psi(r) = 2\pi\varepsilon_S \left[\frac{2}{5}\left(\frac{d_S}{r - r_M}\right)^{10} - \left(\frac{d_S}{r - r_M}\right)^4 - \frac{d_S^4}{3\Delta r(r - r_M + 0.61\Delta r)^3} \right], \tag{6.2b}$$

$$r_M = d_M/2, \quad \Delta r = d_S/\sqrt{2}, \tag{6.2c}$$

where d_M is the diameter of the macroparticle and R_{MS}^{cut} is the cutoff distance. Note that the center of the outermost atoms in the macroparticle is located at separation r_M from the center of the macroparticle. The particle–macroparticle potential shown in Figure 6.2 is almost the same as the potential for particle–wall interaction shown in Figure 5.3. The mass of the macroparticle m_M is equal to $m_S(d_M/d_S)^3$, where m_S is the mass of the solvent particle.

Two types of macroparticles of $d_M = 10d_S$ (or $20d_S$) are considered:

(i) A solvophilic macroparticle of $R_{MS}^{cut} = 10d_S$, where the particle–macroparticle interaction includes the repulsion and attraction.

(ii) A solvophobic macroparticle of $R_{MS}^{cut} = 0.987d_S$, where the particle–macroparticle interaction includes the short-range repulsion only.

6.2.3 Systems

In this study, four systems are employed as listed in Table 6.1; a pair of solvophobic macroparticles in SS and LJ fluids (Systems I and II) and a pair of solvophilic macroparticles in SS and LJ fluids (Systems III and IV).

6.3 Constrained molecular dynamics method

6.3.1 Description of interactions between macroparticles

A system composed of two macroparticles (C and D) and N solvent particles is considered, as illustrated in Figure 6.1. MD simulations of the system are performed keeping the center-to-center separation between the macroparticles. For this purpose, the following constraint on the macroparticles is incorporated into the equations of motion:

$$\xi(\mathbf{r}_C, \mathbf{r}_D) = |\mathbf{r}_C - \mathbf{r}_D|^2 - R^2 = 0, \tag{6.3}$$

where R is the fixed separation between macroparticles C and D. This method was employed for the first time to evaluate the mean force potential of an ion pair in a polar solvent [Ciccotti *et al.*, 1989].

The forces on macroparticles C and D caused by the solvent particles, $\mathbf{F}_{CS}$ and $\mathbf{F}_{DS}$, are calculated during each simulation. The solvent contribution to the interaction force between the macroparticles, that is, the solvation force $F^{solv}(R)$ is evaluated as a time average using the following expression:

$$F^{solv}(R) = \frac{1}{2}\langle \mathbf{u}_{CD} \cdot (\mathbf{F}_{CS} - \mathbf{F}_{DS}) \rangle, \tag{6.4a}$$

$$\mathbf{u}_{CD} = (\mathbf{r}_C - \mathbf{r}_D) / |\mathbf{r}_C - \mathbf{r}_D|. \tag{6.4b}$$

The potential $W^{solv}(R)$ can be obtained by integrating Equation (6.4a) from the

large separation R_0 to a given separation R,

$$W^{solv}(R) = -\int_{R_0}^{R} F^{solv}(R)\,dR. \tag{6.5}$$

Supposing that the macroparticle is uniformly composed of the LJ particles of the number density $\rho d_S^3 = 1.0$ and only the attraction term of $-(4\varepsilon_S d_S^6)/r^6$ in Equation (6.1b) is considered, the potential of the direct macroparticle–macroparticle interaction, $W^{dir}(R)$, is given by the analytical formula [Hamaker, 1937]:

$$W^{dir}(R) = -\frac{A}{6}\left[\frac{2}{s^2-4} + \frac{2}{s^2} + \ln\left(\frac{s^2-4}{s^2}\right)\right], \tag{6.6a}$$

$$s = \frac{2(R-d_M)}{d_S} \Big/ \left(\frac{d_M}{d_S}\right) + 2, \tag{6.6b}$$

$$A = \pi^2\rho^2(4\varepsilon_S d_S^6) = 4\pi^2\varepsilon_S, \tag{6.6c}$$

where A is the Hamaker constant. The force $F^{dir}(R)$ is obtained by differentiating Equation (6.6a),

$$F^{dir}(R) = -\frac{dW^{dir}(R)}{dR} = -\frac{64A}{3d_M}\frac{1}{s^3(s^2-4)^2}. \tag{6.7}$$

Consequently, the total mean force between the macroparticles $F^{tot}(R)$ and the potential $W^{tot}(R)$ are described as

$$F^{tot}(R) = F^{solv}(R) + F^{dir}(R), \tag{6.8}$$

$$W^{tot}(R) = W^{solv}(R) + W^{dir}(R). \tag{6.9}$$

In this chapter, the above method is applied to the short-range potential systems as in Table 6.1. However, the present method is applicable also to long-range potential systems (e.g., Coulomb systems) if needed.

6.3.2 Simulation details

Simulations are performed in a system composed of two macroparticles of d_M = $10d_S$ (or $20d_S$) and N = 108,000 solvent particles in a cubic cell with periodic boundaries. The length of the cell is selected to be $56.8d_S$ (or $57.6d_S$) such that the density of the bulk fluid ρ^* is 0.5925. It is confirmed that the basic cell has enough dimensions to be unaffected by the neighboring image cells. The constraint on macroparticles C and D by Equation (6.3) is imposed using the SHAKE method [Ryckaert *et al.*, 1977]. The equations of motion for the solvent particles and the constrained macroparticles are solved using the leap-frog algorithm with a time step of $\Delta t = 0.00464\tau_0$, where $\tau_0 = d_S(m_S/\varepsilon_S)^{1/2}$. The temperature of the solvent is kept at T^* = 1.2 using the Berendsen's external bath method with a time constant of $\tau_T = 0.464\tau_0$ [Berendsen *et al.*, 1984], while no temperature-control procedure is incorporated into the macroparticles except the separation constraint. This is because it is favorable in the calculation of the solvation force to use as few artificial procedures as possible, which are imposed on the macroparticles. The force calculation algorithm is the same as explained in Section 5.2.5.

The nearest separation between the macroparticles, $R - d_M$ (= R'), ranges from $1.0d_S$ to $5.0d_S$ with increments of $0.1d_S$ and $0.2d_S$. In each system, a series of constrained MD simulations are performed as follows:

(i) Two macroparticles of C and D are positioned on a diagonal line of the cell such that the C–D separation is the largest separation of R' = $5.0d_S$. 108,000 solvent particles are placed at the face-centered-cubic (fcc) lattice points excluding the macroparticles' space.

(ii) The system is equilibrated over 5.5×10^4 time steps.

(iii) The instantaneous forces of $\mathbf{F}_{CS}$ and $\mathbf{F}_{DS}$ are computed during 2×10^4 time steps to obtain the solvation force $F^{solv}(R)$ using Equation (6.4).

(iv) Then, external forces are assigned to the macroparticles along the C–D line for

5×10^3 time steps to reduce the C–D separation by $0.1d_S$ or $0.2d_S$.

(v) For equilibration of the solvent particles around the macroparticles, the system is allowed to evolve for another 5×10^3 time steps, keeping the new C–D separation.

Repeating the procedure from (iii) to (v), one can obtain the force–distance profile. The statistical errors of the solvation forces are evaluated by the block averaging method [Flyvbjerg and Petersen, 1989] and found to be less than ±2.0, ±1.4, ±2.8, and ±2.5 (in unit of k_BT/d_S) for Systems I–IV, respectively. The potential $W^{solv}(R)$ is calculated by integrating the values of $F^{solv}(R)$, where the trapezoidal rule is used without any smoothing procedure.

6.4 Results and discussion

In the following sections, Systems I–IV are investigated mainly in terms of the solvent density profile near the macroparticle surface (g_{MS}), the solvation force (F^{solv}), and the potential (W^{solv}). This is because the direct macroparticle–macroparticle interaction given by Equation (6.7) is not significant compared with the solvation force in the present systems.

6.4.1 Influence of macroparticle diameter on solvation force

How the macroparticle diameter d_M affects the solvation force is examined comparing the results for $d_M = 10d_S$ and $20d_S$ in System I. The solvation force profiles are given in Figure 6.3, where the positive and negative values mean the repulsive and attractive forces, respectively. Figure 6.3(a) indicates that the force–distance profiles are qualitatively similar although the amplitude of the oscillatory behavior is larger in the case of $d_M = 20d_S$. However, after both the profiles are

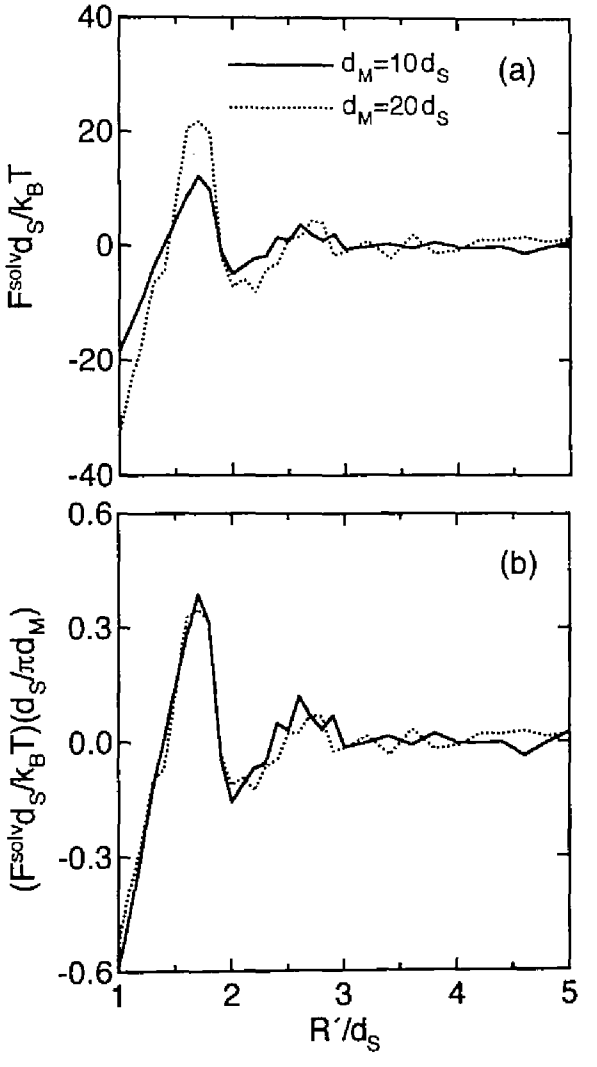

Figure 6.3. (a) Solvation force in System I (see Table 6.1). (b) Force normalized by the Derjaguin approximation (see the text), which is corresponding to panel (a). Solid and dotted lines represent the forces for $d_M = 10d_S$ and $20d_S$, respectively.

multiplied by the factor of $d_S/\pi d_M$ on the basis of the Derjaguin approximation [Derjaguin, 1934], they are almost identical to each other in all the range of the surface separations, as shown in Figure 6.3(b). Therefore, it is believed that the succeeding results of the solvation force obtained using $d_M = 10d_S$ give the quantitative behavior within the conditions employed in this study, if the force–distance profiles are normalized by the value of d_M.

6.4.2 Solvation forces between "solvophobic" macroparticles

A pair of solvophobic macroparticles immersed in SS and LJ fluids, that is, Systems I and II, are considered. Figures 6.4, 6.5, and 6.6 show the profiles of g_{MS}, F^{solv}, and W^{solv}, respectively.

1) System I—Oscillatory structural force

Figure 6.4 illustrates that the dense layers of solvent particles are formed adjacent to the surface of the large sphere even in such a soft-sphere system that particle–particle and particle–macroparticle interactions are repulsive in the short-range separations. This "packing efficiency" of particles near the surface results from the minimization of the free energy of the system, that is, the maximization of the entropy because the enthalpy hardly contributes in the soft-sphere system. It is emphasized that the packing efficiency which is entirely attributable to the entropy effect is, more or less, potentially intrinsic to any systems.

When these two surfaces approach each other, the solvation force and the potential oscillate around the zero value, exhibiting the attraction and repulsion, and their periodic distances are about solvent diameter d_S as shown in Figures 6.5 and 6.6. Hence, this oscillatory behavior is caused by the packing effect. After the solvent particles in the only one layer between the nearest surfaces of macroparticles are pushed out into the bulk at $R' < 1.9d_S$, the strong attraction acts between the macroparticles. Then the macroparticles come into contact with each

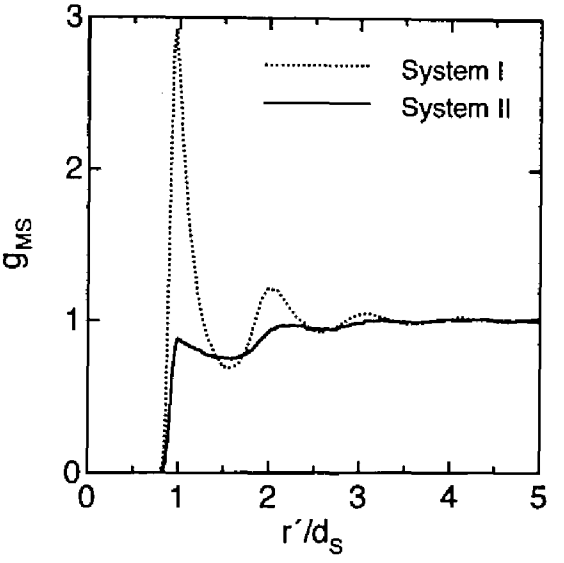

Figure 6.4. Reduced density profile of solvent particles near the surface of the solvophobic macroparticle of $d_M = 10d_S$. Dotted and solid lines represent the profiles for soft-sphere (SS) and Lennard-Jones (LJ) fluids, that is, Systems I and II, respectively.

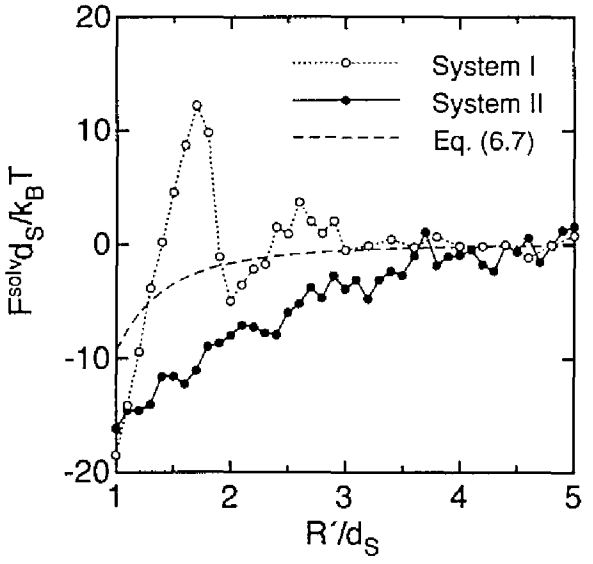

Figure 6.5. Solvation force between the solvophobic macroparticles of $d_M = 10d_S$ in a fluid. The dashed line shows Equation (6.7) and the rest are the same as in Figure 6.4.

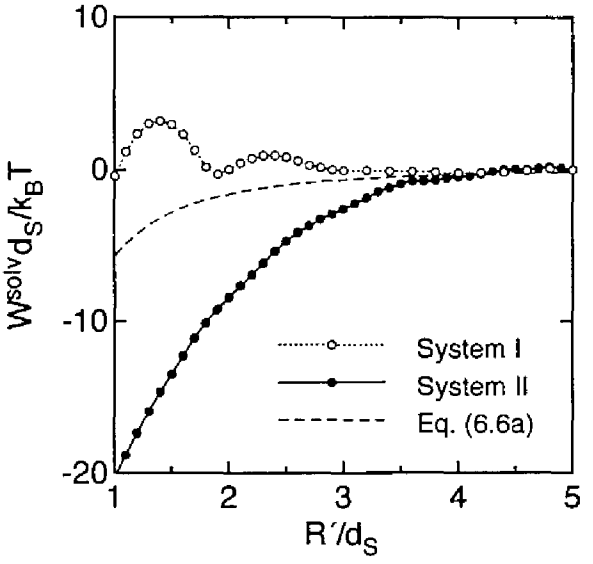

Figure 6.6. Potential of solvation force corresponding to Figure 6.5. The dashed line shows Equation (6.6a) and the rest are the same as in Figure 6.4.

other at $R' = 1.0d_s$, which is the most stable state with regard to the free energy as expected from Figure 6.6.

The above behavior is explained by the following mechanism. In System I where the enthalpy is negligible, the behavior of the solvent particles shown in Figure 6.4 are most favorable for the total entropy of such a system that a single macroparticle exists in the solvent. Nonetheless, the solvent particles in the dense layers near the macroparticle surface are less advantageous in terms of the entropy than those in the bulk. Hence, if two macroparticles attach to each other, the solvent particles are pushed out into the bulk, which leads to the increase of the overall entropy of the system, that is, the decrease of the free energy. Thus the strong attractive force is induced even in a soft-sphere system such as System I.

These results were also derived from the IET studies on the similar systems: hard-spherical macroparticles are immersed in a hard-sphere fluid [Henderson, 1988; Kinoshita *et al.*, 1996a]. The force–distance profiles by the present simulation and theoretical studies coincide qualitatively with those by the SFA experiments: the interaction forces were measured between the molecularly smooth surfaces of a cleaved mica in the liquid of quasi-spherical nonpolar molecules such as octamethylcyclotetrasiloxane (OMCTS), tetrachloromethane, cyclohexane, and benzene [Horn and Israelachvili, 1981; Christenson, 1983, 1986; Israelachvili, 1987, 1991].

2) System II—Solvophobic attraction

In this system, the attraction is present for solvent–solvent interaction, but absent for solvent–macroparticle interaction. Figures 6.4, 6.5, and 6.6 show that no dense layer of the solvent particles is formed near the surface (i.e., the "dewetting") and the solvation force profile exhibits the strong attraction without oscillating (i.e., the "solvophobic attraction"). This behavior is different from that in System I.

The similar results have been also reported in the other studies [Bérard, 1993; Kinoshita *et al.*, 1996b] and are interpreted as follows. When a large solvophobic macroparticle intrudes into an attractive potential fluid, favorable bonds between the solvent particles are disrupted. Accordingly the particles near the macroparticle surface are reorganized at the sacrifice of the packing efficiency such that the bonds are broken as few as possible, which leads to the dewetting in this case. This behavior is advantageous to the bonds, that is, the enthalpy but disadvantageous to the packing efficiency, that is, the entropy. These contradictory contributions are compromised to minimize the free energy. Nevertheless, the solvent particles near the surface are too unstable to form any dense layer. If the surfaces approach each other, these unstable particles are pushed out into the bulk, by which the free energy of the system decreases. Thus the strong and monotonous attraction is generated between solvophobic surfaces in an attractive potential fluid.

Figure 6.5 shows that the attraction caused by the solvent is stronger than the direct macroparticle–macroparticle interaction given by Equation (6.7) in all the separation ranges.

6.4.3 Solvation forces between "solvophilic" macroparticles

A pair of solvophilic macroparticles immersed in SS and LJ fluids, that is, Systems III and IV, are considered and the results are shown in Figures 6.7, 6.8, and 6.9. It is worth noting that the results for Systems III and IV are almost the same independent of the fluids employed: SS and LJ fluids. Comparison between Figure 6.4 for System I and Figure 6.7 for Systems III and IV indicates that the solvent density is higher near the solvophilic surface, though the behavior of these density profiles is qualitatively similar.

Figure 6.8 shows that the solvation forces oscillate with the periodicity of

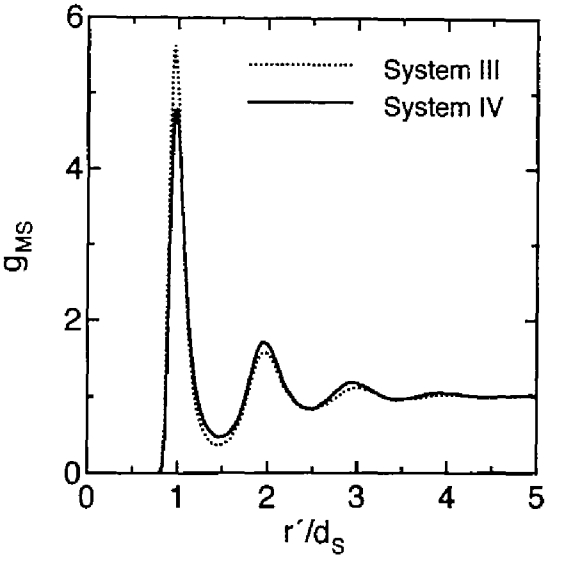

Figure 6.7. Reduced density profile of solvent particles near the surface of the solvophilic macroparticle of $d_M = 10d_S$. Dotted and solid lines represent the profiles for soft-sphere (SS) and Lennard-Jones (LJ) fluids, that is, Systems III and IV, respectively.

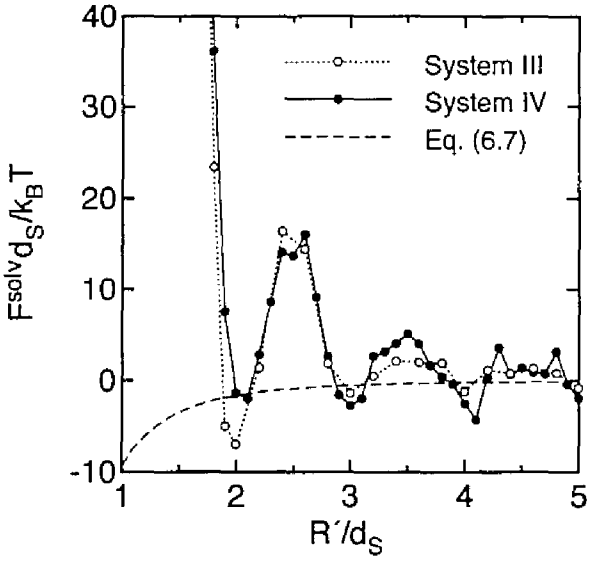

Figure 6.8. Solvation force between the solvophilic macroparticles of $d_M = 10d_S$ in a fluid. The dashed line shows Equation (6.7) and the rest are the same as in Figure 6.7.

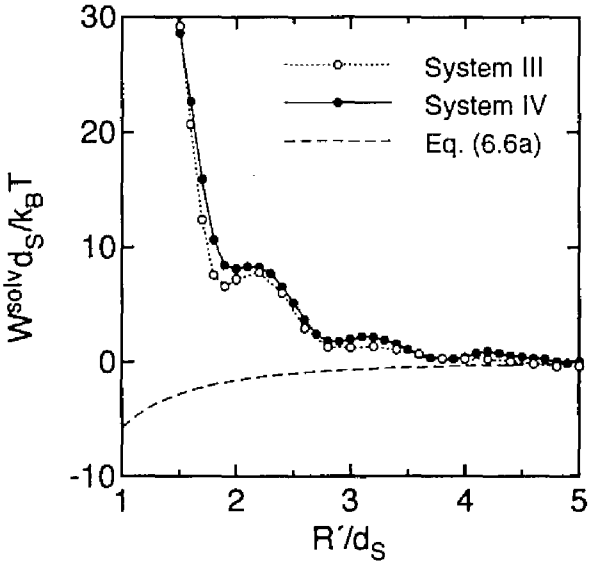

Figure 6.9. Potential of solvation force corresponding to Figure 6.8. The dashed line shows Equation (6.6a) and the rest are the same as in Figure 6.7.

about d_S because of the packing effect and are steeply repulsive in the short range of $R' < 1.9d_S$, where a layer of solvent particles between the surfaces are pushed out into the bulk. This repulsion is even stronger than the attraction F^{dir} given by Equation (6.7). The potentials of W^{solv} shown in Figure 6.9 suggest that the net solvation forces are repulsive from the viewpoint of free energy and the surfaces prefer being separated from each other with interposing more than two layers of solvent particles. This behavior is attributable to a strong affinity of the macroparticle for solvent.

The above results for System IV agree well with those by the other studies [Snook and van Megen, 1980; Magda *et al.*, 1985; Kjellander and Sarman, 1990, 1991; Sarman, 1990; Kinoshita *et al.*, 1996b]. It is worth noting that the sign of solvation forces at the small separation for Systems III and IV is opposite from that for System I as shown in Figures 6.5 and 6.8, although their solvent density profiles are the same qualitatively as described above. This discrepancy arises from the difference in the solvent affinity between the solvophilic and solvophobic macroparticles.

6.5 Concluding remarks

In this chapter, the author first provides the computational technique to evaluate the interaction force between large spheres in a fluid using MD simulations. This method is applied to the relatively simple systems, in which a pair of spherical structureless macroparticles, either solvophobic or solvophilic, is immersed in a fluid of two types: an SS or an LJ fluid. The results agree well with those by the other simulation and theoretical studies with respect to the solvent density profile near the macroparticle surface and the solvation force profile between the surfaces.

The present simulation method requires much computation time compared with the other methods, because a large system is indispensable to allow solvent particles to locate between the macroparticles and exchange themselves with those in the bulk reservoir. As demonstrated in Chapter 7, however, this technique can be easily extended to simulate the systems of the large spheres immersed in a mixture and a complex fluid, to which the GCE simulations are hardly applicable. In the near future, the present method will be extended to simulate long-range potential systems with the advance of computational power.

7
Surface Forces in Complex Fluids

7.1 Introduction

The previous two chapters gave the simple description of water, oil, and surfactant molecules and macroscopic colloidal particles (Chapter 5), and the computational method to evaluate the interaction force between the colloidal particles in a fluid (Chapter 6). A combination of these molecular model and evaluation method enables us to calculate the surface force in a complex fluid composed of water, oil, surfactants, and polymers.

Recently, Kanda *et al.* [1998] measured the interaction forces between negatively charged surfaces in water–alcohol (methanol, ethanol, and *n*-propanol) mixtures using the atomic force microscopy (AFM) and reported as follows:

(i) The force–distanse profile is steplike in the short range of the surface separation when the alcohol weight fraction w_{alc} is greater than 0.9. This steplike behavior will be attributable to the vertical adsorption of alcohol molecules on the surface, as shown in Figure 7.1(a).

(ii) The adhesion force exhibits the strong attraction at $w_{alc} \approx 0.9$. The magnitude of this attraction increases with increasing molecular weight of alcohol. The strong attraction originates possibly in the water bridging between the surfaces, as shown in Figure 7.1(b).

These experimental results are very interesting, but insufficient and indirect to support the mechanisms proposed in Figure 7.1.

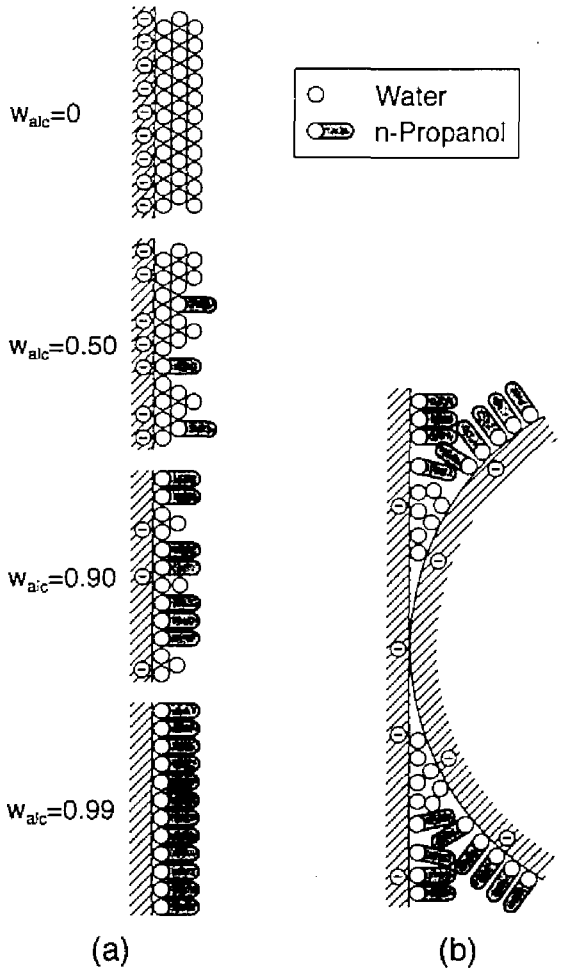

Figure 7.1. Schematic drawing of the structure of molecules adsorbed on the interface in alcohol–water solutions, after Kanda *et al.* [1998]. (a) The change of the structure of the adsorbed layer with alcohol concentration. (b) The proposed model for the attractive force at w_{alc} = 0.9, which is caused by the water bridging between surfaces in the alcohol-rich medium.

The aim of this chapter is to elucidate the origin of the strong adhesion force between the hydrophilic surfaces in alcohol–water mixtures. Using the above simulation method, the author investigates systematically the interaction forces between smooth hydrophilic macroparticles in alcohol–water mixtures and presents the following results:

(i) Structure of the solution near the macroparticle surface.

(ii) Force–distance profile between the macroparticles.

(iii) Adhesion force as a function of the alcohol concentration.

These simulation results are discussed in detail and compared with the experimental results by AFM [Kanda *et al.*, 1998]. The author emphasizes that application of the simulation method employed is not restricted to the present system.

7.2 Molecular models

7.2.1 Alcohol–water mixtures

The simple models of water and alcohol molecules are illustrated in Figure 7.2: a water molecule is represented by one w particle; and two types of amphiphiles are represented by ht and ht_3, which are different in hydrophobic chain length but the same in hydrophilic headgroup. One can consider ht and ht_3 as the *coarse* models of methanol and *n*-propanol, respectively. Note that alcohol molecules are amphiphilic. The particles w, h, and t interact each other in the same way as described in Section 5.2.1, but the neighboring particles in the amphiphile are connected together by Equation (5.1) with $l_0 = d_S$ and $k = 200\epsilon_S/d_S^2$. The thermodynamic state of an amphiphile–water mixture is $\rho^* = \rho d_S^3 = 0.7$ and $T^* = k_B T/\epsilon_S = 1.0$. The average separation of the connected particles is found to be

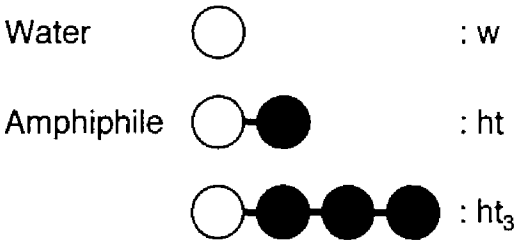

Figure 7.2. Illustration of the simple models of water and amphiphile (alcohol) molecules. Symbols w, h, and t denote waterlike, headlike, and taillike particles, respectively. Two amphiphiles used are displayed.

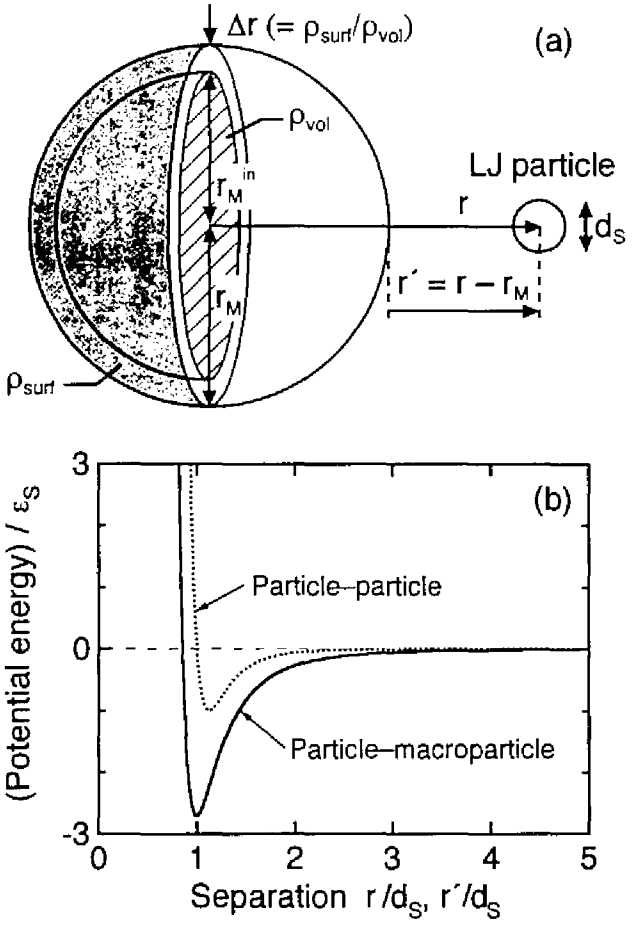

Figure 7.3. (a) Schematic of the macroparticle. (b) Particle–macroparticle potential energy, as a function of the distance from the surface r' ($= r - r_M$). The macroparticle is composed of Lennard-Jones particles, which are uniformly located on the spherical surface of radius $r_M = 5d_S$ at density $\rho_{surf} = 2^{-1/3}/d_S^2$ and in the inner sphere of radius r_M^{in} ($= r_M - \Delta r$) at density $\rho_{vol} = 1/d_S^3$, where $\Delta r = \rho_{surf}/\rho_{vol} = 2^{-1/3} d_S$ (see the text).

$1.06d_S$ in the present systems.

7.2.2 Hydrophilic macroparticle

Suppose that a macroparticle of diameter $d_M = 10d_S$ ($= 2r_M$) is composed of LJ particles, as shown in Figure 7.3(a); that is, the LJ particles are uniformly located on the spherical surface of radius r_M at surface density $\rho_{surf} = 2^{-1/3}/d_S^2$ and in the inner sphere of radius r_M^{in} ($= r_M - \Delta r$) at volume density $\rho_{vol} = 1/d_S^3$, where $\Delta r = \rho_{surf}/\rho_{vol} = 2^{-1/3}d_S$. The particle–macroparticle potential is derived after the analytical calculation (see Appendix B):

$$\psi(r) = \frac{2\pi\rho_{surf}d_S^2 r_M \varepsilon_S}{r}\left[\frac{2}{5}\left(\frac{d_S}{r-r_M}\right)^{10} - \left(\frac{d_S}{r-r_M}\right)^4\right] + \frac{\pi\rho_{vol}d_S^3 r_M^{in}\varepsilon_S}{3r}\left\{\frac{1}{30}\left[8\left(\frac{d_S}{r-r_M^{in}}\right)^9 - \frac{d_S}{r_M^{in}}\left(\frac{d_S}{r-r_M^{in}}\right)^8\right] - \left[2\left(\frac{d_S}{r-r_M^{in}}\right)^3 - \frac{d_S}{r_M^{in}}\left(\frac{d_S}{r-r_M^{in}}\right)^2\right]\right\}, \quad (7.1)$$

where r is the center-to-center separation between the particle and macroparticle. On the right-hand side of Equation (7.1), the first and second terms indicate the interactions of a particle with the outermost surface and the inner sphere of a macroparticle, respectively. Figure 7.3(b) shows the potential energy given by Equation (7.1), whose profile is similar to that by Equation (6.2b) as shown in Figure 6.2. The potential has a minimum of $-2.72\varepsilon_S$ at $r' = 0.992d_S$, where r' indicates the distance from the macroparticle surface, $r - r_M$.

To represent a hydrophilic macroparticle, Equation (7.1) is truncated and shifted using Equation (6.2a) with cutoff distances of $R_{Mj}^{cut} = 5d_S$ and $0.992d_S$. The interaction between particle j and macroparticle M includes the repulsive and attractive forces using $R_{Mj}^{cut} = 5d_S$, when they are of the same kind; otherwise,

TABLE 7.1: Systems of constrained MD simulations

System	Fluid [a]	X_A [b]	Macroparticle pair	Diameter d_M	Box length L
I	w	0.00	Hydrophilic	$10d_S$	$53.8d_S$
II	ht_3	1.00	Hydrophilic	$10d_S$	$53.8d_S$
III	ht	1.00	Hydrophilic	$10d_S$	$53.8d_S$
IV	ht_3–w	0.70–0.98	Hydrophilic	$10d_S$	$53.8d_S$
V	ht–w	0.50–0.95	Hydrophilic	$10d_S$	$53.8d_S$

[a] The total number of particles N is 108,000 and the thermodynamic state is $\rho^* = \rho d_S^3 = 0.7$ and $T^* = k_B T/\varepsilon_S = 1.0$.

[b] Volume fraction of amphiphiles in a fluid; that is, $X_A = n_{site} N_A/N$, where N_A denotes the number of amphiphiles with n_{site} sites.

their interaction is completely repulsive using $R_{Mj}^{cut} = 0.992d_S$.

The direct macroparticle–macroparticle interaction is not considered here (i.e., $F^{dir}(R) \equiv 0$), although it is described by Equation (6.7) approximately. This treatment is reasonable and hardly influences the results presented below, because the interaction between the macroparticles is almost attributable to the interaction caused by the fluid and the direct interaction is not significant, as described in Section 6.4.

7.3 Constrained molecular dynamics simulations

Table 7.1 shows five systems employed, where a pair of hydrophilic macroparticles is immersed in water (I), an amphiphilic liquid of ht_3 or ht (II, III), or an amphiphile–water mixture (IV, V). The method and procedure for the constrained MD simulation are almost the same as explained in Sections 6.3.1 and 6.3.2, respectively. The main different points are described below.

7.3.1 Methods

The systems are composed of two macroparticles of $d_M = 10d_S$ and 108,000 particles in a cubic cell with three-dimensional periodicity. The length of the cubic cell is selected to be $53.8d_S$ such that the density of the bulk fluid ρ^* is 0.7. The temperature of the fluid is kept at $T^* = 1.0$, using the Berendsen's heat bath method with a time constant of $\tau_T = 0.928\tau_0$ [Berendsen *et al.*, 1984], where $\tau_0 = d_S(m_S/\varepsilon_S)^{1/2}$. A time step of $\Delta t = 0.00464\tau_0$ is used, whose value is the same as in Chapters 5 and 6.

7.3.2 Preparation of dense amphiphilic liquids

When the fluid employed is a simple fluid, it is easy to prepare an equilibrated sample starting from an arbitrary configuration (e.g., the face-centered-cubic lattice). This method can not be applied to a dense complex fluid with chain molecules. For this reason, the modified technique was taken in Section 5.2.5. But the more sophisticated method is presented below, which is similar to the method proposed by McKechnie *et al.* [1992; Clarke, 1995].

1) Pure amphiphilic liquids

First of all, a pure amphiphile fluid is considered, in which the amphiphile consists of n_{site} particle sites and the number of the amphiphiles employed is N_A. The method for the sample preparation has three steps:

(I) An initial set of coordinates is generated for all the sites of amphiphiles, where the total number of particles N is equal to $n_{site}N_A$.

(II) These initial configurations are relaxed by a short simulation, but the amphiphiles are treated as chains composed of soft-spheres.

(III) After the chains are replaced by the amphiphiles, the configurations are equilibrated sufficiently by the successive long simulation.

For the sake of convenience, the sites in a linear amphiphile are numbered 1, ···,

n_{site} from the end h to the other end t.

Step I. A pair of macroparticles C and D is positioned at a given separation on a diagonal line of the cell. After that, the position of the site 1 in an amphiphile is determined at random and then the rest sites 2, $\cdots$, n_{site} are generated following the line from the site 1 with the random direction; these sites are placed in the space excluding the macroparticle regions and the separations between the neighboring sites are set to be $1.0d_S$. The same procedure is repeated such that N_A amphiphiles are constructed. Thus, all excluded volume effects are ignored except the space of macroparticles. This will lead to a large number of overlaps between the particle sites.

Step II. In order to implement the stable computation, one has to gently introduce the excluded volume effects into the amphiphile sites. For this reason, all the sites are treated as soft-spheres using Equation (5.2) with $R_{ij}^{cut} = 2^{1/6}d_S$. The interaction force between these soft-spheres is constrained to be a constant value of F^{tr} only when they are within a critical separation R^{tr} [McKechnie *et al.*, 1992; Clarke, 1995]:

$$-\frac{du_{ij}^{m}(r)}{dr} \equiv F^{u}\left(=-\frac{d\phi_{ij}(R^{tr})}{dr}\right) \quad \text{for } r \le R^{tr}. \tag{7.2}$$

The modified form of the shifted Lennard-Jones potential is then

$$u_{ij}^{m}(r) = \begin{cases} (R^{tr}-r)F^{tr} + \phi_{ij}(R^{tr}) - \phi_{ij}(R_{ij}^{cut}), & r \le R^{tr}, \\ \phi_{ij}(r) - \phi_{ij}(R_{ij}^{cut}), & R^{tr} < r \le R_{ij}^{cut}, \\ 0, & r > R_{ij}^{cut}, \end{cases} \tag{7.3}$$

where R^{tr} must be sufficiently small such that soft-spheres are hardly within this separation after the short relaxation, but not so small that the large value of F^{tr} causes the unstable computation.

The macroparticles are also treated as large soft-spheres. The interaction

between these macroparticle and a particle is set to be completely repulsive using Equations (6.2a) and (7.1) with $R_{Mj}^{cut} = 0.992d_S$.

The short relaxation is performed using Equation (7.3) as follows. The value of R^{tt} is decreased from $0.9d_S$ to $0.7d_S$ for 5×10^3 time steps using $\Delta t = 0.00464\tau_0$. The strong spring of $k = 1{,}000\varepsilon_S/d_S^2$ is used such that no bond connecting the sites is broken during the introduction process of the excluded volume. The temperature is kept at $T^* = 1.0$ by scaling the particle velocity at each step to remove a large amount of the thermal energy released. Note that the scaling at every step corresponds to the use of the heat bath with $\tau_T = 0.00464\tau_0$ $(= \Delta t)$.

Step III. After the above short relaxation, all the chains of soft-spheres are treated as the amphiphiles with $k = 200\varepsilon_S/d_S^2$ and the large soft-spheres are treated as the hydrophilic macroparticles. The subsequent relaxation of the amphiphilic liquids, ht and ht_3, is performed for 2.5×10^4 and 6×10^4 time steps, respectively.

2) Amphiphile–water mixtures

When an amphiphile–water mixture is simulated, all the sites in a specific number of amphiphiles are replaced by w particles using the equilibrated sample of a pure amphiphilic liquid, such that the desired number, N_W, of w particles are generated, where $N_W + n_{site}N_A = N$. Thereafter, the system is sufficiently equilibrated over 1×10^5–4×10^5 time steps.

7.3.3 Simulation procedures

1) Force–distance profile

The nearest separation between macroparticles, $R' = R - d_M$, ranges from $1.0d_S$ to 6.0–$8.0d_S$ with increments of $0.1d_S$ and $0.2d_S$. In each system, a series of constrained MD simulations are performed as follows:

(i) The separation between macroparticles C and D is chosen to be the largest value of R' and the equilibrated fluid is prepared as described in Section 7.3.2.

(ii) The instantaneous forces of $\mathbf{F}_{CS}$ and $\mathbf{F}_{DS}$ are computed during 6×10^4–8×10^4 time steps to obtain the force $F^{solv}(R)$ using Equation (6.4).

(iii) Then, external forces are assigned to the macroparticles along the C–D line for 5×10^3 time steps to reduce the C–D separation by $0.1d_S$ or $0.2d_S$.

(iv) For equilibration of the fluid around the macroparticles, the system is allowed to evolve for another 5×10^3–2.5×10^4 time steps, keeping the new C–D separation.

Repeating the procedure from (ii) to (iv), one can obtain the force–distance profile. This profile is evaluated for Systems I–III and for Systems IV and V of $X_A = 0.90$.

2) Adhesion force

The force profile exhibits the maximum attraction at the surface separation of $R' \approx 2d_S$, as is shown in Section 7.4.3. The adhesion forces in Systems IV and V of various concentrations of X_A are computed. The simulation procedure is the same as described above, but the total number of the simulation steps exceeds 2×10^5.

7.4 Results and discussion

In Sections 7.4.1 to 7.4.3, Systems I–V are investigated mainly in terms of (i) the amphiphile and water densities near the macroparticle surface, g_{MA} and g_{MW}, and (ii) the interaction force between the surfaces, F_{MM} (= F^{solv}). Section 7.4.4 deals with the problem (iii) how the adhesion force is influenced by the concentration and molecular architecture of amphiphiles.

7.4.1 Surface force in pure water

Figures 7.4 and 7.5 show the density profile of waterlike particles near the hydrophilic surface and the interaction force between the surfaces, respectively.

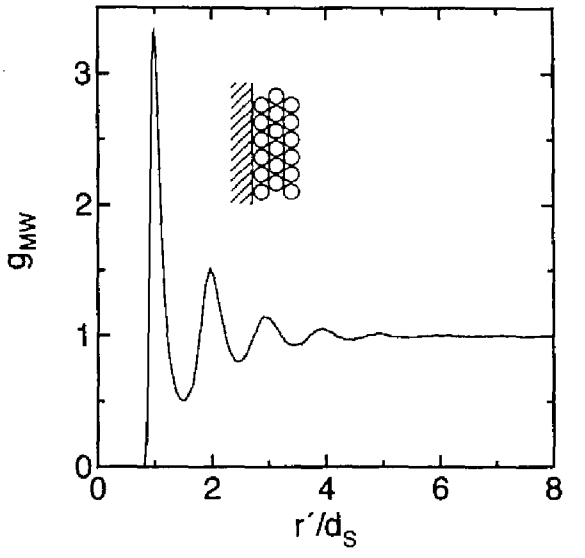

Figure 7.4. Reduced density profile of waterlike particles near the surface of the hydrophilic macroparticle in System I.

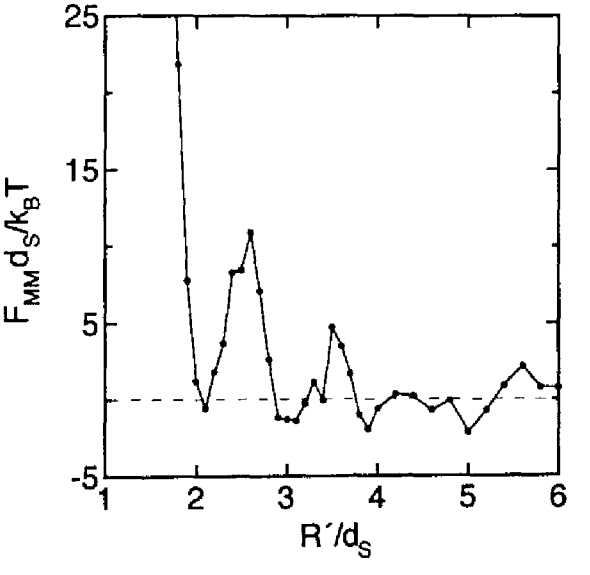

Figure 7.5. Interaction force between the hydrophilic macroparticles in System I.

The dense water layers are formed next to the surface. Accordingly the surface force oscillates with the periodicity of about a water diameter and is steeply repulsive at the small separation. The similar behavior is observed in Figures 6.7 and 6.8, where the LJ solvent used is more fluidlike ($\rho^* = 0.5925$ and $T^* = 1.2$) and the solvent–macroparticle interaction is stronger (compare Figures 6.2 and 7.3(b)).

7.4.2 Surface forces in pure amphiphilic liquids

1) Pure ht_3 solution

Density profile. Figure 7.6 shows the density profiles of the center-of-mass (c.o.m.) and sites 1–4 of amphiphiles near the hydrophilic surface. The profiles of sites 1–4 have a peak at $r' = 0.99d_S$, $1.96d_S$, $2.84d_S$, and $3.63d_S$, respectively, whose neighboring gaps are roughly equal to the average bond length of $1.06d_S$; hence, amphiphiles are adsorbed almost vertically on the surface with their heads and tails pointing toward and away from the surface, respectively. This vertical adsorption of amphiphiles agree well with the adsorption model by Kanda *et al.* [1998] (see Figure 7.1(a)). The profiles of sites 1–4 have another peak at $r' = 5.56d_S$, $4.53d_S$, $3.86d_S$, and $3.01d_S$, respectively, whose order is opposite to that in the above case; therefore, amphiphiles are adsorbed on the first layer of amphiphiles, pointing their tails toward the layer, to form an amphiphile bilayer. This bilayer formation is explained also by two peaks of the c.o.m. profile.

The average thickness of the bilayer, H_1, is defined as the separation between two major peaks of the site-1 profile plus d_S which represents the size of two hemispheres of h particles. H_1 is evaluated to be $5.6d_S$. It is worth noting that the 4th sites of amphiphiles in the second layer, at $r' = 3.01d_S$, are located closer to the surface than those in the first layer, at $r' = 3.63d_S$. This indicates that the amphiphiles in the second layer penetrate into those in the first layer.

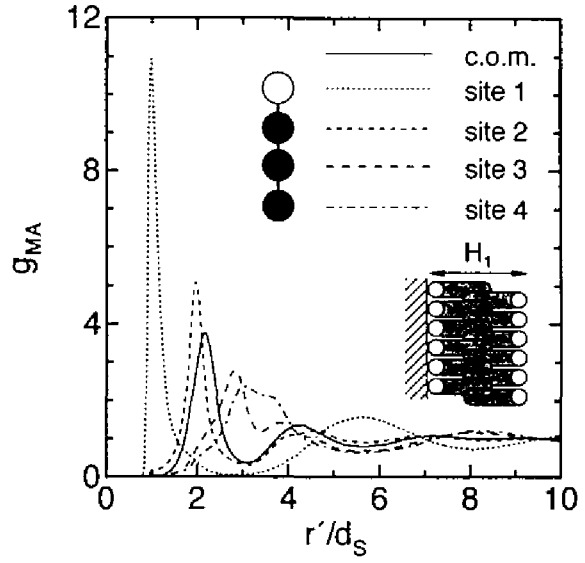

Figure 7.6. Reduced density profile of amphiphile molecules near the surface of the hydrophilic macroparticle in System II.

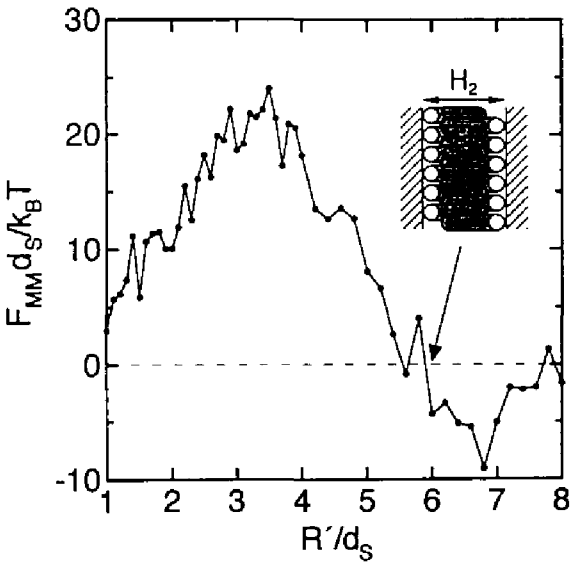

Figure 7.7. Interaction force between the hydrophilic macroparticles in System II.

Force–distance profile. The interaction force between the hydrophilic macroparticles across amphiphiles is shown in Figure 7.7. The force is strongly attractive around $R' = 6.8d_S$, but becomes repulsive at $R' \approx 5.9d_S$ in which the well-ordered bilayer is formed between the surfaces. The latter distance is referred to as the "stable separation" in this chapter. The thickness of the stable film, H_2, is defined as the stable separation minus d_S which represents the net width excluded by two surfaces. The value of $H_2 = 4.9d_S$ is smaller than that of $H_1 = 5.6d_S$, indicating that the tail chains of amphiphiles in one layer enter deeply into the other layer, compared with the case of the single surface. This behavior is attributable to the presence of the second surface.

When the surfaces approach closer, the strong repulsion occurs because of the steric hindrance between the tails of amphiphiles. The clear steplike force curve as in the AFM measurements [Kanda *et al.*, 1998] is not found in Figure 7.7, despite of the agreement in the vertical adsorption of amphiphiles on the surface. This is probably because the amphiphiles used are flexible as pointed out in Section 5.2.1. Note that the force–distance profile is not oscillatory within the range of $R' \leq 8d_S$.

2) Pure ht solution

Density profile. Figures 7.8 shows that the site profile has two major peaks at $r' = 0.99d_S$ and $3.91d_S$ for site 1 and at $r' = 1.94d_S$ and $2.84d_S$ for site 2. These peaks appear in the same way as described in the case of the pure ht_3 solution. The c.o.m. profile has two peaks at $r' = 1.44d_S$ and $3.24d_S$. These results indicate that an amphiphile bilayer with a thickness of $H_1 = 3.9d_S$ is formed at the surface.

Force–distance profile. Figure 7.9 shows that the steric repulsion occurs at the short separation and is weak in strength, compared with that for ht_3 shown in Figure 6. This behavior is attributable to a shorter tail of ht than that of ht_3. The value of H_2 is evaluated to be $3.3d_S$ and smaller than that of $H_1 = 3.9d_S$. This result is similar to that in the case of ht_3 as described above. In the range of $R' <$

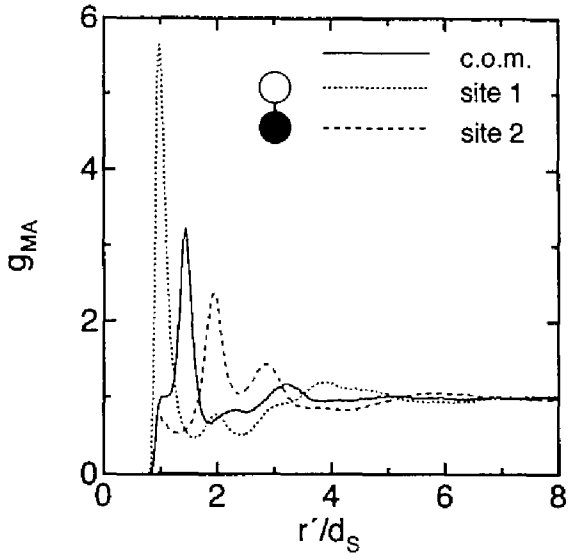

Figure 7.8. Same as in Figure 7.6 but in System III.

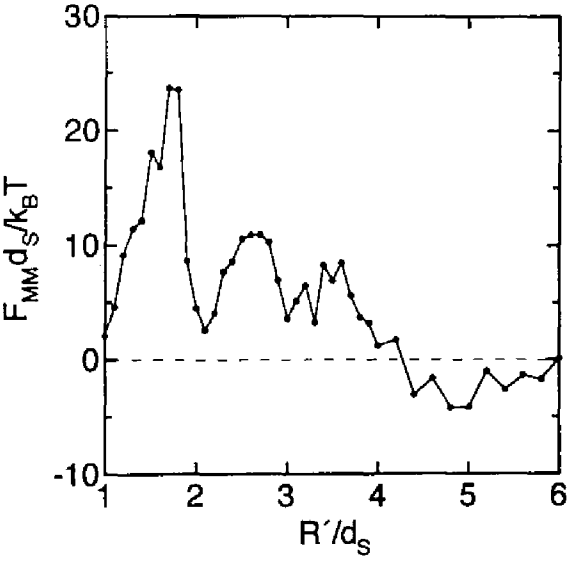

Figure 7.9. Same as in Figure 7.7 but in System III.

$4d_S$, the force oscillates with the periodicity of d_S, because the ht *dumbbells* form a molecularly-ordered film between the surfaces.

7.4.3 Surface forces in amphiphile–water mixtures

1) ht_3 solution of 90 vol %

Density profile. The ht_3 solution of $X_A = 0.9$ containing 10 vol % water is employed. Figure 7.10 displays the density profiles of amphiphile and water molecules near the surface. The amphiphile profile is similar to that for $X_A = 1$ shown in Figure 7.6, indicating that the amphiphile bilayer is formed at the surface even in the presence of water. Water molecules are remarkably concentrated next to the surface and also located around the point of $r' = 6.8d_S$, which is about d_S away from the peak of the site-1 density at $r' = 5.7d_S$; however, they hardly exist in the region of $r' = 2.2$–$5.0d_S$. These results suggest that water molecules are excluded from the hydrophobic interior of the bilayer and located near the hydrophilic outer-surfaces of the bilayer.

For an amphiphile–water mixture, H_1 is defined as the separation between two major peaks of the water profile plus d_S. The value of H_1 represents the average thickness of a bilayer of hydrated amphiphiles and is evaluated to be $6.8d_S$. It is worth noting that the c.o.m., site-1, and site-2 profiles have a shoulder at the point about d_S away from the first peak next to the surface, although no shoulder is observed in Figure 7.6. This indicates that a specific number of amphiphiles are adsorbed vertically on the surface, interposing a water molecule between their heads and the surface, as shown in the inset of Figure 7.10(b). This *solvent-separated* adsorption of amphiphiles was not expected by Kanda *et al.* [1998] as in Figure 7.1(a).

The number ratio of water and amphiphile molecules adsorbed on the surface, $P_{W/A}^{surf}$, is roughly calculated using the values of the first maxima of water and

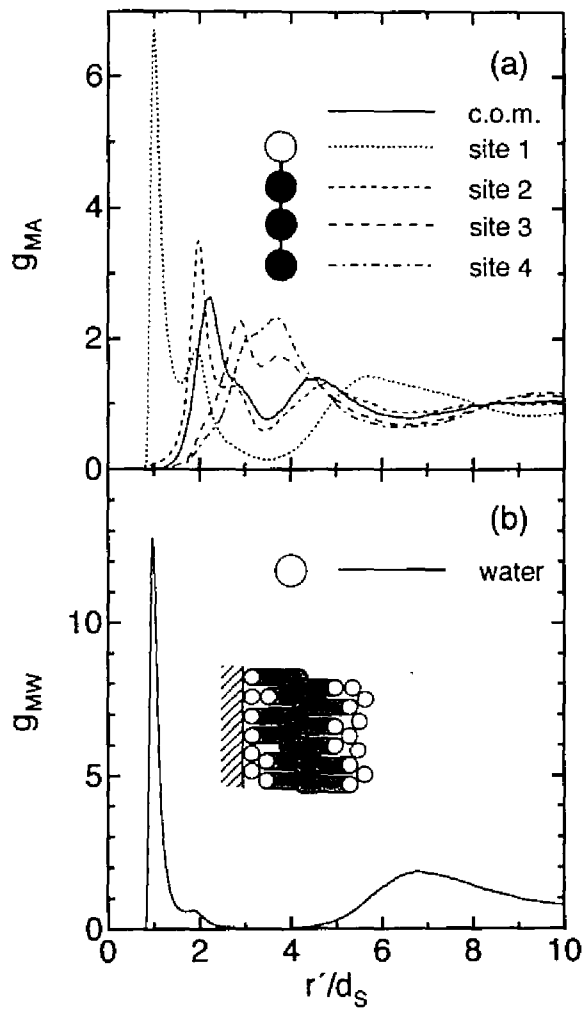

Figure 7.10. Reduced density profile of amphiphile and water molecules near the surface of the hydrophilic macroparticle in System IV of $X_A = 0.90$.

amphiphile profiles:

$$P_{W/A}^{surf} = \frac{(1st\ maximum\ of\ g_{MW})}{(1st\ maximum\ of\ g_{MA}\ for\ site\ 1)} P_{W/A}^{bulk}, \tag{7.4a}$$

$$P_{W/A}^{bulk} = \frac{1 - X_A}{X_A / n_{site}}, \tag{7.4b}$$

where $P_{W/A}{}^{bulk}$ represents the water/amphiphile ratio in the bulk. The values of $P_{W/A}{}^{surf}$ and $P_{W/A}{}^{bulk}$ are evaluated to be 8/9 and 4/9, respectively, in which the absolute number of amphiphiles on the surface is different from that in the bulk. These values manifest that water molecules are adsorbed on the surface almost as many as amphiphiles, although the ratio in the bulk $P_{W/A}{}^{bulk}$ is less than 1/2. This behavior indicates that the medium-averaged affinity of the surface for the w particle prevails against that for the ht_3 amphiphile, while in the absence of the medium these affinities are the same as expected from the particle–macroparticle interactions.

Force–distance profile. The force–distance profile of $X_A = 0.90$ is shown in Figure 7.11, where the profiles in pure liquids of water ($X_A = 0$) and amphiphile ($X_A = 1$) are displayed for comparison. The profile of $X_A = 0.90$ is attractive around $R' = 7.2d_S$, but repulsive in the region of $R' = 4.4$–$6.3d_S$. This behavior is similar to that in the profile of $X_A = 1$. The stable separation is about $6.3d_S$ and the value of H_2 is evaluated to be $5.3d_S$, which is smaller than that of $H_1 = 6.8d_S$.

The point to note in Figure 7.11 is that the surface force drops steeply at $R' = 4.4d_S$ and becomes attractive at $R' = 3.5d_S$. Why the force changes suddenly? To answer the question, the author calculates the densities of water and amphiphile molecules near the macroparticle pair for the separations of $R' = 4.0d_S$ and $4.4d_S$ and displays the contour maps in Figures 7.12 and 7.13. Figure 7.12 shows that amphiphiles between the macroparticles are pushed out into the bulk and water molecules enter to bridge the gap between the surfaces instead. This behavior is a

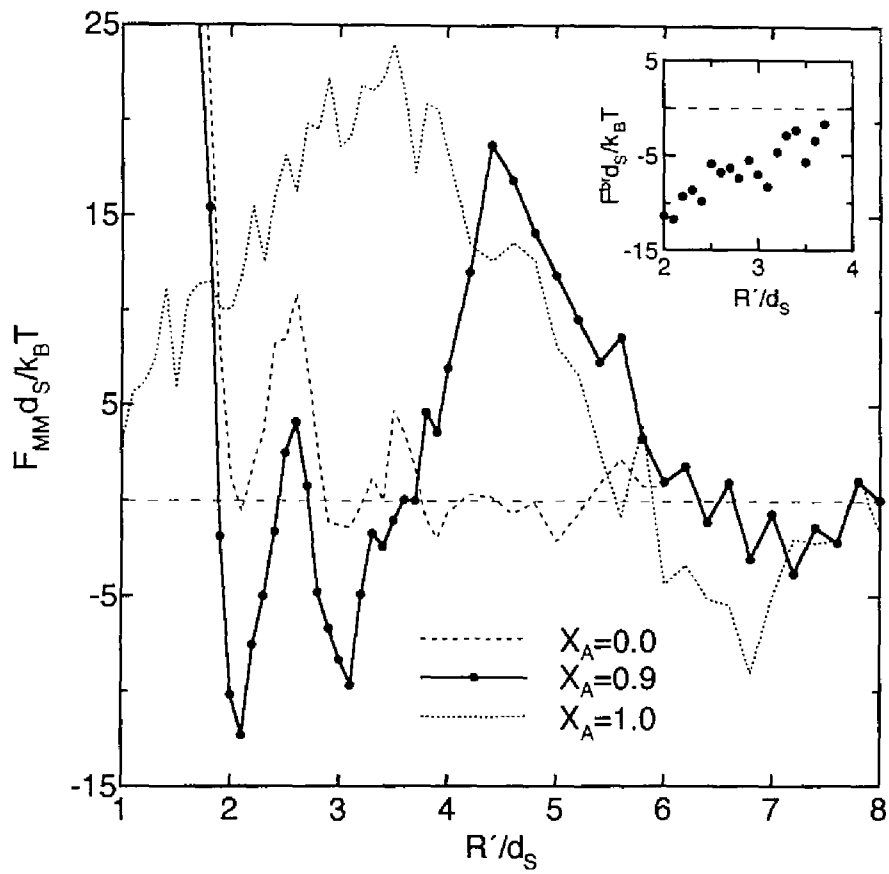

Figure 7.11. Interaction force between the hydrophilic macroparticles in System IV of X_A = 0.90. The inset represents the net force caused by the water bridging between the macroparticle surfaces (see the text).

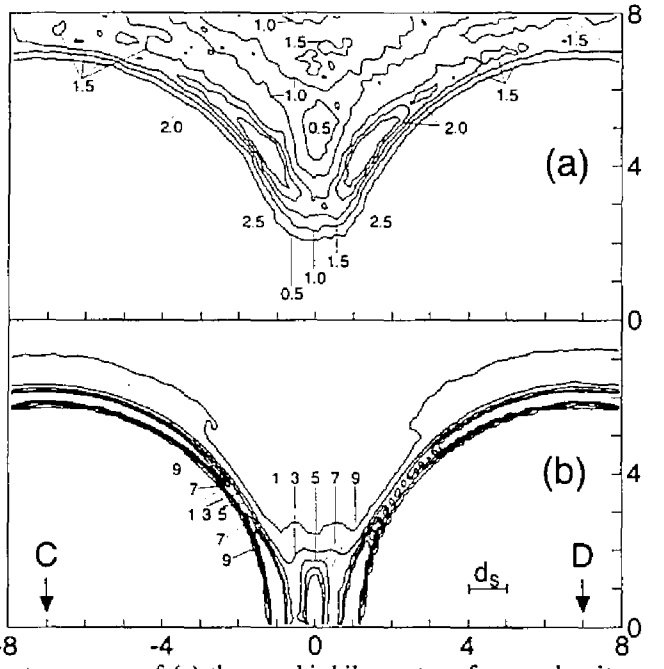

Figure 7.12. Contour maps of (a) the amphiphile center-of-mass density and (b) the water density near the hydrophilic macroparticle pair, C and D, for the separation of $R' = 4.0d_S$ in System IV of $X_A = 0.90$. Values in each panel are normalized such that the value of 1.0 indicates the density in the bulk.

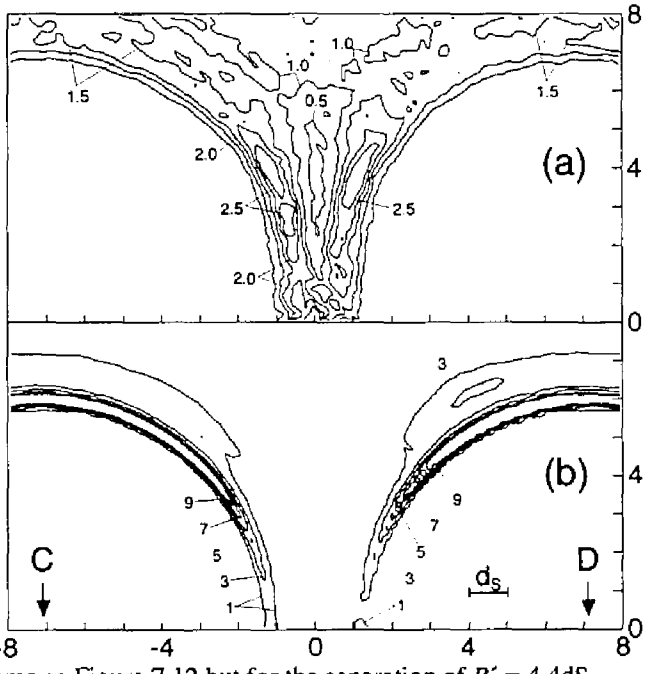

Figure 7.13. Same as Figure 7.12 but for the separation of $R' = 4.4$dS.

liquid–liquid phase separation and attributable to the size of the ht_3 amphiphile larger than that of the w particle. No similar behavior is observed in Figure 7.13, where the surface distance is increased by only $0.4d_S$. These results are the satisfactory evidence for the prediction that the attractive force at $w_{alc} = 0.9$ is caused by the water bridging between surfaces, as pictured in Figure 7.1(b) [Kanda *et al.*, 1998].

Thus, the critical feature of the surface force in Figure 7.11 is closely related to the nature of the liquid–liquid phase separation between the surfaces. The water bridge appears at $R' \approx 4.2d_S$, by which the minimum length of this bridge is evaluated to be about $3.2d_S$. Remember that the water layer on the surface has a thickness of d_S only, as in Figure 7.10(b). These results indicate that the water bridge appears before the surfaces with a water layer make the direct layer-to-layer contact.

Another point to note in Figure 7.11 is as follows: the surface force in the range of $R' < 3.7d_S$ oscillates with the periodicity of d_S, because of the structural hindrance between the surfaces across water molecules; however, this force is more attractive than that in pure water. One can roughly evaluate the net bridging force F^{br} by the following expression:

$$F^{br}(R'; X_A) = F_{MM}(R'; X_A) - F_{MM}(R'; X_A = 0), \tag{7.5}$$

where $F_{MM}(R'; X_A)$ represents the surface force at separation R' in a solution of X_A. The result shown in the inset of Figure 7.11 reveals that F^{br} becomes more attractive as the surfaces approach closer. This feature reminds the author of the bridging-force profile given by the analytical expression [Israelachvili, 1991, Equation (15.34)]. Main contributions to the strong attraction are considered to be:

(i) the Laplace pressure, resulting from the difference between the inner and outer pressures of the concave meniscus.

(ii) the force arising from the tangent component of the interfacial tension.

(iii) the difference in the osmotic pressures between the bulk region and the confined water-rich region, that is, a depletion interaction.

Unfortunately, it is difficult to evaluate these quantities appropriately, because there is no suitable expression for them.

The surface force becomes most attractive at $R' = 2.1d_S$, where the surfaces are not in contact with each other, but interpose one layer of water molecules. This feature is different from that in Figure 7.1(b). The maximum attraction is investigated in Section 7.4.4 extensively.

2) ht solution of 90 vol %

Density profile. The water and amphiphile densities near the surface are displayed in Figure 7.14 and the following features are drawn:

(i) A hydrated amphiphile bilayer with a thickness of $H_1 = 5.0d_S$ is formed near the single surface.

(ii) Water molecules are not excluded from the hydrophobic interior of the bilayer because of a short tail of the ht amphiphile.

(iii) Water molecules are concentrated next to the surface, in which the number ratio of $P_{W/A}^{surf} = 7.3/9$ is about four times lager than that of $P_{W/A}^{bulk} = 2/9$.

Force–distance profile. The force profile is shown in Figure 7.15 and the characteristics are as follows:

(i) The stable separation is about $4.6d_S$, by which the value of H_2 is evaluated to be $3.6d_S$ and smaller than that of $H_1 = 5.0d_S$.

(ii) The surface force drops at $R' = 3.5d_S$, but this decrease is even less crucial than that for ht_3 shown in Figure 7.11.

(iii) The force profile in the range of $R' = 2.4$–$3.5d_S$ is almost identical to that for pure water.

(iv) The bridging force F^{br} becomes attractive in the short range and is weak in strength compared with that for ht_3 shown in the inset of Figure 7.11.

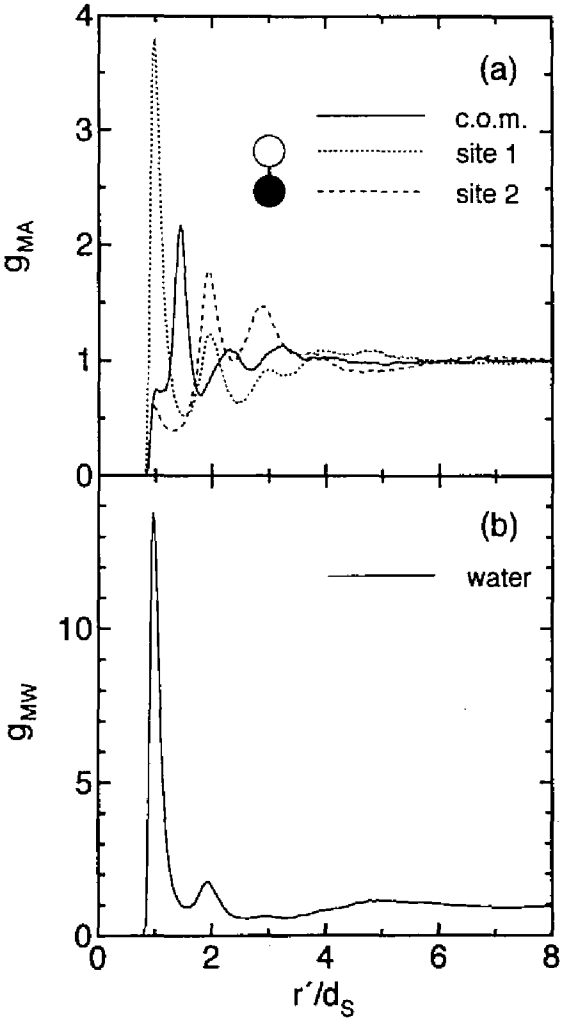

Figure 7.14. Same as in Figure 10 but in System V of $X_A = 0.90$.

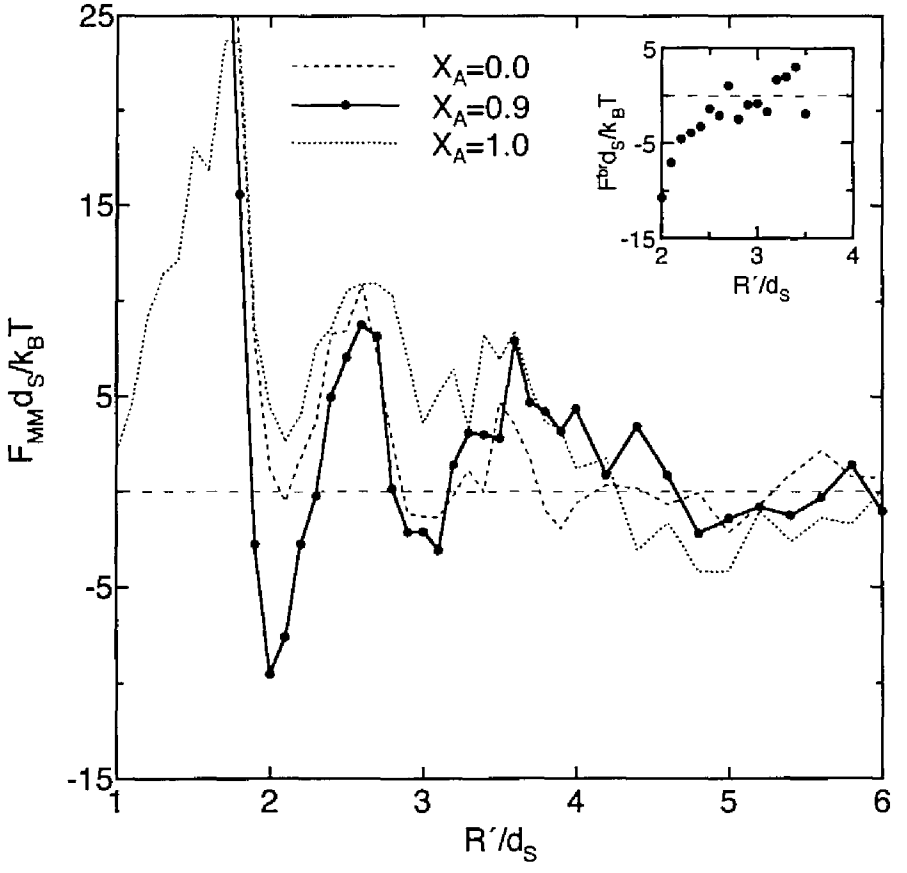

Figure 7.15. Same as in Figure 7.11 but in System V of $X_A = 0.90$.

(v) The surface force becomes most attractive at $R' = 2.0d_S$.

Careful observation of the contour maps manifests that the water bridging occurs at $R' = 3.5d_S$, but the confined film does not completely separate into two phases until $R' \leq 3.1d_S$. This non-simultaneous behavior of the bridging and the phase separation explains the less degree of the force dropping.

7.4.4 Adhesion forces

The surface force in an amphiphile–water mixture becomes most attractive at $R' \approx 2d_S$, as shown in Figures 7.11 and 7.15. This force is denoted by the adhesion force, $-F^{ad}$. The values of $-F^{ad}$ at various concentrations of X_A are computed as given in Figure 7.16. The adhesion force has a maximum at $X_A = 0.90$ for ht_3 and at $X_A = 0.85$ for ht. As an amphiphile has a longer hydrophobic tail, the adhesion force becomes maximum at a larger value of X_A and the magnitude of this maximum is larger. These results agree well with those by the AFM measurements [Kanda *et al.*, 1998].

For investigation of the mechanism of the adhesion, the attention is focused on the water adsorbed near the macroparticle pair. The contour maps at around the maximum of $-F^{ad}$ are displayed in Figure 7.17 for ht_3 and Figure 7.18 for ht. The water density near the macroparticles is reduced from panels (a) to (c) of Figures 7.17 and 7.18, where panel (b) corresponds to the water density at a maximum of $-F^{ad}$. This indicates that the adhesion force becomes maximal when the macroparticle pair is moderately *wetted* by water. Comparison in Figures 7.17 and 7.18 manifests that the interface between the water meniscus and the amphiphiles of ht_3 is clearer than that for ht. This behavior is expected from comparison in Figures 7.10 and 7.14. These results explain the stronger adhesion force in the ht_3–w mixture.

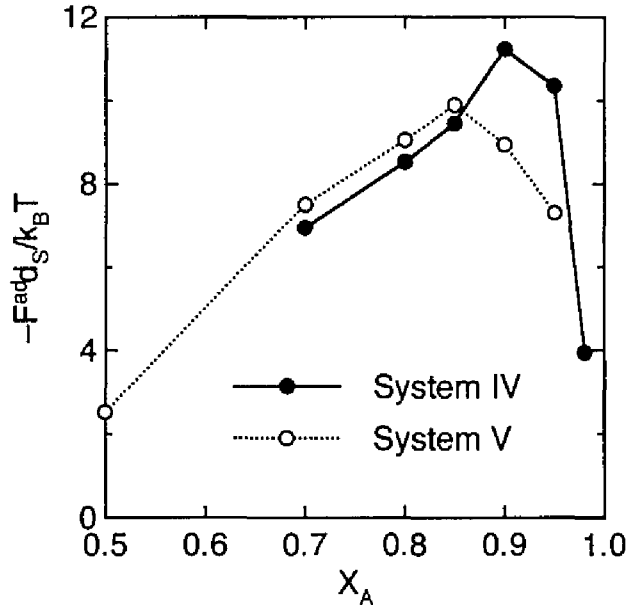

Figure 7.16. Adhesion force between the hydrophilic macroparticles, $-F^{ad}$, in Systems IV and V of various concentrations of X_A.

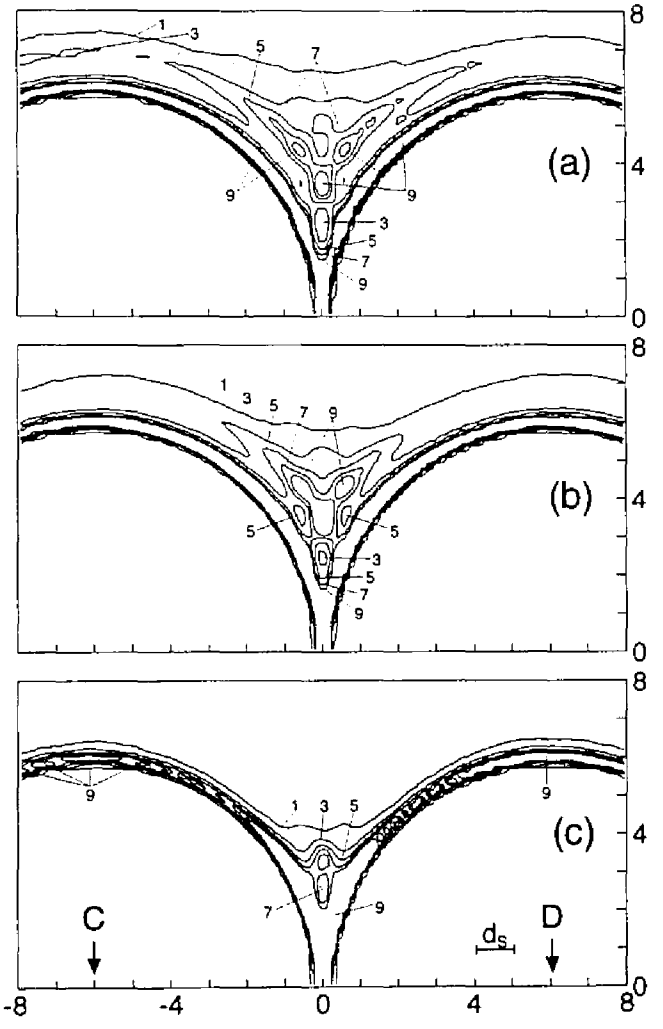

Figure 7.17. Contour maps of the water density near the hydrophilic macroparticle pair, C and D, for the separation of $R' = 2.1d_S$ in System IV of $X_A = 0.85$ (a), 0.90 (b), and 0.95 (c). Values in each panel are normalized such that the value of 1.0 indicates the density in the bulk.

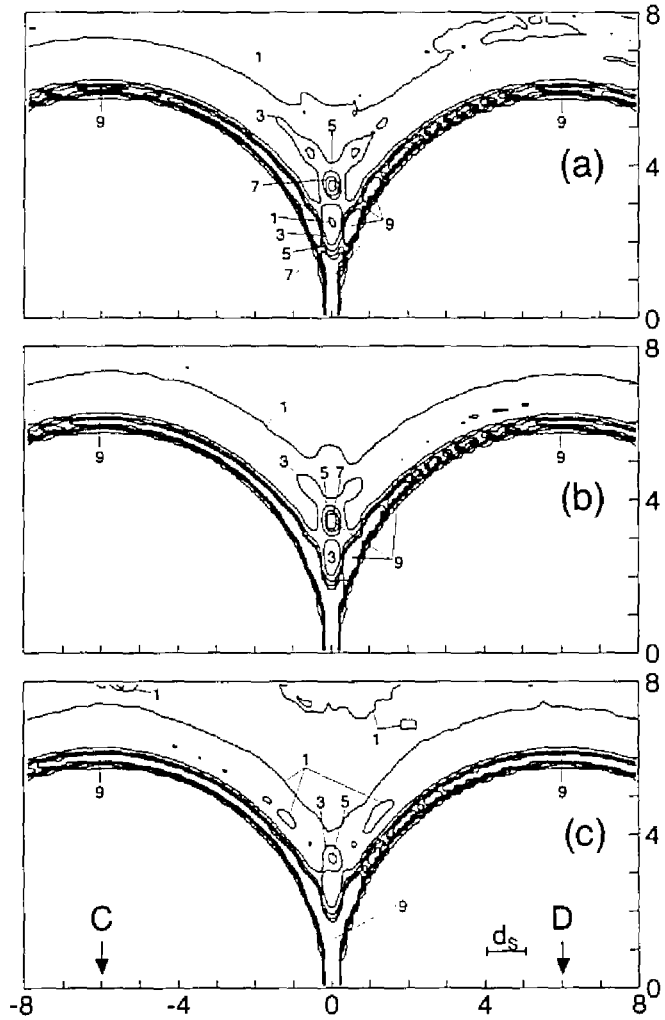

Figure 7.18. Same as Figure 7.17 but near the hydrophilic macroparticle pair for the separation of $R' = 2.0d_S$ in System V of $X_A = 0.80$ (a), 0.85 (b), and 0.90 (c).

7.5 Concluding remarks

In this chapter, the interaction forces between hydrophilic macroparticles in an alcohol–water mixture are investigated systematically using the simulation methods given in Chapters 5 and 6. As the results, the following conclusions are drawn.

Pure amphiphilic liquids:

(i) Amphiphile molecules are adsorbed vertically on the hydrophilic surface to form an amphiphile bilayer.

(ii) The surface force is strongly repulsive at the separation less than about the thickness of the bilayer.

Amphiphile–water mixtures:

(iii) In the presence of 10 vol % water, a bilayer of hydrated amphiphiles is formed near the hydrophilic surface, where waterlike particles are remarkably concentrated.

(iv) When the surfaces approach each other, their interaction force is repulsive, whose profile is similar to that in a pure amphiphilic liquid. However, the surface force becomes attractive suddenly at the separation less than the length of the amphiphile molecule. This behavior is attributable to the liquid–liquid phase separation between the surfaces, in which amphiphiles are pushed out into the bulk and waterlike particles enter to bridge the gap between the surfaces instead.

(v) The adhesion force has a maximum at a higher concentration of X_A ($\simeq 0.9$) and the magnitude of this maximum is larger, as an amphiphile has a longer hydrophobic tail. The adhesion is largely influenced by the *wetting* degree of the macroparticle pair and the sharpness of the interface between the water meniscus and the amphiphile. The features of the wetting degree and the interface sharpness depend on the concentration and molecular architecture of

amphiphiles.

(vi) The above results agree, at least qualitatively, with those by the AFM measurements [Kanda *et al.*, 1998]. This demonstrates that the present simulation method is a good tool to investigate the surface forces in a complex fluid.

8
General Conclusion

In this dissertation, the microscopic features of the liquid/solid interfaces and the interaction forces between the macroscopic solid surfaces are investigated systematically using MD simulations, in which the attention is focused on the hydrophilic and hydrophobic properties of molecules.

Chapters 2 and **3** deal with water molecules near the hydrocarbon and NaCl-crystal surfaces, respectively, which are typical hydrophobic and hydrophilic surfaces. About three strongly adsorbed layers of water molecules are formed near the hydrophilic surface, where the diffusivity of water molecules is remarkably reduced. At the hydrophobic interface the icelike structure is formed, but water molecules near the surface display the high diffusivity to exchange themselves with those in the bulk, which indicates that the icelike structure induced by the hydrophobic surface is not necessarily stable.

In **Chapter 4**, the adsorption of Na^+ and Cl^- ions onto the NaCl(001) and NaCl(011) surfaces in water are examined in terms of the free energy profiles for adsorption. It is found that the ions are adsorbed on the NaCl surfaces either directly (i.e., direct adsorption) or with a water molecule interposed between the surface and themselves (i.e., solvent-separated adsorption). It is also demonstrated that the adsorption of the ions largely depends not only on the size of the ions but also on the lattice arrangement of the surfaces.

In **Chapter 5**, the adsorption of surfactants onto the hydrophilic and hydrophobic surfaces in water is investigated. In order to make the simulation

possible within the limits of the present computational power, the interaction potentials of water, oil, and surfactant molecules and solid surfaces are simplified on the basis of the results obtained in Chapters 2 and 3; that is, the interactions are characterized by only the hydrophilicity and hydrophobicity. Simulating with this simple model, the detailed mechanism of the adsorption and aggregation of surfactants on the surface is discovered for the first time. This mechanism has not been expected and can not be investigated by the atomistic simulation because of the lack of computational power.

In **Chapter 6**, the new computational technique to evaluate the interaction force between macroscopic colloidal particles in a fluid is proposed. This method is applied to calculate the surface forces in fluids composed of simple solvent particles. It is found that the present method successfully derives the structural forces, which are caused by the adsorbed layers of solvent particles near the surface. It is also clarified that the structural forces depend largely on the properties of the solvent and the surface.

In **Chapter 7**, the interaction forces between hydrophilic surfaces in alcohol–water mixtures are calculated, using a combination of the molecular model and the evaluation method developed in Chapters 6 and 7, respectively. It is found that the liquid mixture, which exists stably as a single phase in the bulk, separates into two phases of water and alcohol near the surfaces when the surfaces approach at the distance less than the length of the alcohol molecule. Then, the strong attraction acts between the surfaces because of the water bridging. This attraction becomes maximum at a higher concentration of the alcohol ($\approx$ 90 volume %) and the magnitude of this maximum increases as the alcohol molecule has a longer hydrophobic tail. These results agree, at least qualitatively, with those by the recent AFM measurements. This demonstrates the reliability and availability of the present simulation method.

All these add up to the following conclusions:

(i) It is clarified systematically that the microscopic nature of the hydrophilicity and hydrophobicity of molecules largely influences the feature of a solid/liquid interface and the macroscopic property of the interaction force between the surfaces.

(ii) This dissertation gives a methodology to investigate the macroscopic properties of a colloidal dispersion system using the molecular information.

The author expects that this study can give the principles to control precisely the production process of particulate materials.

This dissertation deals mainly with the equilibrium states of solid/liquid interfaces and surface forces. In actual processes, however, the contribution of a non-equilibrium field becomes important in addition to these equilibrium features. Fortunately, the MD method is a good tool to investigate the influence of non-equilibrium fields such as mass flow and heat flow. In the near future, the author will start non-equilibrium MD (NEMD) simulations to elucidate the solid/liquid interface and the surface force in non-equilibrium states and the further problems lying in a colloidal dispersion system.

Appendices

Appendix A
Electrostatic Analogy for a Simple Model System

The simple models for an oil/water/surfactant system and a solid wall are given in Sections 5.2.1 to 5.2.3. The efficiency and reliability of these models are confirmed in Section 5.3. Then, how dose the simple model system correspond to a real Coulomb system? To answer the question, Wu *et al.* [1992] developed a concept of frustrating charges and created a theory of surfactant self-assembly. Here, a simple consideration of the surfactant–wall interactions is given.

The adsorption of an ionic surfactant on a hydrophilic surface is driven by the strong electrostatic head–surface interaction, which corresponds to the H´–wall interaction in the simple model system, as described in Section 5.2.3. The rate of the adsorption depends on the strength of this interaction. Hence, the strength of the H´–wall interaction is determined by the following consideration.

Suppose that a water molecule and a surfactant headgroup are represented by the hard-spheres of 0.28 nm diameter with a point dipole of μ_{water} = 1.85 Debye and a point charge of $q_{head} = +e$, respectively, and a hard wall has charge sites of $q_{site} = -e$. When the water and the head interact with the charge site, their binding energies are estimated as follows (see also the literature by Israelachvili [1991]):

$$-\frac{\mu_{water} q_{site} \cos\theta}{4\pi\varepsilon_0 r^2} = -1.1 \times 10^{-19}\ \mathrm{J} \quad \text{for water–site,} \tag{A.1}$$

$$\frac{q_{head} q_{site}}{4\pi\varepsilon_0 r} = -8.2 \times 10^{-19}\ \mathrm{J} \quad \text{for head–site,} \tag{A.2}$$

where the dipole orientation of $\cos\theta = -1$ and the separation of r = 0.28 nm are

used. The head–site interaction is 7.5 times lager than the water–site interaction.

On the basis of this result, the energy parameter for H´–wall interaction is chosen to be ten times stronger than that for w–wall interaction. Although the above calculation is not completely correlated with the simple model system, the author thinks that the model used is plausible as far as the possible mechanism of the adsorption and aggregation of surfactants on the surface is concerned.

Appendix B
Potentials for Particle–Macroparticle Interaction

The potential function for particle–macroparticle interaction is derived following Hamaker [1937], who presented the van der Waals attraction between two macroparticles.

The particle–particle interaction is given by the Lennard-Jones (LJ) potential:

$$u(r) = 4\varepsilon\left[\left(\frac{\sigma}{r}\right)^{12} - \left(\frac{\sigma}{r}\right)^{6}\right]. \tag{B.1}$$

Consider a sphere of radius r_M and center O and a particle P outside at a distance OP = r, as shown in Figure B.1. Two types of spheres are considered:

(I) the sphere containing the LJ particles uniformly at volume density ρ_{vol}.

(II) the hollow sphere whose surface is uniformly composed of the LJ particles at surface density ρ_{surf}.

Sphere I. The sphere around O will cut out from a second sphere of radius l around P a surface ABC, whose area is then

$$\text{Surface (ABC)} = \int_0^{\theta_0} (2\pi l \sin\theta)\, l\,d\theta = 2\pi l^2(1 - \cos\theta_0), \tag{B.2}$$

where θ_0 is given by

$$r_M^2 = r^2 + l^2 - 2rl\cos\theta. \tag{B.3}$$

Equation (B.2) yields

$$\text{Surface (ABC)} = \frac{\pi l}{r}\left[r_M^2 - (r-l)^2\right]. \tag{B.4}$$

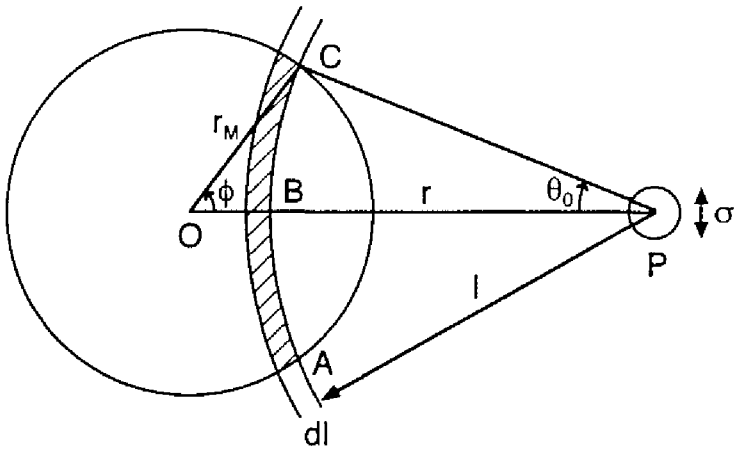

Figure B.1. Schematic of a particle and a macroparticle to derive potential functions for particle–macroparticle interaction.

The potential energy of an LJ particle at P is written down as

$$u_{\mathrm{P}}(r) = \int_{r-r_{\mathrm{M}}}^{r+r_{\mathrm{M}}} \rho_{\mathrm{vol}}\, u(l) \cdot \frac{\pi l}{r}\left[r_{\mathrm{M}}^2 - (r-l)^2\right] \mathrm{d}l. \tag{B.5}$$

Carrying out the integration we get u_{p} as a function of r:

$$u_{\mathrm{P}}(r) = \frac{\pi\rho_{\mathrm{vol}}\sigma^4\varepsilon}{3r}\left\{\frac{1}{30}\left[\frac{8r_{\mathrm{M}}\sigma^8}{(r+r_{\mathrm{M}})^9} + \frac{8r_{\mathrm{M}}\sigma^8}{(r-r_{\mathrm{M}})^9} + \frac{\sigma^8}{(r+r_{\mathrm{M}})^8} - \frac{\sigma^8}{(r-r_{\mathrm{M}})^8}\right]\right.$$
$$\left. - \left[\frac{2r_{\mathrm{M}}\sigma^2}{(r+r_{\mathrm{M}})^3} + \frac{2r_{\mathrm{M}}\sigma^2}{(r-r_{\mathrm{M}})^3} + \frac{\sigma^2}{(r+r_{\mathrm{M}})^2} - \frac{\sigma^2}{(r-r_{\mathrm{M}})^2}\right]\right\}. \tag{B.6}$$

When the sphere is sufficiently large ($r_{\mathrm{M}} > 4\sigma$), Equation (B.6) is approximated by

$$u_{\mathrm{P}}(r) = \frac{\pi\rho_{\mathrm{vol}}\sigma^3 r_{\mathrm{M}}\varepsilon}{3r}\left\{\frac{1}{30}\left[8\left(\frac{\sigma}{r-r_{\mathrm{M}}}\right)^9 - \frac{\sigma}{r_{\mathrm{M}}}\left(\frac{\sigma}{r-r_{\mathrm{M}}}\right)^8\right]\right.$$
$$\left. - \left[2\left(\frac{\sigma}{r-r_{\mathrm{M}}}\right)^3 - \frac{\sigma}{r_{\mathrm{M}}}\left(\frac{\sigma}{r-r_{\mathrm{M}}}\right)^2\right]\right\}. \tag{B.7}$$

If the sphere becomes infinitely large ($r_{\mathrm{M}} = \infty$) and the distance of P from the sphere surface, $r - r_{\mathrm{M}}$, is kept to be constant z, Equations (B.6) and (B.7) are found to be

$$u_{\mathrm{P}}(z) = \frac{2\pi\rho_{\mathrm{vol}}\sigma^3\varepsilon}{3}\left[\frac{2}{15}\left(\frac{\sigma}{z}\right)^9 - \left(\frac{\sigma}{z}\right)^3\right], \tag{B.8}$$

which is identical to the (9–3) potential for particle–wall interaction.

Sphere II. The surface ABC shown in Figure B.1 has a edge circumference with a length of $2\pi r_{\mathrm{M}} \sin\phi$, where ϕ is given by

$$l^2 = r_{\mathrm{M}}^2 + r^2 - 2r_{\mathrm{M}} r\cos\phi. \tag{B.9}$$

Differentiating Equation (B.9) with respect to ϕ we get

$$\frac{\mathrm{d}\phi}{\mathrm{d}l} = \frac{l}{r_{\mathrm{M}} r\sin\phi}. \tag{B.10}$$

The potential energy of an LJ particle at P is written down as

$$u_{\mathrm{P}}(r) = \int_0^{2\pi} \rho_{\mathrm{surf}}\, u(l) \cdot (2\pi r_{\mathrm{M}} \sin\phi)\, r_{\mathrm{M}} \mathrm{d}\phi = \int_{r-r_{\mathrm{M}}}^{r+r_{\mathrm{M}}} \rho_{\mathrm{surf}}\, u(l) \cdot \frac{2\pi r_{\mathrm{M}}}{r}\, l\mathrm{d}l, \qquad \text{(B.11)}$$

where Equation (B.10) is used for transformation. Carrying out the integration we get u_{p} as a function of r:

$$u_{\mathrm{P}}(r) = \frac{2\pi\rho_{\mathrm{surf}}\sigma^2 r_{\mathrm{M}}\varepsilon}{r}\left\{\frac{2}{5}\left[\left(\frac{\sigma}{r-r_{\mathrm{M}}}\right)^{10} - \left(\frac{\sigma}{r+r_{\mathrm{M}}}\right)^{10}\right] - \left[\left(\frac{\sigma}{r-r_{\mathrm{M}}}\right)^{4} - \left(\frac{\sigma}{r+r_{\mathrm{M}}}\right)^{4}\right]\right\}. \qquad \text{(B.12)}$$

When $r_{\mathrm{M}} > 4\sigma$, Equation (B.12) is approximated by

$$u_{\mathrm{P}}(r) = \frac{2\pi\rho_{\mathrm{surf}}\sigma^2 r_{\mathrm{M}}\varepsilon}{r}\left[\frac{2}{5}\left(\frac{\sigma}{r-r_{\mathrm{M}}}\right)^{10} - \left(\frac{\sigma}{r-r_{\mathrm{M}}}\right)^{4}\right]. \qquad \text{(B.13)}$$

If $r_{\mathrm{M}} = \infty$ and $r - r_{\mathrm{M}} \equiv z$ (= constant), Equations (B.12) and (B.13) are found to be

$$u_{\mathrm{P}}(z) = 2\pi\rho_{\mathrm{surf}}\sigma^2\varepsilon\left[\frac{2}{5}\left(\frac{\sigma}{z}\right)^{10} - \left(\frac{\sigma}{z}\right)^{4}\right], \qquad \text{(B.14)}$$

which is identical to the (10–4) potential for particle–wall interaction.

References

The number in square brackets following each entry gives the section number in which the reference is made.

Allen, M. P., and Tildesley, D. J. (1987). *Computer Simulation of Liquids*. Clarendon Press, Oxford. [1.4.1, 2.2.1, 2.2.3, 2.2.4, 4.3.2]

Allinger, N. L., Yuh, Y. H., and Lii, J.-H. (1989). Molecular mechanics. The MM3 force field for hydrocarbons. 1. *J. Am. Chem. Soc.* **111**, 8551–8566. [1.4.1]

Anastasiou, N., Fincham, D., and Singer, K. (1983). Computer simulation of water in contact with a rigid-ion crystal surface. *J. Chem. Soc., Faraday Trans. 2* **79**, 1639–1651. [1.4.2, 2.4.1, 3.1]

Attard, P., and Patey, G. N. (1990). Hypernetted-chain closure with bridge diagrams. Asymmetric hard sphere mixtures. *J. Chem. Phys.* **92**, 4970–4982. [1.3.1]

Attard, P., Bérard, D. R., Ursenbach, C. P., and Patey, G. N. (1991). Interaction force energy between planar walls in dense fluids: An Ornstein–Zernike approach with results for hard-sphere, Lennard-Jones, and dipolar systems. *Phys. Rev. A* **44**, 8224–8234. [1.3.2]

Bandyopadhyay, S., Tarek, M., and Klein, M. L. (1998a). Computer simulation studies of amphiphilic interfaces. *Curr. Opin. Colloid Interface Sci.* **3**, 242–246. [1.4.4]

Bandyopadhyay, S., Shelley, J. C., Tarek, M., Moore, P. B., and Klein, M. L. (1998b). Surfactant aggregation at a hydrophobic surface. *J. Phys. Chem. B* **102**, 6318–6322. [1.4.4]

Bareman, J. P., and Klein, M. L. (1992). Molecular dynamics simulation of a Langmuir monolayer. In *Interface Dynamics and Growth: MRS Symposium Proceedings* (eds. Liang, K. S., Anderson, M. P., Bruinsma, R. F., and Scoles, G.). p 271–279. Materials Research Society, Pittsburgh. [1.4.4]

Barraclough, P. B., and Hall, P. G. (1974). The adsorption of water vapour by lithium fluoride, sodium fluoride and sodium chloride. *Surf. Sci.* **46**, 393–417. [3.2.2]

Bellissent-Funel, M.-C., Sridi-Dorbez, R., and Bosio, L. (1996). X-ray and neutron scattering studies of the structure of water at a hydrophobic surface. *J. Chem. Phys.* **104**, 10023–10029. [1.4.2, 2.4.3]

Benjamin, I. (1992). Theoretial study of the water/1,2-dichloroethane interface: Structure, dynamics, and conformational equilibria at the liquid–liquid interface. *J. Chem. Phys.* **97**, 1432–1445. [2.4.2]

Bérard, D. R., Attard, P., and Patey, G. N. (1993). Cavitation of a Lennard-Jones fluid between hard walls, and the possible relevance to the attraction measured between hydrophobic surfaces. *J. Chem. Phys.* **98**, 7236–7244. [1.4.5, 6.4.2]

Berendsen, H. J. C., Grigera, J. R., and Straatsma, T. P. (1987). The missing term in effective pair potentials. *J. Phys. Chem.* **91**, 6269–6271. [2.3.1, 3.2.2]

Berendsen, H. J. C., Postma, J. P. M., van Gunsteren, W. F., and Hermans, J. (1981). Interaction models for water in relation to protein hydration. In *Intermolecular Forces: Proceedings of the Fourteenth Jerusalem Symposium on Quantum Chemistry and Biochemistry* (ed. Pullman, B.). p 331–342. Reidel, Dordrecht. [2.3.1]

Berendsen, H. J. C., Postma, J. P. M., van Gunsteren, W. F., DiNola, A., and Haak, J. R. (1984). Molecular dynamics with coupling to an external bath. *J. Chem. Phys.* **81**, 3684–3690. [6.3.2, 7.3.1]

Binning, G., Quate, C. F., and Gerber, C. (1986). Atomic force microscope. *Phys. Rev. Lett.* **56**, 930–933. [1.2.2]

Böcker, J., Brickmann, J., and Bopp, P. (1994). Molecular dynamics simulation study of an *n*-decyltrimethylammonium chloride micelle in water. *J. Phys. Chem.* **98**, 712–717. [1.4.4]

Böcker, J., Schlenkrich, M., Bopp, P., and Brickmann, J. (1992). Molecular dynamics simulation of an *n*-hexadecyltrimethylammonium chloride monolayer. *J. Phys. Chem.* **96**, 9915–9922. [1.4.4]

Boek, E. S., Briels, W. J., van Eerden, J., and Feil, D. (1992). Molecular-dynamics simulations of interfaces between water and crystalline urea. *J. Chem. Phys.* **96**, 7010–7018. [1.4.2, 2.4.1]

Bordarier, P., Rousseau, B., and Fuchs, A. H. (1997). Rheology of model confined ultrathin fluid films. I. Statistical mechanics of the surface force apparatus experiments. *J. Chem. Phys.* **106**, 7295–7302. [1.4.5]

Brindle, D., and Care, C. M. (1992). Phase diagram for the lattice model of amphiphile and solvent mixtures by Monte Carlo simulation. *J. Chem. Soc., Faraday Trans.* **88**, 2163–2166. [1.4.4, 5.3.2]

Brooks, B. R., Bruccoleri, R. E., Olafson, B. D., States, D. J., Swaminathan, S., and Karplus, M. (1983). CHARMM: A program for macromolecular energy, minimization, and dynamics calculations. *J. Comput. Chem.* **4**, 187–217. [1.4.1]

Carpenter, I. L., and Hehre, W. J. (1990). A molecular dynamics study of the hexane/water interface. *J. Phys. Chem.* **94**, 531–536. [2.4.2]

Chang, T.-M., and Dang, L. X. (1996). Molecular dynamics simulations of CCl_4–H_2O liquid–liquid interface with polarizable potential models. *J. Chem. Phys.* **104**, 6772–6783. [2.4.2]

Chialvo, A. A., and Debenedetti, P. G. (1990). On the use of the Verlet neighbor list in molecular dynamics. *Comput. Phys. Commun.* **60**, 215–224. [5.2.5]

Christenson, H. K. (1983). Experimental measurements of solvation forces in nonpolar liquids. *J. Chem. Phys.* **78**, 6906–6913. [1.2.1, 6.4.2]

Christenson, H. K. (1984). DLVO (Derjaguin–Landau–Verway–Overbeek) theory and solvation forces between mica surfaces in polar and hydrogen-bonding liquids. *J. Chem. Soc., Faraday Trans. 1* **80**, 1933–1946. [1.2.1]

Christenson, H. K. (1985). Forces between solid surfaces in a binary mixture of non-polar liquids. *Chem. Phys. Lett.* **118**, 455–458. [1.2.1]

Christenson, H. K. (1986). Interactions between hydrocarbon surfaces in a nonpolar liquid: Effect of surface properties on solvation forces. *J. Phys. Chem.* **90**, 4–6. [1.2.1, 6.4.2]

Christenson, H. K. (1988). Non-DLVO forces between surfaces—Solvation, hydration and capillary effects. *J. Disp. Sci. Technol.* **9**, 171–206. [1.2.1]

Christenson, H. K., and Claesson, P. M. (1988). Cavitation and the interaction between macroscopic hydrophobic surfaces. *Science* **239**, 390–392. [1.2.1]

Christenson, H. K., and Horn, R. G. (1983). Direct measurement of the force between solid surfaces in a polar liquid. *Chem. Phys. Lett.* **98**, 45–48. [1.2.1]

Christenson, H. K., and Horn, R. G. (1985). Force between mica surfaces in ethylene glycol. *J. Colloid Interface Sci.* **103**, 50–55. [1.2.1]

Christenson, H. K., Gruen, D. W. R., Horn, R. G., and Israelachvili, J. N. (1987). Structuring in liquid alkanes between solid surfaces: Force measurements and mean-field theory. *J. Chem. Phys.* **87**, 1834–1841. [1.2.1]

Ciccotti, G., Ferrario, M., Hynes, J. T., and Kapral, R. (1989). Constrained molecular dynamics and the mean potential for an ion pair in a polar solvent. *Chem. Phys.* **129**, 241–251. [6.3.1]

Clark, M., Cramer III, R. D., and van Opdenbosch, N. (1989). Validation of the general purpose Tripos 5.2 force field. *J. Comput. Chem.* **10**, 982–1012. [1.4.1]

Clarke, J. H. R. (1995). Molecular dymamics of glassy polymers. In *Monte Carlo and Molecular Dynamics Simulations in Polymer Science* (ed. Binder, K.). p 272–306. Oxford University Press, New York. [7.3.2]

Derjaguin, V. B. (1934). Untersuchungen über die Reibung und Adhäsion IV. *Kolloid Z.* **69**, 155–164. [6.4.1]

Desplat, J.-C., and Care, C. M. (1996). A Monte Carlo simulation of the micellar phase of an amphiphile and solvent mixture. *Mol. Phys.* **87**, 441–453. [1.4.4, 5.3.2]

Dijkstra, M. (1997). Confined thin films of linear and branched alkanes. *J. Chem. Phys.* **107**,

3277–3288. [1.4.5]

Ducker, W. A., and Grant, L. M. (1996). Effect of substrate hydrophobicity on surfactant surface-aggregate geometry. *J. Phys. Chem.* **100**, 11507–11511. [1.2.2]

Ducker, W. A., Senden, T. J., and Pashley, R. M. (1991). Direct measurement of colloidal forces using an atomic force microscope. *Nature* **353**, 239–241. [1.2.2]

Ducker, W. A., Senden, T. J., and Pashley, R. M. (1992). Measurement of forces in liquids using a force microscope. *Langmuir* **8**, 1831–1836. [1.2.2]

Esselink, K., Hilbers, P. A. J., van Os, N. M., Smit, B., and Karaborni, S. (1994). Molecular dynamics simulations of model oil/water/surfactant systems. *Colloids Surf. A* **91**, 155–167. [1.4.4]

Evans, D. J., and Morriss, G. P. (1990). *Statistical Mechanics of Nonequilibrium Liquids.* Academic Press, London. [1.4.1]

Feller, S. E., Pastor, R. W., Rojnuckarin, A., Bogusz, S., and Brooks, B. R. (1995). Effect of electrostatic force truncation on interfacial and transport properties of water. *J. Phys. Chem.* **100**, 17011–17020. [2.3.3]

Flyvbjerg, H., and Petersen, H. G. (1989). Error estimates on averages of correlated data. *J. Chem. Phys.* **91**, 461–466. [6.3.2]

Frenkel, D., and Smit. B. (1996). *Understanding Molecular Simulation: From Algorithms to Applications.* Academic Press, San Diego. [1.4.1, 2.2.3]

Fukuda, K. (1996). AFM studies of adsorption phenomena of cationic surfactants onto mica surfaces (in Japanese). Master's Thesis, Kyoto University, Japan. [1.2.2, 5.4.1]

Fumi, F. G., and Tosi, M. P. (1964). Ionic sizes and Born repulsive parameters in the NaCl-type alkali halides—I. The Huggins–Mayer and Pauling forms. *J. Phys. Chem. Solids* **25**, 31–43. [3.2.1]

Gao, J., Luedtke, W. D., and Landman, U. (1997). Origin of solvation forces in confined films. *J. Phys. Chem. B* **101**, 4013–4023. [1.4.5]

Gee, M. L., and Israelachvili, J. N. (1990). Interactions of surfactant monolayers across hydrocarbon liquids. *J. Chem. Soc., Faraday Trans.* **86**, 4049–4058. [1.2.1]

Glosli, J. N., and Philpott, M. R. (1992). Molecular dynamics simulation of adsorption of ions from aqueous media onto charged electrodes. *J. Chem. Phys.* **96**, 6962–6969. [1.4.3]

Glosli, J. N., and Philpott, M. R. (1993a). Adsorption of hydrated halide ions on charged electrodes. Molecular dynamics simulation. *J. Chem. Phys.* **98**, 9995–10008. [1.4.3]

Glosli, J. N., and Philpott, M. R. (1993b). Molecular dynamics modeling of electric double layers. *Electrochem. Soc. Symposium Proc.* **93–5**, 90–105. [1.4.3]

Götzelamann, B., and Dietrich, S. (1997). Density profiles and pair correlation functions of hard spheres in narrow slits. *Phys. Rev. E* **55**, 2993–3005. [1.3.2]

Grest, G. S., Dünweg, B., and Kremer, K. (1989). Vectorized link cell Fortran code for molecular dynamics simulaitons for a large number of particles. *Comput. Phys. Commun.* **55**, 269–285. [5.2.5]

Griffiths, J. A., and Heyes, D. M. (1996). Atomistic simulation of overbased detergent inverse micelles. *Langmuir* **12**, 2418–2424. [1.4.4]

Gruhn, T., and Schoen, M. (1997). Microscopic structure of molecularly thin confined liquid-crystal films. *Phys. Rev. E* **55**, 2861–2875. [1.4.5]

Gruhn, T., and Schoen, M. (1998a). A grand canonical ensemble Monte Carlo study of confined planar and homeotropically anchored Gay–Berne films. *Mol. Phys.* **93**, 681–692. [1.4.5]

Gruhn, T., and Schoen, M. (1998b). Substrate-induced order in confined nematic liquid-crystal films. *J. Chem. Phys.* **108**, 9124–9136. [1.4.5]

Haliloglu, T., and Mattice, W. L. (1994). Monte Carlo lattice simulation of the interchange of chains between micelles of diblock copolymers. *Chem. Eng. Sci.* **49**, 2851–2857. [1.4.4, 5.3.2]

Hamaker, H. C. (1937). The London–van der Waals attraction between spherical particles. *Physica* **4**, 1058–1072. [6.3.1, Appendix B]

Han, K. K., Cushman, J. H., and Diestler, D. J. (1993). Grand canonical Monte Carlo simulations of a Stockmayer fluid in a slit micropore. *Mol. Phys.* **79**, 537–545. [1.4.5]

Hansen, J. P., and McDonald, I. R. (1986). *Theory of Simple Liquids* (2nd edn). Academic Press, London. [1.3.1]

Hansma, P. K., Elings, V. B., Marti, O., and Bracker, C. E. (1988). Scanning tunneling microscopy and atomic force microscopy: Application to biology and technology. *Science* **242**, 209–216. [1.2.2]

Hautman, J., and Klein, M. L. (1992). An Ewald summation method for planar surfaces and interfaces. *Mol. Phys.* **75**, 379–395. [2.3.3]

Heinzinger, K. (1996). Molecular dynamics studies of electrolyte solution/metal interfaces. *Mol. Simul.* **16**, 19–30. [1.4.3, 4.2.2]

Heller, H., Schaefer, M., and Schulten, K. (1993). Molecular dynamics simulation of a bilayer of 200 lipids in the gel and in the liquid-crystal phases. *J. Phys. Chem.* **97**, 8343–8360. [1.4.4]

Henderson, D. (1988). An explicit expression for the solvent contribution to the force between colloidal particles using a hard sphere model. *J. Colloid Interface Sci.* **121**, 486–490. [1.3.2, 6.4.2]

Herder, C. E., Ninham, B. W., and Christenson, H. K. (1989). Interaction of hydrocarbon monolayer surfaces across *n*-alkane: A steric repulsion. *J. Chem. Phys.* **90**, 5801–5805. [1.2.1]

Heyes, D. M. (1994). Pressure tensor of partial-charge and point-dipole lattices with bulk and surface geometries. *Phys. Rev. B* **49**, 755–764. [2.3.3]

Heyes, D. M. (1998). *The Liquid State: Applications of Molecular Simulations*. John Wiley & Sons, Chichester. [2.2.1]

Heyes, D. M., and van Swol, F. (1981). The electrostatic potential and field in the surface region of lamina and semi-infinite point charge lattices. *J. Chem. Phys.* **75**, 5051–5058. [2.3.3]

Hoeve, C. A. J., and Benson, G. C. (1957). On the statistical mechanical theory of micelle formation in detergent solutions. *J. Phys. Chem.* **61**, 1149–1158. [5.3.2]

Horn, R. G., and Israelachvili, J. N. (1981). Direct measurement of structural forces between two surfaces in a nonpolar liquid. *J. Chem. Phys.* **75**, 1400–1411. [1.2.1, 6.4.2]

Horn, R. G., and Israelachvili, J. N. (1988). Molecular organization and viscosity of a thin film of molten polymer between two surfaces as probed by force measurements. *Macromolecules* **21**, 2836–2841. [1.2.1]

Horn, R. G., Hirz, S. J., Hadziioannou, G., Frank, C. W., and Catala, J. M. (1989). A reevaluation of forces measured across thin polymer films: Nonequilibrium and pinning Effects. *J. Chem. Phys.* **90**, 6767–6774. [1.2.1]

Iiyama, T., Nishikawa, K., Otowa, T., and Kaneko, K. (1995). An ordered water molecular assembly structure in a slit-shaped carbon nanospace. *J. Phys. Chem.* **99**, 10075–10076. [1.4.2, 2.4.3]

Israelachvili, J. N. (1987). Solvation forces and liquid structure, as probed by direct force measurements. *Acc. Chem. Res.* **20**, 415–421. [1.2.1, 6.4.2]

Israelachvili, J. N. (1991). *Intermolecular and Surface Forces* (2nd edn). Academic Press, New York. [1.2.1, 6.4.2, 7.4.3, Appendix A]

Israelachvili, J. N., and Adams, G. E. (1978). Measurement of forces between two mica surfaces in aqueous electrolyte solutions in the range 0–100 nm. *J. Chem. Soc., Faraday Trans. I* **74**, 975–1001. [1.2.1]

Israelachvili, J. N., and Kott, S. J. (1988). Liquid structuring at solid interfaces as probed by direct force measurements: The transition from simple to complex liquids and polymer fluids. *J. Chem. Phys.* **88**, 7162–7166. [1.2.1]

Israelachvili, J. N., and Wennerström, H. (1996). Role of hydration and water structure in biological and colloidal interactions. *Nature* **379**, 219–225. [1.2.1]

Jaschke, M., Butt, H.-J., Gaub, H. E., and Manne, S. (1997). Surfactant aggregates at a metal surface. *Langmuir* **13**, 1381–1384. [1.2.2]

Jorgensen, W. L., and Tirado-Rives, J. (1988). The OPLS potential functions for proteins. Energy minimizations for crystals of cyclic peptides and crambin. *J. Am. Chem. Soc.* **110**, 1657–1666. [1.4.1]

Jorgensen, W. L., Chandrasekhar, J., Madura, J. D., Impey, R. W., and Klein, M. L. (1983). Comparison of simple potential functions for simulating liquid water. *J. Chem. Phys.* **79**, 926–935. [2.3.1]

Kanda, Y., Nakamura, T., and Higashitani, K. (1998). AFM studies of interaction forces between surfaces in alcohol–water solutions. *Colloids Surf. A* **139**, 55–62. [7.1, 7.4.2, 7.4.3, 7.4.4, 7.5]

Karaborni, S., and Smit, B. (1996). Computer simulations of surfactant structures. *Curr. Opin. Colloid Interface Sci.* **1**, 411–415. [1.4.4]

Karaborni, S., van Os, N. M., Esselink, K., and Hilbers, P. A. J. (1993). Molecular dynamics simulations of oil solubilization in surfactant solutions. *Langmuir* **9**, 1175–1178. [1.4.4, 5.3.2]

Karaborni, S., Esselink, K., Hilbers, P. A. J., Smit, B., Karthäuser, J., van Os, N. M., and Zana, R. (1994). Simulating the self-assembly of gemini (dimeric) surfactants. *Science* **266**, 254–256. [1.4.4, 5.3.2]

Kinoshita, M. (1998). Long-range attractive interaction between macroparticles in a binary fluid mixture. *Mol. Phys.* **94**, 485–494. [1.3.2]

Kinoshita, M., and Hirata, F. (1996). Application of the reference interaction site model theory to analysis on surface-induced structure of water. *J. Chem. Phys.* **104**, 8807–8815. [1.3.2, 2.4.3]

Kinoshita, M., Iba, S., and Harada, M. (1996a). Interaction between macroparticles in aqueous electrolytes. *J. Chem. Phys.* **105**, 2487–2499. [1.3.2, 6.4.2]

Kinoshita, M., Iba, S., Kuwamoto, K., and Harada, M. (1996b). Interaction between macroparticles in Lennard-Jones fluids or in hard-sphere mixtures. *J. Chem. Phys.* **105**, 7177–7183. [1.3.2, 6.2.1, 6.4.2, 6.4.3]

Kinoshita, M., Iba, S., Kuwamoto, K., and Harada, M. (1996c). Interaction between macroparticles in a simple model system of a nonpolar liquid containing trace amounts of water. *J. Chem. Phys.* **105**, 7184–7191. [1.3.2]

Kjellander, R., and Marcelja, S. (1985a). Polarization of water between molecular surfaces: A molecular dynamics study. *Chem. Scripta* **25**, 73–80. [1.4.2, 2.4.1]

Kjellander, R., and Marcelja, S. (1985b). Pertubation of hydrogen bonding in water near polar surfaces. *Chem. Phys. Lett.* **120**, 393–396. [1.4.2, 3.3.4]

Kjellander, R., and Sarman, S. (1990). A study of anisotropic pair correlation theories for Lennard-Jones fluids in narrow slits. Part I. Density profiles and surface interactions. *Mol. Phys.* **70**, 215–237. [1.3.2, 6.2.1, 6.4.3]

Kjellander, R., and Sarman, S. (1991). A study of anisotropic pair correlation theories for Lennard-Jones fluids in narrow slits. Part II. Pair correlations and solvation forces. *Mol. Phys.* **74**, 665–688. [1.3.2, 6.2.1, 6.4.3]

Klein, M. L. (1992). Conformations of flexible molecules in fluid phases. *J. Chem. Soc., Faraday Trans.* **88**, 1701–1705. [1.4.4]

Kurihara, K., and Kunitake, T. (1992). Submicron-range attraction between hydrophobic surfaces of monolayer-modified mica in water. *J. Am. Chem. Soc.* **114**, 10927–10933. [1.2.1]

Laaksonen, L., and Rosenholm, J. B. (1993). Molecular dynamics simulations of the water/octanoate interface in the presence of micelles. *Chem. Phys. Lett.* **216**, 429–434. [1.4.4]

Lang, J., and Zana, R. (1987). Chemical relaxation methods. In *Surfactant Solutions: New Methods of Investigation* (ed. Zana, R.). Surfactant Science Series Vol. 22, p 405–452. Marcel Dekker, New York. [5.3.2]

Larson, R. G. (1992). Monte Carlo simulation of microstructural transitions in surfactant systems. *J. Chem. Phys.* **96**, 7904–7918. [1.4.4, 5.3.2]

Larson, R. G. (1994). Molecular simulation of ordered amphiphilic phases. *Chem. Eng. Sci.* **49**, 2833–2850. [1.4.4]

Larson, R. G. (1996). Monte Carlo simulations of the phase behavior of surfactant solutions. *J. Phys. II France* **6**, 1441–1463. [1.4.4]

Larson, R. G. (1997). Simulations of self-assembly. *Curr. Opin. Colloid Interface Sci.* **2**, 361–364. [1.4.4]

Lee, C. Y., McCammon, J. A., and Rossky, P. J. (1984). The structure of liquid water at an extended hydrophobic surface. *J. Chem. Phys.* **80**, 4448–4455. [1.4.2, 2.3.1, 2.4.1, 2.4.3]

Lee, S. H., and Rossky, P. J. (1994). A comparison of the structure and dynamics of liquid water at hydrophobic and hydrophilic surfaces—A molecular dynamics simulation study. *J. Chem. Phys.* **100**, 3334–3345. [1.4.2, 2.4.1, 2.4.3, 2.4.4, 3.3.4]

Lekner, J. (1989). Summation of dipolar fields in simulated liquid–vapor interfaces. *Physica A* **157**, 826–838. [2.3.3]

Lekner, J. (1991). Summation of Coulomb fields in computer-simulated disordered systems. *Physica A* **176**, 485–498. [2.3.3]

Linse, P. (1987). Monte Carlo simulation of liquid–liquid benzene–water interface. *J. Chem. Phys.*

86, 4177–4187. [2.4.2]

Luzar, A., Bratko, D., and Blum, L. (1987). Monte Carlo simulation of hydrophobic interaction. *J. Chem. Phys.* **86**, 2955–2959. [1.4.5]

MacKerell, A. D. (1995). Molecular dynamics simulation analysis of a sodium dodecyl sulfate micelle in aqueous solution: Decreased fluidity of the micelle hydrocarbon interior. *J. Phys. Chem.* **99**, 1846–1855. [1.4.4]

Magda, J. J., Tirrell, M., and Davis, H. T. (1985). Molecular dynamics of narrow, liquid-filled pores. *J. Chem. Phys.* **83**, 1888–1901. [1.4.5, 6.2.1, 6.4.3]

Manne, S. (1997). Visualizing self-assembly: Force microscopy of ionic surfactant aggregates at solid–liquid interfaces. *Prog. Colloid Polym. Sci.* **103**, 226–233. [1.2.2]

Manne, S., and Gaub, H. E. (1995). Molecular organization of surfactants at solid–liquid interfaces. *Science* **270**, 1480–1482. [1.2.2]

Manne, S., Cleveland, J. P., Gaub, H. E., Stucky, G. D., and Hansma, P. K. (1994). Direct visualization of surfactant hemimicelles by force microscopy of the electrical double layer. *Langmuir* **10**, 4409–4413. [1.2.2]

Mar, W., and Klein, M. L. (1994). Molecular dynamics study of the self-assembled monolayer composed of $S(CH_2)_{14}CH_3$ molecules using an all-atoms model. *Langmuir* **10**, 188–196. [1.4.4]

Marrink, S.-J., and Berendsen, H. J. C. (1994). Simulation of water transport through a lipid membrane. *J. Phys. Chem.* **98**, 4155–4168. [1.4.4]

Matsui, T., and Jorgensen, W. L. (1992). Free energy profiles for Na^+ adsorption on a metal electrode. *J. Am. Chem. Soc.* **114**, 3220–3226. [1.4.3, 4.3.2]

Matsuoka, O., Clementi, E., and Yoshimine, M. (1976). CI study of the water dimer potential surface. *J. Chem. Phys.* **64**, 1351–1361. [2.3.1]

Mayo, S. L., Olafson, B. D., and Goddard III, W. A. (1990). DREIDING: A generic force field for molecular simulations. *J. Phys. Chem.* **94**, 8897–8909. [1.4.1]

McCarthy, M. I., Schenter, G. K., Scamehorn, C. A., and Nicholas, J. B. (1996). Structure and dynamics of the water/MgO interface. *J. Phys. Chem.* **100**, 16989–16995. [1.4.2, 2.4.1]

McKechnie, J. I., Brown, D., and Clarke, J. H. R. (1992). Methods of generating dense relaxed amorphous polymer samples for use in dynamic simulations. *Macromolecules* **25**, 1562–1567. [7.3.2]

Müller-Plathe, F., and Brown, D. (1991). Multi-colour algorithms in molecular simulation: Vectorisation and parallelisation of internal forces and constraints. *Comput. Phys. Commun.* **64**, 7–14. [5.2.5]

Ohtaki, H., and Fukushima, N. (1989). Dissolution of an NaCl crystal with the (111) and (–1–1–1) faces. *Pure Appl. Chem.* **61**, 179–185. [3.1, 3.3.1]

Ohtaki, H., Fukushima, N., Hayakawa, E., and Okada, I. (1988). Dissolution process of sodium chloride crystal in water. *Pure Appl. Chem.* **60**, 1321–1324. [3.1, 3.3.1]

Pashley, R. M. (1981). DLVO and hydration forces between mica surfaces in Li^+, Na^+, K^+, and Cs^+ electrolyte solutions: A correlation of double-layer and hydration forces with surface cation exchange properties. *J. Colloid Interface Sci.* **83**, 531–546. [1.2.1]

Pashley, R. M., and Israelachvili, J. N. (1984a). DLVO and hydration forces between mica surfaces in Mg^{2+}, Ca^{2+}, Sr^{2+}, and Ba^{2+} chloride solutions. *J. Colloid Interface Sci.* **97**, 446–455. [1.2.1]

Pashley, R. M., and Israelachvili, J. N. (1984b). Molecular layering of water in thin films between mica surfaces and its relation to hydration forces. *J. Colloid Interface Sci.* **101**, 511–523. [1.2.1]

Pastor, R. W. (1994). Molecular dynamics and Monte Carlo simulations of lipid bilayers. *Curr. Opin. Struct. Biol.* **4**, 486–492. [1.4.4]

Patrick, H. N., Warr, G. G., Manne, S., and Aksay, I. A. (1997). Self-assembly structures of nonionic surfactants at graphite/solution interfaces. *Langmuir* **13**, 4349–4356. [1.2.2]

Perera, L., and Berkowitz, M. L. (1993). Free energy profiles for Li^+ and I^- ions approaching the Pt(100) surfaces: A molecular dynamics study. *J. Phys. Chem.* **97**, 13803–13806. [1.4.3, 4.2.1]

Pettitt, B. M., and Rossky, P. J. (1986). Alkali halides in water: Ion–solvent correlations and ion–ion potentials of mean force at infinite dilution. *J. Chem. Phys.* **84**, 5836–5844. [3.2.1, 3.2.2]

Prevost, M., van Belle, D., Lippens, G., and Wodak, S. (1990). Computer simulations of liquid water: Treatment of long-range interactions. *Mol. Phys.* **71**, 587–603. [2.3.3]

Raghavan, K., Foster, K., and Berkowitz, M. (1991a). Comparison of the structure and dynamics of water at the Pt(111) and Pt(100) interfaces: Molecular dynamics study. *Chem. Phys. Lett.* **177**, 426–432. [1.4.2, 2.4.1]

Raghavan, K., Foster, K., Motakabbir, K., and Berkowitz, M. (1991b). Structure and dynamics of water at the Pt(111) interface: Molecular dynamics study. *J. Chem. Phys.* **94**, 2110–2117. [1.4.2, 2.4.1]

Rapaport, D. C. (1988). Large-scale moelcular dynamics simulations using vector and parallel computers. *Comput. Phys. Rep.* **9**, 1–53. [5.2.5]

Rapaport, D. C. (1995). *The Art of Molecular Dynamics Simulation*. Cambridge University Press, Cambridge. [1.4.1, 2.2.1, 2.2.3]

Rector, D. R., van Swol, F., and Henderson, J. R. (1994). Simulation of surfactant solutions I. Micelle formation in the bulk phase. *Mol. Phys.* **82**, 1009–1031. [1.4.4, 5.3.2]

Rhee, Y., Halley, J. W., Hautman, J., and Rahman, A. (1989). Ewald method in molecular dynamics for systems of finite extent in one of three dimensions. *Phys. Rev. B* **40**, 36–42. [2.3.3]

Rose, D. A., and Benjamin, I. (1991). Solvation of Na^+ and Cl^- at the water–platinum (100) interface. *J. Chem. Phys.* **95**, 6856–6865. [1.4.3, 4.2.1, 4.3.2]

Rose, D. A., and Benjamin, I. (1993). Adsorption of Na^+ and Cl^- at the charged water–platinum interface. *J. Chem. Phys.* **98**, 2283–2290. [1.4.3]

Ryckaert, J.-P., Ciccotti, G., and Berendsen, H. J. C. (1977). Numerical integration of the Cartesian equations of motion of a system with constraints: Molecular dynamics of *n*-alkanes. *J. Comput. Phys.* **23**, 327–341. [6.3.2]

Sakakibara, T. (1997). Molecular dynamics simulation studies of water and ions near NaCl crystal surfaces (in Japanese). Master's Thesis, Kyoto University, Japan. [4.3.2]

Sarman, S. (1990). The influence of the fluid–wall interaction potential on the structure of a simple fluid in a narrow slit. *J. Chem. Phys.* **92**, 4447–4455. [1.3.2, 6.2.1, 6.4.3]

Schoen, M., and Diestler, D. J. (1997). Ultrathin fluid films confined to a chemically heterogeneous slit-shaped nanopore. *Phys. Rev. E* **56**, 4427–4440. [1.4.5]

Schweighofer, K. J., Essmann, U., and Berkowitz, M. (1997). Simulation of sodium dodecyl sulfate at the water–vapor and water–carbon tetrachloride interfaces at low surface coverage. *J. Phys. Chem. B* **101**, 3793–3799. [1.4.4]

Shelley, J. C., Sprik, M., and Klein, M. L. (1993). Molecular dynamics simulation of an aqueous sodium octanoate micelle using polarizable surfactant molecules. *Langmuir* **9**, 916–926. [1.4.4]

Shinoda, W., Namiki, N., and Okazaki, S. (1997). Molecular dynamics study of a lipid bilayer: Convergence, structure, and long-time dynamics. *J. Chem. Phys.* **106**, 5731–5743. [1.4.4]

Siepmann, J. I., and McDonald, I. R. (1993). Monte Calro study of the properties of self-assembled monolayers formed by adsorption of $CH_3(CH_2)_{15}SH$ on the (111) surface of gold. *Mol. Phys.* **79**, 457–473. [1.4.4]

Siepmann, J. I., and Sprik, M. (1995). Influence of surface topology and electrostatic potential on water/electrode systems. *J. Chem. Phys.* **102**, 511–524. [1.4.2]

Siepmann, J. I., Karaborni, S., and Klein, M. L. (1994). Monte Carlo simulation of the liquid–vapor coexistance in a Langmuir monolayer of pentadecanoic acid. *J. Phys. Chem.* **98**, 6675–6678. [1.4.4]

Smit, B. (1988). Molecular-dynamics simulations of amphiphilic molecules at a liquid–liquid

interface. *Phys. Rev. A* **37**, 3431–3433. [1.4.1, 1.4.4, 5.2.1]

Smit, B. (1993). Computer simulations of surfactants. In *Computer Simulation in Chemical Physics* (eds. Allen, M. P., and Tildesley, D. J.). NATO ASI Series C Vol. 397, p 461–472 Kluwer, Dordrecht. [1.4.4]

Smit, B., Hilbers, P. A. J., and Esselink, K. (1993a). Computer simulations of simple oil/water/surfactants systems. *Tenside Surf. Det.* **4**, 287–293. [1.4.4]

Smit, B., Schlijper, A. G., Rupert, L. A. M., and van Os, N. M. (1990). Effects of chain length of surfactants on the interfacial tension: Molecular dynamics simulations and experiments. *J. Phys. Chem.* **94**, 6933–6935. [1.4.1, 1.4.4, 5.2.1]

Smit, B., Esselink, K., Hilbers, P. A. J., van Os, N. M., Rupert, L. A. M., and Szleifer, I. (1993b). Computer simulations of surfactant self-assembly. *Langmuir* **9**, 9–11. [1.4.4, 5.3.2]

Smit, B., Hilbers, P. A. J., Esselink, K., Rupert, L. A. M., van Os, N. M., and Schlijper, A. G. (1991). Structure of a water/oil interface in the presence of micelles: A computer simulation study. *J. Phys. Chem.* **95**, 6361–6368. [1.4.4]

Smith, W., and Fincham, D. (1982). *The Program MDMPOL: CCP5 Program Library Documentation.* Daresbury Laboratory, Warrington, England. [2.3.4]

Snook, I. K., and van Megen, W. (1980). Solvation forces in simple dense fluids. I. *J. Chem. Phys.* **72**, 2907–2913. [1.4.5, 6.2.1, 6.4.3]

Somers, S. A., McCormick, A. V., and Davis, H. T. (1993). Superselectivity and solvation forces of a two component fluid adsorbed in slit micropores. *J. Chem. Phys.* **99**, 9890–9898. [1.4.5]

Sonnenschein, R., and Heinzinger, K. (1983). A molecular dynamics study of water between Lennard-Jones walls. *Chem. Phys. Lett.* **102**, 550–554. [2.4.4]

Spohr, E. (1989). Computer simulation of the water/platinum interface. *J. Phys. Chem.* **93**, 6171–6180. [1.4.2, 2.4.1, 3.3.4]

Spohr, E. (1990). Computer simulation of the water/platinum interface. Dynamical results. *Chem. Phys.* **141**, 87–94. [1.4.2, 2.4.1]

Spohr, E. (1993). A computer simulation study of iodide ion solvation in the vicinity of a liquid water/metal interface. *Chem. Phys. Lett.* **207**, 214–219. [1.4.3, 4.2.1, 4.2.2]

Spohr, E., and Heinzinger, K. (1986). A molecular dynamics study of an aqueous LiI solution between Lennard-Jones walls. *J. Chem. Phys.* **84**, 2304–2309. [1.4.3]

Sprik, M. (1993). Effective pair potentials and beyond. In *Computer Simulation in Chemical Physics* (eds. Allen, M. P., and Tildesley, D. J.). NATO ASI Series C Vol. 397, p 211–259. Kluwer, Dordrecht. [2.2.1]

Steele, W. A. (1973). The physical interaction of gases with crystalline solids. I. Gas–solid energies

and properties of isolated adsorbed atoms. *Surf. Sci.* **36**, 317–352. [5.2.2, 6.2.2]

Steele, W. A. (1974). *The interaction of gases with solid surfaces.* Pergamon Press, Oxford. [5.2.2]

Steinbach, P. J., and Brooks, B. R. (1994). New spherical-cutoff methods for long-range forces in macromolecular simulation. *J. Comput. Chem.* **15**, 667–683. [2.3.3]

Stillinger, F. H., and Rahman, A. (1974). Improved simulation of liquid water by molecular dynamics. *J. Chem. Phys.* **60**, 1545–1557. [2.3.1]

Stoddard, S. D. (1978). Identifying clusters in computer experiments on systems of particles. *J. Comput. Phys.* **27**, 291–293. [5.2.4]

Tarek, M., Tobias, D. J., and Klein, M. L. (1995). Molecular dynamics simulation of tetradecyltrimethylammonium bromide monolayers at the air/water interface. *J. Phys. Chem.* **99**, 1393–1402. [1.4.4]

Taylor, D. P., Hess, W. P., and McCarthy, M. I. (1997). Structure and energetics of the water/NaCl(100) interface. *J. Phys. Chem. B* **101**, 7455–7463. [3.2.2]

Telo da Gama, M. M., and Gubbins, K. E. (1986). Adsorption and orientation of amphiphilic molecules at a liquid–liquid interface. *Mol. Phys.* **59**, 227–239. [1.4.1, 5.2.1]

The Chemical Society of Japan (1993). Kagaku Binran Kiso-hen II (4th edn) (Handbook of Chemistry). p 699. Maruzen, Tokyo. [3.2.3]

Tobias, D. J., Tu, K., and Klein, M. L. (1997). Atomic-scale molecular dynamics simulations of lipid membranes. *Curr. Opin. Colloid Interface Sci.* **2**, 15–26. [1.4.4]

Toney, M. F., Howard, J. N., Richer, J., Borges, G. L., Gordon, J. G., Melroy, O. R., Wiesler, D. G., Yee, D., and Sorensen, L. B. (1994). Voltage-dependent ordering of water molecules at an electrode–electrolyte interface. *Nature* **368**, 444–446. [1.4.2]

Tosi, M. P., and Fumi, F. G. (1964). Ionic sizes and Born repulsive parameters in the NaCl-type alkali halides—II. The generalized Huggins–Mayer form. *J. Phys. Chem. Solids* **25**, 45–52. [3.2.1]

Tsao, Y.-H., Yang, S. X., Evans, D. F., and Wennerström, H. (1991). Interactions between hydrophobic surfaces. Dependence on temperature and alkyl chain length. *Langmuir* **7**, 3154–3159. [1.2.1]

Urbina-Villalba, G., Landrove, R. M., and Guaregua, J. A. (1997). Molecular dynamics simulation of the interfacial behavior of a heptane/water system in the presence of nonylphenol triethoxylated surfactants. 1. Surface energy, surface entropy, and interaction energies as a function of temperature and surfactant concentration. *Langmuir* **13**, 1644–1652. [1.4.4]

Wang, Y., Mattice, W. L., and Napper, D. H. (1993). Simulation of the formation of micelles by

diblock copolymers under weak segregation. *Langmuir* **9**, 66–70. [1.4.4]

Wang, Y., Hill, K., and Harris, J. G. (1994). Confined thin films of a linear and branched octane. A comparison of the structure and solvation forces using molecular dynamics simulations. *J. Chem. Phys.* **100**, 3276–3285. [1.4.5]

Wanless, E. J., and Ducker, W. A. (1996). Organization of sodium dodecyl sulfate at the graphite–solution interface. *J. Phys. Chem.* **100**, 3207–3214. [1.2.2]

Watanabe, K., and Klein, M. L. (1991). Molecular dynamics studies of sodium octanoate and water: The liquid-crystal mesophase with two-dimensional hexagonal symmetry. *J. Phys. Chem.* **95**, 4158–4166. [1.4.4]

Watanabe, K., Ferrario, M., and Klein, M. L. (1988). Molecular dynamics study of a sodium octanoate micelle in aqueous solution. *J. Phys. Chem.* **92**, 819–821. [1.4.4]

Weiner, S. J., Kollman, P. A., Nguyen, D. T., and Case, D. A. (1986). An all atom force field for simulations of proteins and nucleic acids. *J. Comput. Chem.* **7**, 230–252. [1.4.1]

Wendoloski, J. J., Kimatian, S. J., Schutt, C. E., and Salemme, F. R. (1989). Molecular dynamics simulation of a phospholipid micelle. *Science* **243**, 636–638. [1.4.4]

Wennerström, H., and Lindman, B. (1979). Micelles. Physical chemistry of surfactant association. *Phys. Rep.* **52**, 1–86. [5.3.2]

Wijmans, C. M., and Linse, P. (1997). Monte Carlo simulations of the adsorption of amphiphilic oligomers at hydrophobic interfaces. *J. Chem. Phys.* **106**, 328–338. [5.4.1]

Wu, D., Chandler, D., and Smit, B. (1992). Electrostatic analogy for surfactant assemblies. *J. Phys. Chem.* **96**, 4077–4083. [Appendix A]

Zhu, S.-B., and Robinson, G. W. (1991). Structure and dynamics of liquid water between plates. *J. Chem. Phys.* **94**, 1403–1410. [1.4.2]

Acknowledgments

This thesis is a summary of my work conducted at the Laboratory of Surface Control Engineering, Department of Chemical Engineering, Kyoto University from 1993 to 1999.

I am greatly indebted to Dr. Ko Higashitani, Professor of the Department of Chemical Engineering, Kyoto University, for his constant supervision, kind consideration, and warm encouragement throughout this work. Without his supervision and support, this work would certainly not have been made. One of the greatest gifts from Prof. Higashitani is the deepest impression of his eyes, boyishly brilliant as a researcher and full of tenderness as an educator. Again, I would like to express my sincere appreciation and deep gratitude to Prof. Higashitani.

It was a great pleasure and honor to have two supervisors for this thesis, Dr. Fumihiko Tanaka, Department of Polymer Chemistry, and Dr. Hiroaki Masuda, Department of Chemical Engineering, Professors of Kyoto University. I would like to express my sincere appreciation for the efforts of both supervisors. Their careful reading of the original manuscript led to many critical suggestions which were indeed valuable.

I would like to express my sincere gratitude to Dr. Minoru Miyahara, Associate Professor of Kyoto University, for his continuing interest, kind guidance, and helpful discussions. I also would like to express my gratitude to Mr. Yoichi Kanda, Research Instructor of Kyoto University, for his valuable discussions, especially fruitful suggestions on the study of Chapter 7.

This thesis could not be submitted without the technical assistance of Messrs. Takashi Sakakibara and Satoshi Tsuji. I wish to express my thanks to them for

their efforts and ideas on conducing this work. This computational work is greatly indebted to the Supercomputer Laboratory, Institute for Chemical Research, Kyoto University, for the use of supercomputers.

I was very fortunate to meet and discuss with Dr. Masahiro Kinoshita, Associate Professor of the Institute of Advanced Energy, Kyoto University. His outstanding and challenging work by the Integral Equation Theory not only led me to new ideas, but also stimulated me to the development of a new computational method given in Chapter 6.

I'm very happy to have a good friend of mine at the laboratory of Prof. Higashitani. His name is Jun Oshitani, presently Research Instructor of Okayama University. I have learned from him many things; especially, the affection for researches and colleagues. I would like to express my sincere appreciation to him.

At the same time, I can not forget all other members of Prof. Higashitani's laboratory who discuss actively with each other to improve further their academic researches. Especially, Mr. Naoyuki Ishida impresses me with his sincere attitude as a researcher. I am thankful to Miss Takako Inuta, Secretary of the laboratory, for her encouragement as well as secretarial work. Now, I am proud to have been a member of Prof. Higashitani's laboratory and hope that this wonderful laboratory continues to lead the world in research activities.

Finally, I would like to express my deepest appreciation to my parents for their affectionate support.

Kyoto Hiroyuki Shinto

February 1999

List of Publications

Chapter 3

Shinto, H., Sakakibara, T., and Higashitani, K. (1998). Molecular Dynamics Simulations of Water at NaCl(001) and NaCl(011) Surfaces. *J. Phys. Chem. B* **102**, 1974–1981.

Chapter 4

Shinto, H., Sakakibara, T., and Higashitani, K. (1998). Free Energy Profiles for Na^+ and Cl^- Adsorption onto Water/NaCl Crystal Interfaces Evaluated by Molecular Dynamics Simulation. *J. Chem. Eng. Japan* **31**, 771–779.

Chapter 5

Shinto, H., Tsuji, S., Miyahara, M., and Higashitani, K. (1999). Molecular Dynamics Simulations of Surfactant Aggregation on Hydrophilic Walls in Micellar Solutions. *Langmuir* **15**, 578–586.

Chapter 6

Shinto, H., Miyahara, M., and Higashitani, K. (1999). Evaluation of Interaction Forces between Macroparticles in Simple Fluids by Molecular Dynamics Simulation. *J. Colloid Interface Sci.* **209**, 79–85.

Chapter 7

Shinto, H., Miyahara, M., and Higashitani, K. (1999). Interaction Forces between Colloidal Particles in Alcohol–Water Mixtures Evaluated by Simple Model Simulations. *Langmuir*, to be submitted.